Strandberg, Bruno (2017) Threshold π– photoproduction and Compton scattering on the deuteron. PhD thesis.

Threshold π^- photoproduction and Compton scattering on the deuteron

Bruno Strandberg

A thesis presented for the degree of
Doctor of Philosophy

Nuclear Physics Group
School of Physics and Astronomy
University of Glasgow

August 2017

Threshold π^- photoproduction and Compton scattering on the deuteron

Bruno Strandberg

Submitted for the degree of Doctor of Philosophy
August 2017

Abstract

Over the years various theoretical frameworks have been developed to gain insight into the strong force at the hadronic scale and several of them make predictions for the pion photoproduction cross-section at threshold. The cross-sections for positive and neutral pion photoproduction have been measured, but experimental data on the negative pion has so far been absent. The first measurement of the cross-section $\sigma(E_\gamma)$ for π^- photoproduction on the deuteron near threshold is presented. The π^- cross-section provides a test for the theoretical models that aim to describe Quantum Chromodynamics in the non-perturbative regime.

Nucleon polarisabilities are long range nucleon structure observables and give insight into the internal degrees of freedom of the nucleon. The proton polarisabilities are determined significantly more accurately compared to the neutron polarisabilities. The latter can be extracted from the differential cross-section for Compton scattering on the deuteron. The first measurement of the differential cross-section $d\sigma/d\Omega(E_\gamma, \cos\theta)$ for Compton scattering on the deuteron as a function of photon energy (E_γ) and polar angle (θ) above the pion threshold is presented. The new experimental data contributes to the ongoing effort for accurate determination of the neutron polarisabilities.

Due to recent theoretical advances the differential cross-section for Compton scattering on Helium-3 can now also be interpreted in a way that allows extraction of the neutron polarisabilities. In the appendix a proposed experiment to measure the differential cross-section for Compton scattering on Helium-3 with a Helium Gas Scintillator Active target is considered.

Declaration

The work in this thesis is based on research carried out at the Nuclear Physics Group, School of Physics & Astronomy, University of Glasgow, UK. No part of this thesis has been submitted elsewhere for any other degree or qualification and it is all my own work unless referenced to the contrary in the text.

Contents

Introduction

In this thesis the analysis of the last photonuclear experiment performed at the MAX IV laboratory[1] in Lund is presented. The experiment measured the photoproduction cross-section for negative pions on the deuteron near threshold and the differential cross-section for Compton scattering on the deuteron.

It is an inherent property of the strong force that the strength of the interactions between quarks and gluons - the “building blocks” of nucleons - is energy dependent. This is encoded in the running coupling constant of Quantum Chromodynamics (QCD) - the quantum field theory of the strong force. Due to this the strongly interacting particles reveal different behaviour at different energy scales. At low energies ($\sim$ 1 GeV) the quarks are closely bound in composite hadronic states, typically forming mesons (2-quark systems) and baryons (3-quark systems). Thus hadrons, rather than quarks and gluons, act as relevant effective degrees of freedom. In this regime a special role is played by the lightest baryonic states - the proton and the neutron - and the lightest mesonic state - the pion. Protons and neutrons form atomic nuclei and the pion acts as the long range mediator of the strong force that binds them together. At high energies the interaction between quarks and gluons becomes weaker and the elementary particles become the dominant degrees of freedom. Although the strong force is described by QCD at all energies, solution of the QCD Lagrangian by perturbative techniques is impossible at low energy. Understanding the strong force at the hadronic scale is a complex problem that requires input both from theoreticians and experimentalists. The experiment of this thesis was performed at an energy of $\sim$ 0.15 GeV and the extracted cross-sections can be considered as a small contribution to the ongoing effort to gain a better insight into the dynamics of tightly bound quark systems.

One way of studying QCD at low energy is through to the excitation spectrum of the nucleon. Various hadronic states can be excited by firing electron or photon beams at a nucleon target. The first excited state of the nucleon (called the Δ resonance) decays to a nucleon and a pion. The threshold production of both positive and neutral pions has been measured before, but experimental data on the threshold production of negative pions has so far been absent. The results of this thesis fill that gap and provide a further test for the various models that aim to describe QCD in the non-perturbative regime.

The Compton scattering measurement is a continuation of an ongoing effort to extract the neutron *polarisabilities*. Polarisabilities are long range nucleon structure observables that describe the “rigidity” of a nucleon with respect to its deformation by an external electromagnetic field and are tightly related to the internal structure of the nucleon. The impinging electromagnetic radiation interacts with the charge

---

[1] The experiment employed the MAX-I accelerator that was dismantled in the second half of 2015.

constituents of the nucleon, which in turn influences the observed differential cross-section. The results presented here constitute a first measurement of the differential cross-section for Compton scattering on the deuteron above the pion threshold.

The thesis is divided into six chapters and two appendices. Chapter 1 provides an overview of the theoretical treatment of the pion photoproduction and the Compton scattering reactions and summarises previous experiments. In Chapter 2 the experimental apparatus and setup at the MAX IV laboratory is discussed and the methods of event identification are reviewed. In Chapter 3 the detector calibration procedures are outlined. Chapter 4 identifies the main sources of background and details methods for their removal from the experimental signal. Chapter 5 describes the method of extraction of the cross-section $\sigma(E_\gamma)$ for π^- photoproduction on the deuteron and presents the results of the pion analysis. Chapter 6 deals with the extraction of the differential cross-section $d\sigma/d\Omega(E_\gamma, \cos\theta)$ for Compton scattering on the deuteron as a function of photon energy (E_γ) and polar angle (θ) and presents the results of the Compton analysis. Appendix A summarises various aspects of computer simulations of the experiment that were integral to the analyses. Finally, Appendix B discusses a recently proposed experiment to measure the differential cross-section for Compton scattering on Helium-3. The experiment of Appendix B is separate from the Lund experiment, but is strongly tied to the neutron polarisabilities programme.

Chapter 1

Overview

The Lund experiment gives access to two different reaction channels. Section 1.1 reviews the theoretical models and previous experiments related to the π^- photoproduction channel, whereas Section 1.2 deals with the Compton scattering channel. No explicit discussion for various theoretical models is presented in the Compton overview. This is because the theoretical treatment relevant for the Compton scattering is already introduced when the π^- photoproduction is discussed.

1.1 π^- photoproduction

This section provides an overview of the threshold pion photoproduction reaction on the nucleon. Section 1.1.1 is devoted to the reaction kinematics and explains how some of the values and expressions often encountered in the theoretical predictions are related to the pion photoproduction cross-section. Sections 1.1.2 – 1.1.5 describe various models that make predictions for the near threshold pion photoproduction reaction. The actual numerical values of the model predictions are summarised separately in Section 1.1.6. Section 1.1.7 discusses briefly the implications of using a bound neutron target for photoproduction experiments and Section 1.1.8 finishes the π^- photoproduction overview with a summary of previous measurements.

1.1.1 Kinematics, multipole expansion and the E_{0+} multipole

The kinematics of the pion photoproduction reaction on the nucleon is illustrated in Figure 1.1. It depicts an initial photon γ with 4-momentum k interacting with a nucleon N with initial 4-momentum p_i, resulting in a final pion π and a nucleon N with 4-momenta q and p_f, respectively. The shaded sphere represents the hadronic vertex. The expression for the unpolarised differential cross-section in the center-of-momentum frame reads [2]

$$\frac{d\sigma}{d\Omega} = \frac{|\mathbf{q}|}{|\mathbf{k}|} \left(\frac{1}{16} \frac{1}{(2\pi)^2} \frac{M^2}{W^2} \sum_{\text{pol}} |\mathcal{M}|^2 \right), \tag{1.1}$$

where $\mathbf{k}$ and $\mathbf{q}$ stand for the photon and pion 3-momenta, M is the nucleon mass, $W = \sqrt{s} = \sqrt{(p_i + k)^2}$ is the centre-of-momentum energy and $\mathcal{M}$ is the invariant amplitude that describes the transition from an initial state photon and nucleon to a

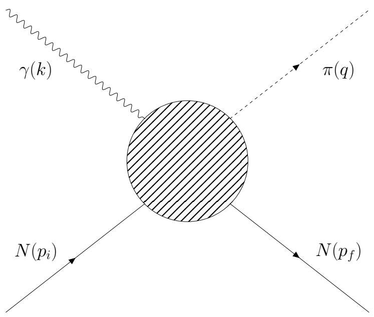

Figure 1.1: Pion photoproduction. Wave line - photon, dashed line - pion, solid lines - initial and final nucleon [1].

final state pion and nucleon. A summation over the polarisations of the final states is indicated. The physics of the process is contained in the invariant amplitude and although Eq. (1.1) is exact, evaluating the invariant amplitude is complicated and usually some approximations have to be made.

When it comes to the low-energy cross-section for pion photoproduction, in the literature the knowledge of the relation between the differential cross-section $d\sigma/d\Omega$ and the *multipole* E_{0+} is often assumed, along with the knowledge that the threshold amplitude is primarily *S-wave*. However, the way these statements and definitions are connected may not be clear immediately. The discussion that follows aims to lay out these connections in simple terms. The involved mathematics is rather advanced and therefore not followed here, the aim is to establish a connection between the different statements and quantities in a qualitative manner.

First of all, the invariant amplitude $\mathcal{M}$ of Eq. (1.1) for pion photoproduction can be parametrised in many ways. One of the more famous parametrisations is that of Chew, Goldberger, Low and Nambu [3], but alternatives exist, e.g. [4, 5]. The connections between the different parametrisations are laid out in Ref. [6]. The idea of Ref. [3] is that by using the most general properties of the scattering matrix of pion photoproduction, such as the demand for Lorentz invariance, and the spin structure of the initial and final states, the invariant amplitude can be written as a linear combination of four terms. Each term contains a structure built out of the photon polarisation vector $\boldsymbol{\epsilon}$, the Pauli matrices $\boldsymbol{\sigma}$ and the photon and pion three-momenta $\mathbf{k}$, $\mathbf{q}$. Qualitatively the parametrisation of the invariant amplitude $\mathcal{M}$ can be written as

$$\mathcal{M} = \sum_{i=1}^{4} \mathcal{F}_i \times (\text{combination of } \boldsymbol{\epsilon}, \boldsymbol{\sigma}, \mathbf{k}, \mathbf{q}), \tag{1.2}$$

where $\mathcal{F}_i$ are functions of W and $\cos\theta$, where θ is the angle between the initial photon and the final pion in the center-of-momentum frame. After establishing that such a parametrisation is possible, the structure functions $\mathcal{F}_i$ are expanded in terms of the multipoles $E_{l\pm}, M_{l\pm}$ and the Legendre polynomials $P_l(\cos\theta)$, such that the angular dependence of $\mathcal{F}_i$ is encoded in the Legendre polynomials and the energy dependence is carried by the multipoles. The multipoles $E_{l\pm}, M_{l\pm}$ refer to electric and magnetic transitions, respectively, and depend on the center-of-momentum energy W. The subscript $l\pm$ denotes the total angular momentum $j = l \pm 1/2 \equiv l\pm$ of the final state pion-nucleon system, where l is the relative orbital angular momentum between the pion and the nucleon [3, 6].

Through the parametrisation and expansions discussed above, the differential cross-section (1.1) becomes dependent on the multipoles $E_{l\pm}, M_{l\pm}$ and the Legendre polynomials $P_l(\cos\theta)$. Only the term $i = 1$ of Eq. (1.2) has no dependence on the pion momentum $\mathbf{q}$. Hence, at threshold ($\mathbf{q} \to 0$) only the structure function $\mathcal{F}_1$ survives. The structure function $\mathcal{F}_1$ reads [1]

$$\mathcal{F}_1 = \sum_{l=0}^{\infty} \left\{ \left[l M_{l+} + E_{l+} \right] P'_{l+1}(\cos\theta) + \left[(l+1) M_{l-} + E_{l-} \right] P'_{l-1}(\cos\theta) \right\}, \tag{1.3}$$

where $P'_{l\pm1}(\cos\theta) \equiv \frac{d}{d(\cos\theta)} P_{l\pm1}(\cos\theta)$. At threshold the relative angular momentum of the pion-nucleon system is expected to be $l = 0$ and the first term of the series in Eq. (1.3) dominates. This can also be understood intuitively, as the relative orbital angular momentum of a two-body system is correlated with the total energy in the system. At threshold the kinetic energy in the system is low, hence it is reasonable to expect that the relative angular momentum of the final state pion-nucleon system is $l = 0$. At threshold Eq. (1.3) reduces to

$$\begin{aligned} \mathcal{F}_1 &= E_{0+} P'_1(\cos\theta) + (M_{0-} + E_{0-}) P'_{-1}(\cos\theta) + \sum_{l=1}^{\infty} ... \\ &= E_{0+} + \sum_{l=1}^{\infty} ... \\ &\approx E_{0+}. \end{aligned} \tag{1.4}$$

Thus the relation between the threshold π^- photoproduction cross-section and the E_{0+} amplitude emerges.

The terminology of S-wave, P-wave, D-wave, F-wave dates back more than a hundred years and first emerged in the spectral analysis of alkali metals. The letters stood for “sharp”, “principal”, “diffuse” and “fundamental” and gave a qualitative description of the observed spectral lines. The association to the quantum number l of the angular momentum comes through relating the lines with the electron orbits in the atom [7]. The S-wave stands for orbital angular momentum $l = 0$, the P-wave for $l = 1$ etc. In the context of pion photoproduction, S-wave, P-wave, etc. refer to the orbital angular momentum of the final state pion-nucleon system.

Finally, when the energy of the incident photon increases above threshold the P-waves ($l = 1$) also start to contribute. The differential cross-section including the P-waves is given in Refs. [1, 8] and reads

$$\frac{d\sigma}{d\Omega} = \frac{|\mathbf{q}|}{|\mathbf{k}|} \left(A + B\cos\theta + C\cos^2\theta \right), \tag{1.5}$$

where

$$A = |E_{0+}|^2 + \frac{1}{2}(|P_2|^2 + |P_3|^2), \tag{1.6}$$

$$B = 2\mathrm{Re}(E_{0+} P_1^*), \tag{1.7}$$

$$C = |P_1|^2 - \frac{1}{2}(|P_2|^2 + |P_3|^2) \tag{1.8}$$

and

$$
\begin{aligned}
P_1 &= 3E_{1+} + M_{1+} - M_{1-}, &(1.9)\\
P_2 &= 3E_{1+} - M_{1+} + M_{1-}, &(1.10)\\
P_3 &= 2M_{1+} + M_{1-}. &(1.11)
\end{aligned}
$$

The total cross-section becomes

$$
\sigma_{\mathrm{tot}} = 4\pi \frac{|\mathbf{q}|}{|\mathbf{k}|} \left(|E_{0+}|^2 + |M_{1-}|^2 + 6|E_{1+}|^2 + 2|M_{1+}|^2 \right). \tag{1.12}
$$

1.1.2 Low-Energy Theorem (LET) approach

The first predictions for the pion photoproduction amplitudes on the nucleon near threshold were calculated in the so-called Low-Energy Theorem (LET) approach. An example that is often given to explain the nature of a LET is that of the Thomson limit to Compton scattering [5, 9]. In this case the transition matrix element T that describes the differential cross-section for the scattering $\gamma + N \rightarrow \gamma' + N'$ is expanded into a Taylor series in the parameter $\delta = |\mathbf{k}|/M$, where $|\mathbf{k}|$ is the photon energy and M is the nucleon mass. The first term in the series represents the Thomson amplitude that can be calculated using classical electrodynamics. In this example, the Low-Energy Theorem is a mathematical proof that the quantum mechanical calculation equals the Thomson amplitude in the limit where the photon energy goes to zero $|\mathbf{k}| \rightarrow 0$. The Low Energy Theorems associated with Compton scattering are discussed in detail in references [10, 11].

Qualitatively, similar ideas can be applied to pion photoproduction. However, in this case the transition amplitude is expanded in the parameter $\mu = m_\pi/M$, where m_π is the pion mass in the limiting case of massless pions (also referred to as "soft pions"). This was first done by Kroll and Ruderman in 1954 [12]. In that famous article they proved a theorem that enabled a connection to be made between the photoproduction cross-section and the pion-nucleon coupling constant. Given the value of the pion-nucleon coupling constant $g_{\pi N}$, the LET approach predicts the E_{0+} multipoles at threshold for the π^- and π^+ channels. The Feynman diagram of the Kroll-Ruderman term is depicted in Figure 1.2. More detail can be found in Ref. [12] and later reviews of the theorem presented in Refs. [2, 5].

Although the Kroll-Ruderman term dominates the threshold photoproduction amplitude of charged pions, it vanishes for neutral pion photoproduction in the limit

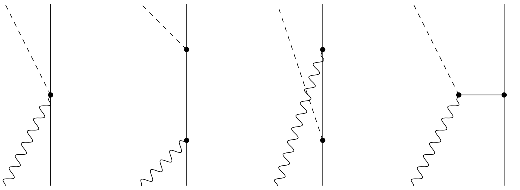

Figure 1.2: Leading order Feynman graphs of pion photoproduction. Solid line - nucleon, wave line - photon, dashed line - pion. From the left: 1. The Kroll-Ruderman term, 2. direct nucleon pole term, 3. crossed nucleon pole term, 4. pion pole term [5].

$\mu \to 0$. Expanding the LET calculations to higher order in the expansion parameter μ was complicated and led to a noticeable discrepancy between the theory predictions [2] and experimental data [13, 14] for the neutral pion channel. An interesting discussion of the various difficulties that arise in higher order expansions is presented in Ref. [9].

1.1.3 Dispersion theory approach

Close to the time the Kroll-Ruderman theorem (Section 1.1.2) was published, it became apparent that the pion photoproduction amplitude cannot be calculated perturbatively from meson theory due to the high value of the pion-nucleon coupling constant. This led theorists to develop non-perturbative methods, one of which has become known as dispersion theory. The name originates from optics. An equation that gives the real part of the index of refraction as an integral over its imaginary part was referred to as a “dispersion relation”, because it is related to the dispersion of light in a medium (see Section 10.8 of Ref. [15] and references therein). The development of dispersion relations for the pion-nucleon system originates from an article by Gell-Mann, Goldberger and Thirring [16], where the scattering of a spin-0 particle from a force center is considered. This work was extended by Goldberger by developing a dispersion relation for the forward pion-nucleon scattering amplitude [17, 18].

More recent dispersion theory calculations for the threshold E_{0+} amplitudes of π^-, π^0 and π^+ photoproduction were performed in Ref. [8]. In that article the procedure to numerically solve the dispersion relation integrals introduced 10 free parameters that were extracted from fits to experimental data. The fits were performed in the energy interval $160\,\mathrm{MeV} \leq E_\gamma \leq 420\,\mathrm{MeV}$, such that the threshold behaviour of the multipoles was extrapolated from the dispersion integrals that were evaluated above the threshold region. The details of the calculations are outlined in Ref. [19].

Dispersion theory techniques remain relevant to this day, for instance they provide important input [20] in determining the *low-energy constants* (see below) of Chiral Perturbation Theory. The latter has been very successful in describing many aspects of low-energy hadron physics and is discussed in the following subsection.

1.1.4 Chiral Perturbation Theory approach

New ideas about low-energy nuclear physics started to surface in the 1960s. Through the work of Nambu [21, 22] and Goldstone [23, 24] emerged the interpretation of pions as nearly massless Goldstone bosons of the nuclear force. This led to the effective Lagrangian approach by Weinberg [25] in 1967, which offered a simpler calculation method compared to the techniques employed up to that time. Approximately a decade later it was again pointed out by Weinberg that the effective Lagrangian approach can be linked formally with the underlying field theory of the strong interaction. Using these ideas Chiral Perturbation Theory (ChPT) was formulated [26, 27, 28]. A modern pedagogical review of ChPT is provided in Refs. [29, 30]. An important part in the ChPT concept is played by the QCD Lagrangian in the *chiral limit*, hence the name of the theory. Due to its importance, the chiral limit of QCD and its implications are discussed separately in the next paragraph. Then the basic principles of constructing an effective Lagrangian and the emergence of *Low Energy Constants* are reviewed.

Finally a discussion of various chiral models and their predictions for the π^- photoproduction process are summarised. Some of the aspects of this subsection are treated at a somewhat greater length in Ref. [31].

Emergence of the low-energy hadron spectrum from QCD

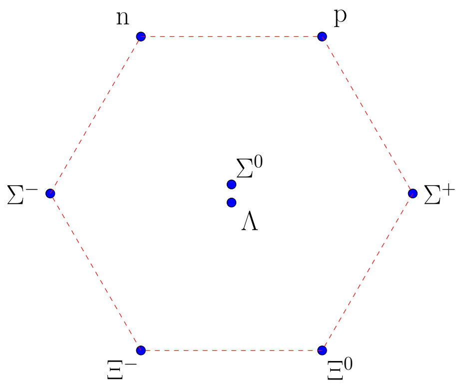

Figure 1.3: The lightest baryon octet.

From the viewpoint of QCD, the low energy hadron spectrum emerges from the QCD Lagrangian in the low-energy limit where the three heavier quarks (*charm, top, bottom*) are neglected and the masses of the three lightest quarks are taken to be zero. In this limit (referred to as the *chiral limit*) the QCD Lagrangian separates into left-handed and right-handed fields. Applying Noether's theorem to the Chiral Lagrangian leads to the prediction of flavour multiplets, e.g. the well-known lowest lying baryon octet depicted in Figure 1.3. The full symmetry group of the QCD Lagrangian in the chiral limit reads

$$\mathrm{SU}(3)_\mathrm{V} \times \mathrm{SU}(3)_\mathrm{A} \times \mathrm{U}(1)_\mathrm{V}, \tag{1.13}$$

where V and A stand for vector and axial-vector transformations. From this symmetry group one expects to observe parity doublets of the flavour multiplets, e.g. the lowest-lying vector meson multiplet (Figure 1.4) should have, according to the symmetry group (1.13), a parity doublet of axial-vector mesons of similar masses. The fact that such multiplets have not been observed is interpreted as evidence that the axial-vector symmetry is *spontaneously broken*. Shortly put, this means that the Chiral QCD Lagrangian is symmetric under the full group of (1.13), whereas the QCD ground state does not have the $\mathrm{SU}(3)_\mathrm{A}$ symmetry. For more details on the spontaneous symmetry breaking the reader is referred to [29]. The spontaneous symmetry breaking leads to the identification of the pseudoscalar meson multiplet (Figure 1.5) as the Goldstone bosons of the theory. In addition, the chiral symmetry is also explicitly broken by the non-vanishing quark masses, causing the flavour multiplets to be only approximately degenerate in mass. For example without explicit symmetry breaking the vector mesons in Figure 1.4 would have equal mass.

It should be noted that historically the SU(3) flavour symmetry of the low-energy hadron spectrum was observed before Quantum Chromodynamics - the quantum field theory of the strong interaction - was formulated. This dates back to the work of Gell-Mann and the so-called “eightfold way” [32]. However, from the viewpoint of modern nuclear physics it is elegant to see the hadron spectrum emerging from the underlying theory of QCD in the approximation of massless up, down and strange quarks.

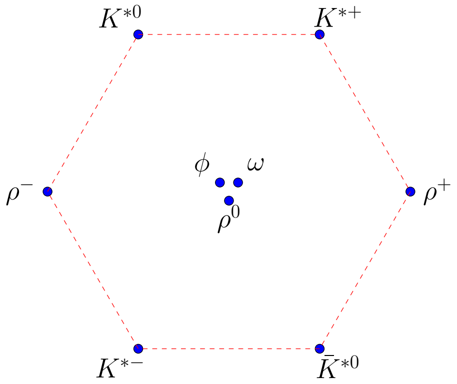

Figure 1.4: Vector meson nonet.

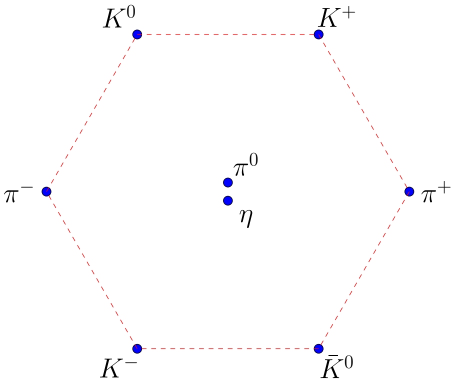

Figure 1.5: Pseudoscalar meson octet.

The effective Lagrangian

The goal of the effective field theory approach is accurate description of low energy hadronic reactions. Because of the high value of the QCD coupling constant in the ~ 1 GeV region, hadrons rather than quarks act as relevant degrees of freedom. In general terms, the effective Lagrangian is constructed such that:

1. Hadrons, instead of quarks act as degrees of freedom.
2. The effective ChPT Lagrangian respects the same symmetry as the QCD Lagrangian in the chiral limit.
3. The effective Lagrangian should include “all possible terms”.
4. The expansion to higher orders (more precise results) is done in energies and momenta, rather than in the coupling constant.
5. The effective theory holds only in a certain energy domain.

The first condition means that the Lagrangian contains hadron fields, such as pions and kaons, instead of elementary quark fields. The second condition states that the effective Lagrangian has the spontaneously broken symmetry group of (1.13), like the QCD Lagrangian in the chiral limit. The conditions $3-5$ are best explained with the help of an example. For instance, to describe Compton scattering from the nucleon, one should include a term in the Lagrangian that corresponds to the lowest-order diagram (left in Figure 1.6), a term that corresponds to a diagram with the pion propagator (right in Figure 1.6) etc. (condition 3). Each term of the Lagrangian comes with a phenomenological low-energy constant (LEC) and in principle the number of terms

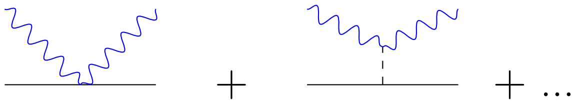

Figure 1.6: Example Feynman diagrams depicting Compton scattering from the nucleon (image from Ref. [33]). Leading order diagram (left) and an example higher order diagram (right). Solid line - nucleon, wave line - photon, dashed line - pion.

(and corresponding Feynman diagrams) is infinite. In ChPT the expansion to higher orders is made in p/Λ (condition 4), where p is a small momentum, mass or energy compared to the scale factor $\Lambda \sim 1$ GeV. Thus the theory is valid in the range where condition $p \ll \Lambda$ is met (condition 5). Recall that this is different in a fundamental quantum field theory such as Quantum Electrodynamics, where the expansion to higher orders is done in the small coupling constant $\alpha = 1/137$. In Weinberg's power counting scheme [26] the right-hand diagram of Figure 1.6 is higher order in p/Λ when compared to the left-hand diagram. Thus as long as the assumption $p \ll \Lambda$ is valid, the right-hand diagram will act as a higher order correction to the left-hand diagram. The leading order contributions in the p/Λ expansion will dominate, resulting in a drastic reduction in the number of terms required in the Lagrangian. The power counting and the effective Lagrangian are discussed in more detail in Refs. [1, 6] and at length in Refs. [29, 30].

Low-energy constants

The LECs can be viewed as a parametrisation of the underlying theory (QCD). Therefore in principle the LECs can be calculated from Quantum Chromodynamics, but solving QCD in the low energy region is difficult (hence the emergence of effective field theories, dispersion theories etc). Due to advancements in Lattice QCD some of the LECs can now be evaluated from first principles [34, 35], but the bulk of the LECs that are relevant for the ChPT prediction of the pion photoproduction amplitude need to be determined from experimental data. Once the LECs for a given order in the p/Λ expansion have been determined, the theory becomes predictive. The extraction of the LECs from experimental data is discussed in detail in Ref. [6].

Chiral models

In its simplest, purely mesonic form the ChPT Lagrangian contains only the pseudoscalar mesons (the Goldstone bosons) and for example can be used to describe pion-pion rescattering. In order to describe pion photoproduction on the nucleon, the baryon fields must be incorporated as well as the electromagnetic fields. Chiral Perturbation Theory including baryons divides into Heavy-Baryon Chiral Perturbation Theory (HBChPT) and Relativistic Chiral Perturbation Theory (RChPT). This separation has to do with subtle differences in the treatment of baryon fields and higher order corrections and is beyond the scope of this work. The interested reader is referred to the introduction of Ref. [1] and references therein. The RChPT predictions of Ref. [6] are available through a web interface (called MAID) [36] and provide values for the threshold E_{0+} multipoles and the cross-sections for pion photoproduction. The HBChPT prediction for the E_{0+} multipoles is presented in Ref. [37].

In addition to RChPT and HBChPT, other chiral models exist. One relatively recent development is that by Gasparyan and Lutz [38]. Their work is also based on a chiral Lagrangian and is part of an effort to extend the applicability of hadronic effective field theories to higher energies. Their article also presents predictions for the E_{0+} multipoles at threshold.

1.1.5 SAID approach

The predictions of the previous subsection are based on the underlying ChPT model. An alternative analysis is available by the so-called Scattering Analysis Interactive Dial-in (SAID) program [39, 40]. In the SAID program the helicity amplitude formalism of Ref. [41] is used, where four helicity amplitudes $H_i(\theta)$ are expanded in terms of the multipoles $E_{l\pm}, M_{l\pm}$ already discussed in 1.1.1. The differential cross-section is given through the helicity amplitudes as

$$\frac{d\sigma}{d\Omega} = \frac{|\mathbf{q}|}{2|\mathbf{k}|} \sum_{i=0}^{4} |H_i(\theta)|^2, \tag{1.14}$$

where $\mathbf{k}$ and $\mathbf{q}$ are the photon and pion momentum, respectively. A detailed discussion of the structure and form of the helicity amplitudes is given in Refs. [41, 42]. In the SAID approach the multipoles are parametrised in an energy-dependent way and determined by fits to experimental data. Then, after the multipole structures have been extracted from the fits, the helicity amplitudes are calculated, which in turn allow calculation of observables, such as the cross-section in Eq. (1.14). In the SAID parametrisation there is no clear physical interpretation of the fit parameters, the main goal is to understand the nucleon resonance structure through a phenomenological description of the multipoles.

1.1.6 Summary of predictions by various models

In this subsection the various predictions by the models of Sections 1.1.2 – 1.1.5 related to threshold π^- photoproduction are summarised. It should be stressed that all these models describe the reaction $\gamma + n \to \pi^- + p$, i.e. they assume a free neutron target. The implications of using a neutron bound into ^{2}H are discussed in the next subsection.

The various predictions for the E_{0+} multipole for threshold π^- photoproduction are outlined in Table 1.1. The table reveals very good consistency between different models. The predicted multipole values are sensitive to the pion-nucleon coupling constant $g_{\pi N}$, thus each prediction is accompanied with the corresponding coupling constant value that was used in the calculation. The only noticeable difference is that the magnitudes of RChPT and HBChPT predictions seem to be slightly higher compared to the other models.

Threshold $\mathbf{E_{0+}}$ predictions of $\boldsymbol{\gamma n \to \pi^- p}$

Model	$E_{0+} \cdot 10^{-3}/m_{\pi^+}$	$g_{\pi N}$	Reference
LET	-31.7	13.4	[12, 8]
Dispersion th.	-31.67	13.4	[8]
HBChPT	-32.7 ± 0.6	14.28	[37]
RChPT	-32.87	13.21	[6, 36]
Gasparyan-Lutz	-31.5	13.54	[38]

Table 1.1: Summary of various predictions for the E_{0+} multipole for the $\gamma n \to \pi^- p$ reaction at threshold.

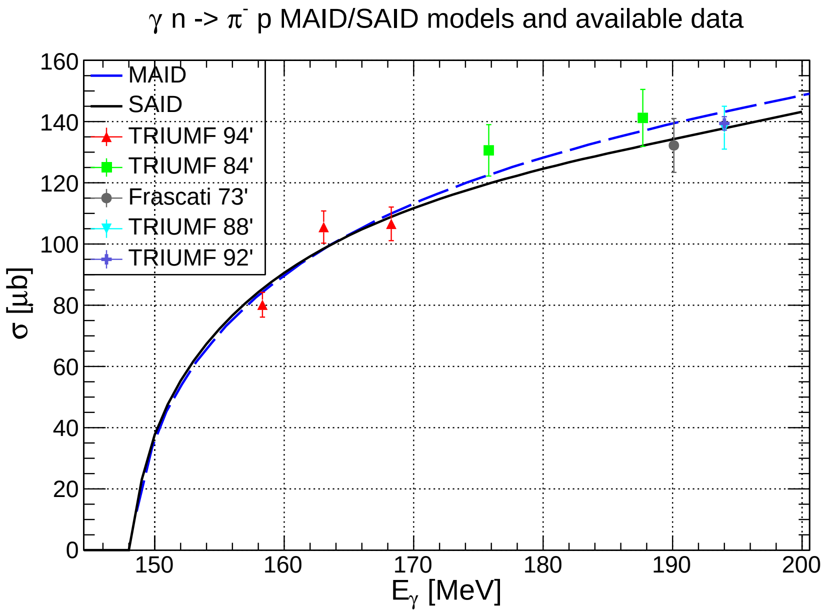

Figure 1.7: MAID and SAID predictions for the reaction $\gamma \mathrm{n} \to \pi^- \mathrm{p}$ from threshold to $E_\gamma \leq 200$ MeV. The experimental data points are discussed in Section 1.1.8.

In addition to the E_{0+} multipole predictions, the MAID [36] and SAID [40] analyses provide values for the total cross-section $\sigma(E)$. The predicted cross-sections, alongside available measured data points, are depicted in Figure 1.7. The data points are treated in further detail separately in Section 1.1.8. The figure reveals very good agreement between the two models, but significantly there are no previous measurements close to the threshold region. The new results presented in this thesis will be an important consistency test for the MAID and SAID predictions in that region.

1.1.7 The deuteron target - on the role of the final state interactions

As has already been stressed, the models of Sections 1.1.2 – 1.1.5 assume a free neutron target. In practice a neutron bound in a light nucleus has to be used. The simplest such nucleus is the deuteron with a bound proton and a neutron. In π^- photoproduction on the deuteron, the π^- is produced on the neutron in the process $\gamma \mathrm{n} \to \pi^- \mathrm{p}$. However, the bound nature of the target nucleon and the presence of the second proton in the final state have a considerable effect on the cross-section for the reaction $\gamma + {}^2\mathrm{H} \to \pi^- + 2\mathrm{p}$ compared to the elementary reaction $\gamma \mathrm{n} \to \pi^- \mathrm{p}$. The final-state proton-proton and pion-proton scattering are referred to as Final State Interactions (FSI).

The theoretical treatment of FSI effects is complicated and extraction of the elementary cross-section from deuteron data is non-trivial. One way of achieving this is proposed in a recent article by Tarasov *et. al.* [43].

On the other hand a model for the elementary amplitude is necessary to understand π^- photoproduction on the deuteron. This can for example be obtained from MAID or SAID. If the amplitude of the elementary process is assumed to be correct, the π^- photoproduction on the deuteron becomes an important test for our understanding of the final state interactions. Tarasov employs the elementary amplitude from SAID to provide a prediction for the reaction $\gamma + {}^2\text{H} \rightarrow \pi^- + 2\text{p}$ over a wide energy range. Additionally, it is also interesting to note that a ChPT based calculation for the alternative isospin channel $\gamma + {}^2\text{H} \rightarrow \pi^+ + 2\text{n}$ in the threshold region has been performed by Lensky *et. al.* [44]. Although π^- and π^+ photoproduction on the deuteron are very similar processes, the theoretical treatment of the former is complicated by the Coulomb interaction between proton-proton and π^--proton final states. A comparison between the π^+ channel prediction [44] and the π^- channel measurement of this thesis could provide an initial insight into the strength of the final state Coulomb interaction [45]. Both the predictions from Tarasov and Lensky are shown alongside the measurements of this thesis in Chapter 5.

1.1.8 Overview of previous measurements

There are only a handful of measurements that have probed π^- photoproduction in the threshold region. Limiting this overview to the region from threshold to $E_\gamma < 200$ MeV and to experiments performed from 1950 onwards, there are in total 51 measured differential cross-section points for the π^- channel, 83 for the π^+ channel and 1432 for the π^0 channel [40]. All three datasets were comparable in size until the 1990s, but the extensive measurements by Fuchs *et. al.* [46] and Bergstrom *et. al.* [47, 48, 49] in mid-nineties and more recently by Hornidge *et. al.* [50], alongside numerous other experiments, have drastically increased the π^0 database. On the other hand, there have been no extensive measurements performed for the charged channels, with the last π^- data from 1994 and the last π^+ data from 1999.

Frascati 1973

The first measurement of π^- photoproduction below $E_\gamma < 200$ MeV was performed by Rossi *et. al.* in 1973 at Frascati [51]. The lowest photon energy in their experiment was 190.1 MeV. Electrons incident on a Ta sheet created a bremsstrahlung beam [52] and LiH beam hardeners were employed to preferentially suppress the low energy part of the bremsstrahlung continuum. The photon beam was incident on a bubble chamber where the events $\gamma + {}^2\text{H} \rightarrow \pi^- + 2\text{p}$ were registered and the incident flux was measured by monitoring $\gamma \rightarrow e^+e^-$ pair production in the chamber. The cross-section for the elementary reaction $\gamma\text{n} \rightarrow \pi^-\text{p}$ was extracted by using the spectator model, combined with Monte-Carlo techniques for event identification.

TRIUMF 1984 and 1988

In 1984 Salomon *et. al.* [53] used a pion beam at TRIUMF [54] to measure the differential cross-sections for the reactions $\pi^-\text{p} \rightarrow \gamma\text{n}$ and $\pi^-\text{p} \rightarrow \pi^0\text{n}$. Negative pion capture on the proton $\pi^-\text{p} \rightarrow \gamma\text{n}$ can be directly related to the photoproduction reaction $\gamma\text{n} \rightarrow \pi^-\text{p}$ [55]. At TRIUMF a 33 MeV and 44 MeV π^- beam was incident on a liquid hydrogen target, which translates into corresponding photon beam energies $E_\gamma = 175.8$ MeV and $E_\gamma = 187.7$ MeV for the inverse reaction. A NaI(TI) detector was used to detect photons from π^- capture and π^0 decay at angles from 30° to 145°

by varying the position of the detector. Differential cross-section points were obtained at energies equivalent to $E_\gamma = 175.8$, 187.7 MeV.

In 1988 Bagheri *et. al.* [56] used a similar experimental setup to probe higher energies. However, their lower energy points have more background contamination compared to [53]. Bagheri *et. al.* extracted the differential cross-section at an energy equivalent to $E_\gamma = 194$ MeV. Interestingly, at an energy equivalent to $E_\gamma = 211$ MeV Bagheri *et. al.* and Rossi *et. al.* data agree relatively well in the angle range from 60° to 120°, but a discrepancy emerges at backward and especially at forward angles. The reasons for this are not explained, but it may have been caused by unaccounted FSI in the analysis by Rossi *et. al.*

TRIUMF 1992 and 1994

In the experiments of Refs. [53, 56] the equivalent photon energy E_γ was well above threshold, meaning strong contributions from multiple partial waves. Thus these data are of limited value in determining the multipole E_{0+} at threshold. Further measurements on the inverse reaction were performed at TRIUMF in 1992 by Wang [57] and in 1994 by Liu [58]. However it proved impossible to source these unpublished theses and the results were obtained from the SAID website [40]. Liu took data at energies equivalent to $E_\gamma = 158.32$, 163.05 and 168.27 MeV, where the lowest energy overlaps with the present experiment. However, it should be kept in mind that the results presented in this thesis measure the π^- photoproduction on the deuteron, meaning the amplitude of the elementary process $\gamma \mathrm{n} \rightarrow \pi^- \mathrm{p}$ will first have to be properly extracted before any comparisons with Ref. [58] can be made.

1.2 Compton scattering

Compton scattering from electrons has been known for ∼100 years [59]. The first Compton scattering measurements on nuclei were performed at the end of the 1940s [60, 61] and by now a wealth of experiments and theoretical interpretations are available, with several exhaustive reviews written in the last ∼15 years [62, 63, 64, 65]. In the context of Compton scattering on light nuclei and neutron polarisabilities, the relevant theoretical treatment is provided by an extended HBChPT framework [65] and therefore that review is followed throughout this section. Section 1.2.1 explains the nature of the nucleon polarisability observables. Section 1.2.2 sketches how the sensitivity of the differential Compton scattering cross-section to the nucleon polarisabilities emerges. In Section 1.2.3 the present values for the neutron polarisabilities are given and the use of light nucleus targets for the extraction of the neutron polarisabilities is discussed. Finally, Section 1.2.4 finishes this section with an overview of previous experiments. The basic concepts of a chiral effective field theory, such as the HBChPT relevant for Compton scattering on the deuteron, are already provided in Section 1.1.4 and are thus not discussed here.

1.2.1 Nucleon polarisabilities

Nucleon polarisabilities are nucleon structure observables that characterise the nucleon response to an external electromagnetic (EM) excitation. Polarisation arises because the external field displaces the charge constituents of the nucleon, which creates charge and current multipoles. The dominant polarisabilities are the *electric dipole* $\alpha_{E1}(E_\gamma)$ and the *magnetic dipole* $\beta_{M1}(E_\gamma)$. Cartoons of the electric and magnetic dipole polarisabilities are depicted in Figures 1.8 and 1.9, where an external electromagnetic field creates displacements of the charge constituents of the nucleon, leading to electric and magnetic dipole moments. The electric and magnetic multipoles that have been created by the external electromagnetic excitation re-radiate at the same frequency as the EM field that induced the polarisation. The polarisabilities $\alpha_{E1}(E_\gamma)$ and $\beta_{M1}(E_\gamma)$ characterise the strength of the dipole radiation relative to the incident electromagnetic field. As different multipolarities have different angular distributions, the polarisabilities can be extracted from differential cross-section measurements. In

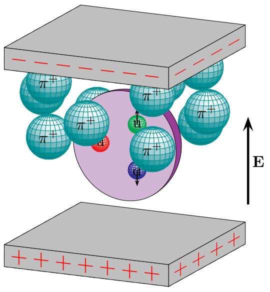

Figure 1.8: Nucleon and the surrounding pion cloud in an external electric field [66].

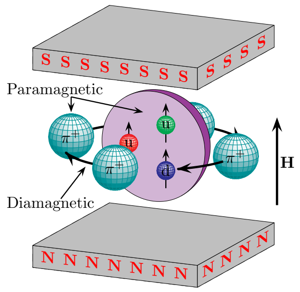

Figure 1.9: Nucleon and the surrounding pion cloud in an external magnetic field [66].

addition to the dipole polarisabilities there are also spin polarisabilities, which characterise the nucleon spin response to an external EM field. In principle also quadrupole excitations and subsequent radiation modes are possible, but such contributions to the cross-section are negligible below $E_\gamma < 300$ MeV [65]. The polarisabilities for a particle without internal structure vanish, meaning these observables are tightly related to the properties and behaviour of the internal degrees of freedom of the nucleon. Usually, values for the *static polarisabilities* $\bar{\alpha}_{E1} \equiv \alpha_{E1}(E_\gamma \to 0)$ and $\bar{\beta}_{M1} \equiv \beta_{M1}(E_\gamma \to 0)$ are given in the literature. The energy dependent (*dynamical*) polarisabilities, $\alpha_{E1}(E_\gamma)$ and $\beta_{M1}(E_\gamma)$, are defined with an appropriate normalisation, such that they equal the static polarisabilities in the limit $E_\gamma \to 0$ [67, 68].

1.2.2 Kinematics and sensitivity to polarisabilities

The Compton scattering reaction $\gamma(k_i) + N(p_i) \to \gamma(k_f) + N(p_f)$ is depicted in Figure 1.10. In this case a photon with initial momentum k_i scatters from a nucleon with initial momentum p_i, resulting in a final photon with momentum k_f and final nucleon with momentum p_f. The shaded sphere stands for the interaction vertex. The energy of the scattered photon E'_γ is determined by the reaction kinematics and can be expressed in terms of the incoming photon energy E_γ, the scattering angle $\cos\theta$ and the target mass M as

$$E'_\gamma = \frac{ME_\gamma}{M + E_\gamma(1 - \cos\theta)}. \tag{1.15}$$

Generally, the differential cross-section for Compton scattering in the laboratory frame is [65]

$$\frac{d\sigma}{d\Omega} = \frac{1}{16\pi^2} \frac{M^2}{\left[M + E_\gamma(1 - \cos\theta)\right]^2} |T|^2, \tag{1.16}$$

where M is the target nucleus mass, E_γ is the incident photon energy and $\cos\theta$ is the laboratory angle between the incident and scattered photon. The scattering is described by the T-matrix. Similarly to the invariant amplitude $\mathcal{M}$ of Eq. (1.1), the T-matrix can be parametrised and written as a sum of independent invariant amplitudes. For the scattering of a photon from a spin-$\frac{1}{2}$ nucleon there are six amplitudes [69]. Thus

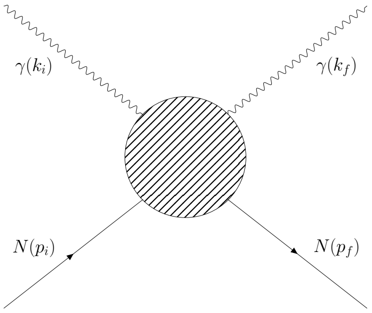

Figure 1.10: Compton scattering. Wave lines - initial and final photon, solid lines - initial and final nucleon.

the T-matrix can be written as [65]

$$T = \sum_{i=1}^{6} A_i(E_\gamma, \cos\theta) \times (\text{combination of } \boldsymbol{\epsilon}, \boldsymbol{\epsilon'}, \boldsymbol{\sigma}, \mathbf{k_i}, \mathbf{k_f}), \tag{1.17}$$

where $\boldsymbol{\epsilon}$ and $\boldsymbol{\epsilon'}$ are the polarisations of the initial and final photon, $\boldsymbol{\sigma}$ is the polarisation of the nucleon and $\mathbf{k_i}$, $\mathbf{k_f}$ are the momenta of the initial and final photon. Comparing Eq. (1.17) with Eq. (1.2) reveals that more invariant amplitudes are necessary to parametrise the T-matrix of Compton scattering compared to the matrix element $\mathcal{M}$ of pion photoproduction. This stems from the extra degrees of freedom in the Compton scattering process carried by the spin of the final photon (spin ± 1), whereas the final state pion is a pseudoscalar (spin 0). In the limit $E_\gamma \to 0$ the transition matrix reduces to the classical Thomson scattering limit, as discussed in 1.1.2. The Thomson limit obviously does not contain any polarisabilities and in this sense the low-energy limit illustrates nicely how the Compton scattering cross-section becomes sensitive to the internal degrees of freedom of the nucleon only for sufficiently high incident photon energies ($E_\gamma \gtrsim 50$ MeV). From the theoretical viewpoint, this allows separation of the amplitudes A_i of Eq. (1.17) into structure dependent and structure independent (often referred to as “Born” or “pole”) terms

$$A_i(E_\gamma, \cos\theta) = A_i^{\text{Born}}(E_\gamma, \cos\theta) + \bar{A}_i(E_\gamma, \cos\theta). \tag{1.18}$$

Denoting $E_\gamma \equiv \omega$ and $\cos\theta \equiv z$, the structure dependent parts up to order ω^3 are given as

$$\begin{aligned}
\bar{A}_1(\omega, z) &= 4\pi \left[\alpha_{E1}(\omega) + z\beta_{M1}(\omega)\right]\omega^2 + ... \\
\bar{A}_2(\omega, z) &= -4\pi\beta_{M1}(\omega)\omega^2 + ... \\
\bar{A}_3(\omega, z) &= -4\pi \left[\gamma_{E1E1}(\omega) + z\gamma_{M1M1}(\omega) + \gamma_{E1M2}(\omega) + z\gamma_{M1E2}(\omega)\right]\omega^3 + ... \\
\bar{A}_4(\omega, z) &= 4\pi \left[-\gamma_{M1M1}(\omega) + \gamma_{M1E2}(\omega)\right]\omega^3 + ... \\
\bar{A}_5(\omega, z) &= 4\pi\gamma_{M1M1}(\omega)\omega^3 + ... \\
\bar{A}_6(\omega, z) &= 4\pi\gamma_{E1M2}(\omega)\omega^3 + ... \,.
\end{aligned} \tag{1.19}$$

In the equations above the γ’s are the spin polarisabilities discussed in the previous subsection. Eqs. (1.16) – (1.19) outline how the sensitivity of the differential cross-section (1.16) to the nucleon polarisabilities emerges. It is worth noting that the dipole polarisabilities $\alpha_{E1}(E_\gamma)$ and $\beta_{M1}(E_\gamma)$ enter at order E_γ^2, one order lower than the spin polarisabilities, making the experimental determination of the latter more difficult.

The latest determination of the proton polarisabilities was performed by McGovern *et. al.* [33], yielding

$$\begin{aligned}
\bar{\alpha}_{E1}^{(p)} &= 10.65 \pm 0.35(\text{stat}) \pm 0.2 \pm 0.3(\text{theory}), \\
\bar{\beta}_{M1}^{(p)} &= 3.15 \mp 0.35(\text{stat}) \pm 0.2 \mp 0.3(\text{theory}).
\end{aligned} \tag{1.20}$$

Here and onward the polarisabilities are given in the standard units of $10^{-4}\,\text{fm}^3$ for α and $10^{-4}\,\text{fm}^4$ for β. Notably, in this analysis the statistical and theoretical uncertainty have almost equal magnitude. The subjects considered in this subsection are discussed in further detail in Ref. [65] and at length in Ref. [67].

1.2.3 Neutron polarisabilities and light nucleus targets

In Sections 1.2.1 and 1.2.2 the Compton scattering from a free nucleon was described. As already mentioned, there is no free neutron target and so the bulk of the Compton scattering data - and the associated polarisability determinations - have been measured on a proton target. For neutron experiments light nucleus targets, such as the deuteron, have to be used. A recent determination of the neutron polarisabilities by Myers *et. al.* [70, 71] from coherent Compton scattering on the deuteron gave

$$\begin{aligned}\bar{\alpha}_{E1}^{(n)} &= 11.55 \pm 1.25(\text{stat}) \pm 0.2 \pm 0.8(\text{theory}),\\ \bar{\beta}_{M1}^{(n)} &= 3.65 \mp 1.25(\text{stat}) \pm 0.2 \mp 0.8(\text{theory}).\end{aligned} \tag{1.21}$$

Comparison between (1.20) and (1.21) reveals that the neutron polarisabilities are less precisely known. Moreover, as outlined in the discussion of Ref. [70], extending the formalism of Ref. [33] to the deuteron calculations should further constrain the theoretical uncertainty, clearly indicating the necessity for improved measurements towards the neutron polarisabilities. It should be noted that the values quoted in (1.20) and (1.21) differ somewhat from the values given by the Particle Data Group [72]. The latter calculates the world average values from different techniques, whereas the results (1.20) and (1.21) rely on the extended HBChPT method discussed in Ref. [65] and references therein.

The deuteron target

The extraction of the neutron polarisabilities from Compton scattering data on the deuteron is discussed at length in the PhD thesis [67] and the associated publications [73, 74, 75]. In case of the deuteron target the *isoscalar* polarisabilities

$$\bar{\alpha}_{E1}^{(s)} = \frac{1}{2}(\bar{\alpha}_{E1}^{(p)} + \bar{\alpha}_{E1}^{(n)}), \qquad \bar{\beta}_{M1}^{(s)} = \frac{1}{2}(\bar{\beta}_{M1}^{(p)} + \bar{\beta}_{M1}^{(n)}) \tag{1.22}$$

are obtained and the neutron values are extracted by using the better known proton polarisabilities of Eq. (1.20). An example of a fit to the deuteron Compton scattering differential cross-section data that was used to extract the neutron polarisabilities is depicted in Figure 1.11. The theoretical treatment of the measured cross-section for the extraction of the neutron polarisabilities is not trivial and the reader is referred to the review [65]. The cited formalism has yet to be extended to the energy region where the experiment of this thesis is performed, but the new data will provide a strong incentive to make this extension. The sensitivity of the differential cross-section to the polarisabilities increases with E_γ, but above pion photoproduction threshold the influence of the $\Delta(1232)$ resonance increases, which complicates the theoretical treatment of the process. In this sense the Compton scattering data on the deuteron above the pion threshold will not only provide a valuable contribution to the global database for neutron polarisabilities, but also a test for the extended HBChPT formalism discussed in Ref. [65].

The ^{3}He target

It was first suggested in Refs. [76, 77, 78] that the differential cross-section for the Compton scattering reaction

$$\gamma + {}^3\text{He} \rightarrow \gamma' + {}^3\text{He}' \tag{1.23}$$

could also be treated in the HBChPT framework to extract information about the neutron polarisabilities. The sensitivity of the differential cross-section to the neutron polarisabilities is illustrated in Figure 1.12, which shows maximum effect at forward and backward angles. An experiment to use a Helium Gas Scintillator Active Target [79, 80], developed at The University of Glasgow, to measure the differential cross-section for reaction (1.23) has been approved to run at the tagged photon facility in Mainz [81]. This led to the development of a new prototype of the Active Target. The simulation work related to the new prototype development formed an important part of this PhD project and is summarised separately in Appendix B.

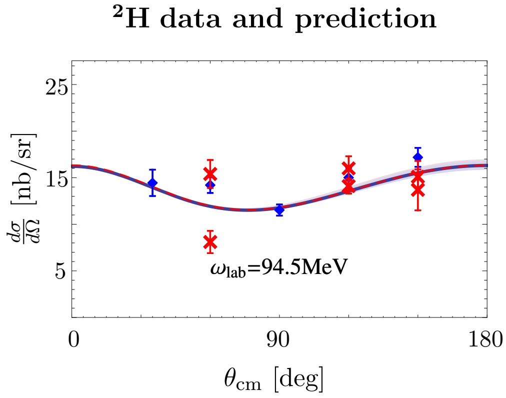
^{2}H data and prediction

Figure 1.11: Compton scattering $\frac{d\sigma}{d\Omega}$ on ^{2}H at $E_\gamma = 94.5$ MeV, data and model prediction. Cross: Lund 2015; diamond: Saskatchewan 2000. See Section 1.2.4 for data review. Solid (dashed) curve corresponding to one (two) parameter fit in the framework of Ref. [65]. Figure from Ref. [70].

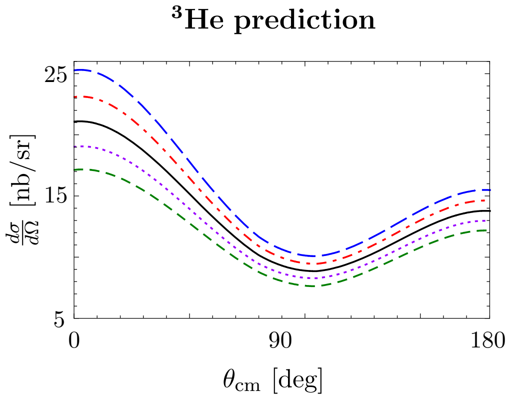
^{3}He prediction

Figure 1.12: Compton scattering $\frac{d\sigma}{d\Omega}$ on ^{3}He at $E_\gamma = 120$ MeV, model sensitivity to $\Delta\bar{\alpha}^{(n)}_{E1}$. Solid black: central value $\bar{\alpha}^{(n)}_{E1} = 12.2$; long dashed (blue): $\Delta\bar{\alpha}^{(n)}_{E1} = -4$; dot dashed (red): $\Delta\bar{\alpha}^{(n)}_{E1} = -2$; dotted (magenta): $\Delta\bar{\alpha}^{(n)}_{E1} = 2$; dashed (green): $\Delta\bar{\alpha}^{(n)}_{E1} = 4$. Figure from Ref. [65].

1.2.4 Overview of previous measurements

Only a few experiments have been performed in the range of photon energies where the deuteron Compton scattering cross-section is sensitive to the neutron polarisabilities. Data collected before the 1970's has been reviewed in Ref. [82] and will not be discussed here.

Illinois 1994

The first tagged photon Compton scattering measurement on a deuteron target was performed by Lucas in 1994 [83]. Scattered photons were detected at laboratory angles

50°, 75°, 110° and 140° by two large NaI(TI) crystals at a photon beam energy $E_\gamma =$ 49 MeV. Additionally, differential cross-section points at $E_\gamma = 69$ MeV were measured at laboratory angles 60° and 135°. Thus in total 6 differential cross-section points were extracted. The unpublished thesis of Ref. [83] is not publicly available, but some more details are provided in Ref. [65].

Saskatchewan 2000

Chronologically the next Compton experiment on the deuteron was performed by Hornidge *et. al.* [84, 85] at the Saskatchewan Accelerator Laboratory (SAL). At SAL a 135 MeV pulse-stretched electron beam was used to create a tagged photon beam in the energy range 84.4-104.6 MeV, that was incident on a liquid deuterium target. Compton scattered photons were detected with a large NaI(TI) detector at laboratory angles 35°, 60°, 90°, 120° and 150°. Although the SAL tagger has an energy resolution better than 1 MeV the data were averaged, due to the low counting rate, over the full range of the tagger resulting in one ∼20 MeV wide energy bin centred at $E_\gamma = 94.2$ MeV. The Compton scattering events were separated from the inelastic channel $\gamma^2\mathrm{H} \to \gamma\mathrm{np}$ using a photon detector with a high ($\sim 2\%$) energy resolution. Note that the SAL photon tagger and the NaI(TI) detector (named BUNI) were transferred to MAXLab in Lund, Sweden and were used in the present experiment.

Lund 2003

Shortly after the experiment by Hornidge *et. al.* a Compton scattering program started at MAXLab in Lund, Sweden (Lundin *et. al.* [86, 87]). A pulse-stretched electron beam with energy $E_e = 95$ MeV was used to create a tagged photon beam in the energy range $50 - 72$ MeV. The data were summed in two energy bins centred at 55 MeV and 66 MeV. Three separate NaI(TI) photon detectors were used to detect scattered photons at laboratory angles 45°, 125° and 135°, resulting in 6 differential cross-section points. The measurements in Lund and Illinois were in a similar energy range and the results of the two experiments were consistent.

Lund 2015

Soon after the results of Lundin were published the MAXLab facility was upgraded, resulting in higher energy electron and tagged photon beams. Compton scattering on the deuteron at incident photon energies reaching 115 MeV was performed by Myers *et. al.* [70, 71, 88]. There were several improvements compared to the earlier measurement by Lundin *et. al.* The SAL photon tagger was installed at Lund. The NaI(TI) detectors used by Lundin *et. al.* had diameter 25.4 cm and length 25.4 cm[1], with detector resolution around 6-8% for 60 MeV photons. Three new NaI(TI) detectors, one of which was the aforementioned BUNI from SAL, were available to Myers *et. al.* These detectors had substantially larger crystals and therefore the necessary energy resolution of about 2% for Compton signal separation at photon energies close to 100 MeV. The same detectors were used in the present experiment and further details are available in Section 2.1.3. In addition, the liquid deuterium target was improved to stop ice build-up

---

[1] Expect for one detector, which had length 35.5 cm

on the target, which constituted a significant source of background in the experiment by Lundin *et. al.* Finally, the Myers *et. al.* data is substantially more extensive. Differential cross-section points were measured at three laboratory angles 60°, 120° and 150° at 8 incident photon energies between 69.6 and 112.1 MeV, resulting in 23 new data points. The measurements by Myers *et. al.* more than doubled the database for Compton scattering on the deuteron. In Ref. [70] data from all the experiments discussed in this subsection were combined to extract the most up-to-date values of the neutron polarisabilities, given in Section 1.2.3. The data from Myers *et. al.* has overlaps with the data from Lundin *et. al.* and Hornidge *et. al.* and is consistent with both previous measurements.

Chapter 2

The π^- photoproduction/Compton scattering on ^{2}H experiment

This chapter provides an overview of the setup that was used for the π^- photoproduction/Compton scattering experiment. The experiment was performed at the Tagged-Photon Facility [89] of the MAX IV Laboratory [90] in Lund, Sweden. The experiment aimed to measure the π^- photoproduction cross-section $\sigma(E_\gamma)$ on the deuteron [91] as a function of the photon energy, E_γ,

$$\gamma + {}^2\mathrm{H} \rightarrow \pi^- + 2\mathrm{p} \tag{2.1}$$

and the differential Compton scattering cross-section $\sigma(E_\gamma, \cos\theta)$ on the deuteron [92] as a function of the photon energy and the angle of the scattered photon, θ,

$$\gamma + {}^2\mathrm{H} \rightarrow \gamma' + {}^2\mathrm{H}' \tag{2.2}$$

in the incident tagged photon energy interval from 140 to 160 MeV. The data were collected in three 4-week run periods in June 2011, September 2011 and April 2015. In this chapter a general overview is provided of how the experiment was performed and how the different reaction channels were studied. There are four sections in this chapter. Section 2.1 will briefly summarise all the general aspects relevant to the experimental apparatus. Section 2.2 addresses the configurations of the experimental hall that were necessary for some important aspects of the analysis. Section 2.3 provides a detailed account of how the π^- photoproduction events were identified. The last section of this chapter reviews the identification technique for the Compton scattering events.

2.1 Apparatus setup

2.1.1 Tagged photon production

The tagged photons that bombarded the target were created through the bremsstrahlung-tagging method [93, 94], which is an established technique in nuclear physics experiments. In this case an electron beam is incident on a thin radiator foil where the electrons de-accelerate and in the process radiate a photon in the forward direction. A dipole magnet installed after the radiator bends the degraded electron trajectories

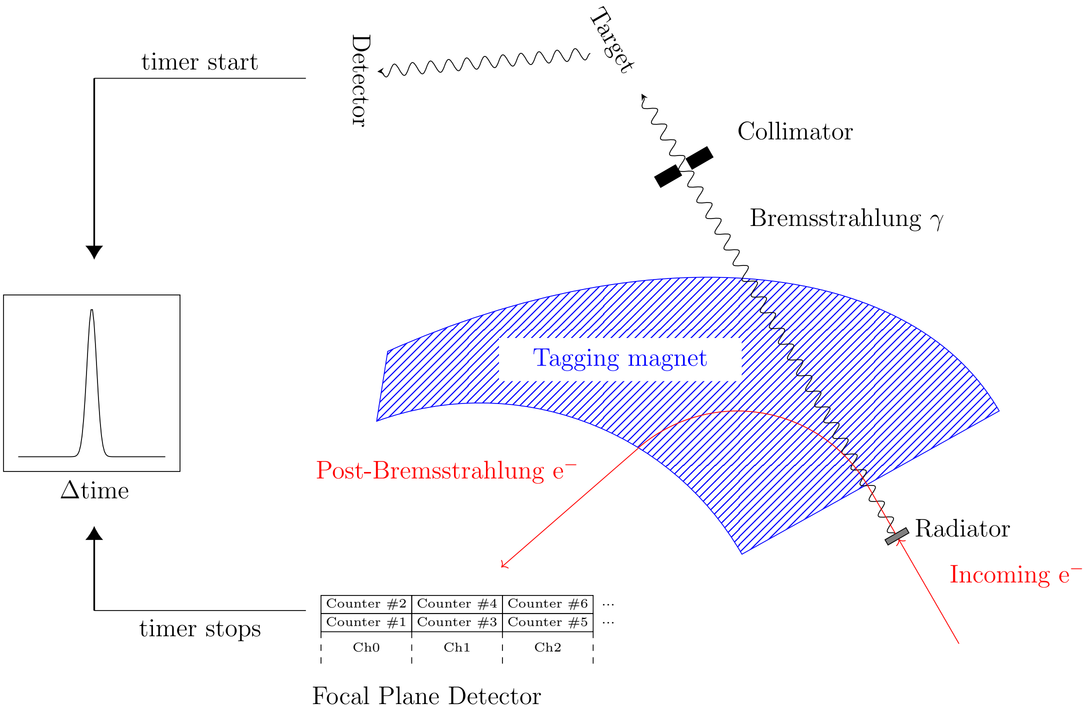

Figure 2.1: A schematic diagram of the photon tagging system in Lund, Sweden.

towards a position-sensitive detector installed along the plane where the electrons are brought to a focus after exit from the dipole. The focal plane detector is a highly segmented array of thin scintillators and allows determination of the position of the detected electron. Knowing the magnetic field strength and the position of the detected electron enables determination of the momentum of the electrons that have passed through the radiator. As the energy of the incident electron beam is known, the energies of the bremsstrahlung photons can be easily calculated from energy conservation. In this experiment the typical electron rate per focal plane channel during production running was $\sim 0.1 - 1$ MHz. A crucial component of the bremsstrahlung-tagging technique is the timing coincidence between the detector that registers the tagged photon in the experimental hall and the focal plane electron hit. The photon that has been emitted by an electron that creates a hit in the focal plane detector arrives at a certain time at the target relative to the electron hit in the focal plane. As the hit rates in the focal plane detector channels during production running are high, the only way of establishing which tagger channel is associated with the photon in the experimental hall is through the timing coincidence.

Figure 2.1 illustrates the tagged photon production system in Lund. A 300 µm thick Aluminium radiator was used, the electron beam incident on the radiator had a typical diameter of $\sim 0.5 - 1$ mm [95] and an energy of ~ 190 MeV. The experiment used the Lund End-Point tagger [96] with the SAL Focal Plane (FP) detector [97]. The SAL detector consisted of two segmented layers of thin plastic scintillators. A focal plane detector channel was defined as a complete overlap of a scintillator segment from the upper layer with a scintillator segment from the lower layer[1]. The upper and lower layer refer to the two layers of FP detector counters in Figure 2.1. The FP detector consisted of 64 scintillators (counters), which through the overlaps combined to a total of 31 FP channels[2]. A channel hit was registered when both the upper and the lower layer scintillator fired. Such a setup served to suppress the noise of the photomultiplier tubes that read out single counters as well as neutral particle background. In this experiment the tagger magnet and the FP detector were set up such that the photons were tagged in the energy range between 140 and 160 MeV. Only the bremsstrahlung photons that passed through a 19 mm diameter collimator entered the experimental hall. The distance between the radiator and the collimator was 3715 mm and the distance from the radiator to the target in the experimental hall was 7435 mm [95] (see also Figure A.2 in Appendix A.2).

2.1.2 Liquid deuterium target

The bremsstrahlung photons that passed through the collimator were incident on a liquid deuterium target. The liquid deuterium target that was used in this experiment was the same as was used for the experiment reported in Ref. [71, 88]. The cell which held the liquid deuterium had a cylindrical central body of 150 mm length and 68 mm diameter. There were spherical end caps attached to the cylindrical central body, such that at the centre the full length of the target was 170 mm (see Figure 2.2). The cell was made out of 120 µm thick Kapton. The liquid deuterium target was housed in a vacuum chamber constructed from stainless steel that was 1 mm thick in the scattering plane. The housing chamber had 100 µm thick Hostaphan entrance and exit windows for the photon beam. The target cell, the entrance and exit windows and the housing chamber in the scattering plane are depicted in Figure 2.3. The relative temperature and the absolute pressure of the liquid deuterium were continuously monitored throughout the experiment to be able to account for any density fluctuations in the target.

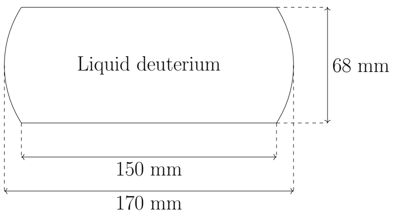

Figure 2.2: The dimensions of the Kapton cell.

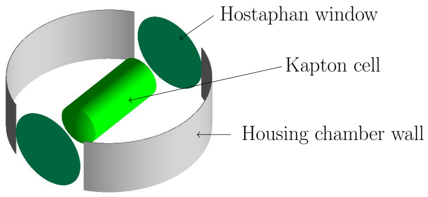

Figure 2.3: A figure depicting the target cell, the entrance and exit windows for the photon beam and the housing chamber (Geant4 simulation).

---

[1] Alternatively, the SAL detector could operate in a mode where the upper layer was shifted by half the width of one segment with respect to the lower layer.

[2] Channel 32 (defined by counters 63 and 64) was not used for registering tagged photons.

2.1.3 Photon detectors

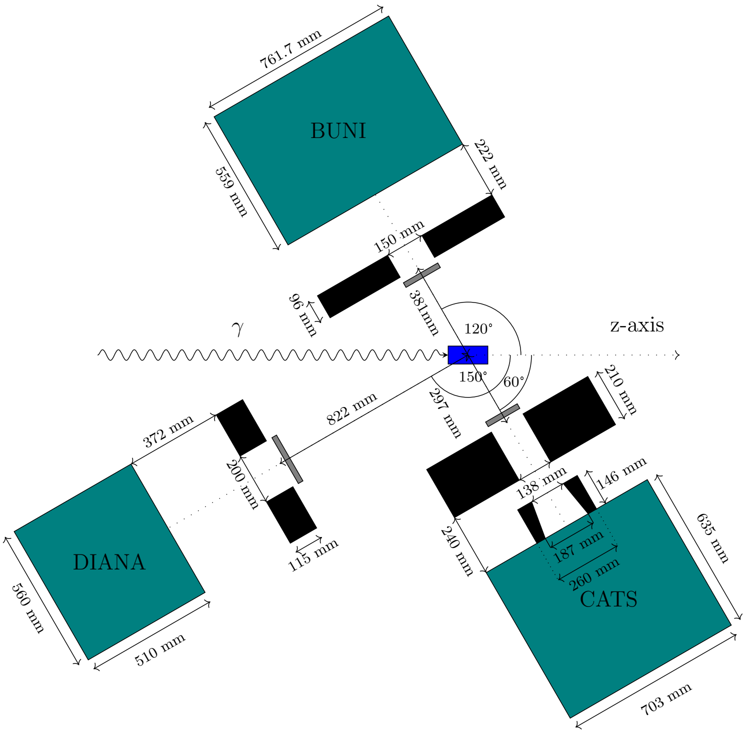

Figure 2.4: A drawing of the experimental setup in Lund, Sweden during the April 2015 data collection. The detector positioning in the June/September 2011 run period is summarised in Table 2.1.

Three large Thallium-doped Sodium Iodide (NaI(TI)) detectors were set up to detect photons originating from the target volume at laboratory angles $\theta = 60^\circ$, $\theta = 120^\circ$ and $\theta = 150^\circ$. The large NaI(TI) detectors are named Boston University Sodium Iodide (BUNI) [98], Compton And Two Photon Spectrometer (CATS) [99] and Detector Of Iodine And Sodium (DIANA) [88]. The layout of the photon detectors and the liquid deuterium target in the Lund experimental hall in April 2015 is shown in Figure 2.4. In the drawing the overall dimensions of the detectors, the front shielding and the collimators are indicated. Unlike BUNI and DIANA, CATS has an additional inner collimator to further constrain the solid angle acceptance. All three NaI(TI) detectors are fully encased in lead to suppress any radiation that does not enter the scintillator through the front collimator. In addition, the collimators have a ∼0.5 cm thick plastic scintillator paddle in front to veto charged particles. The distances from the target

Detector positions in different data collection periods

Run period	BUNI	CATS	DIANA
Jun./Sep. 2011	407 mm	335 mm	902 mm
April 2015	381 mm	297 mm	822 mm

Table 2.1: Detector distances (front shield to target centre) during different run periods. Also consult Figure 2.4.

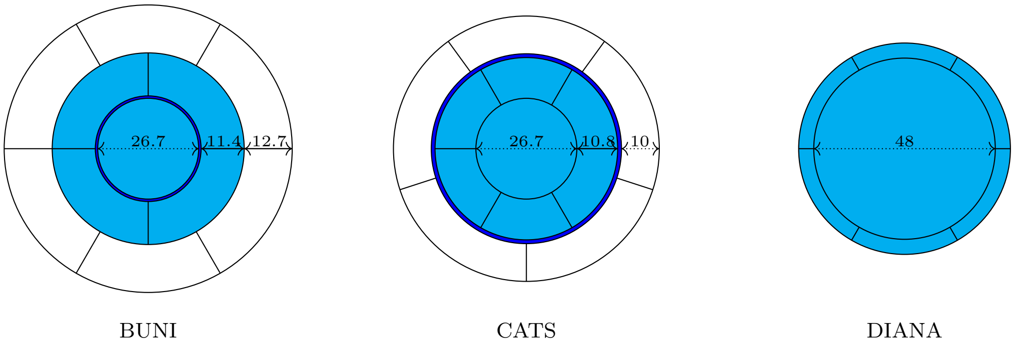

BUNI CATS DIANA

Figure 2.5: Cross-section views of BUNI, CATS and DIANA spectrometers, dimensions in cm. The cyan colour indicates the NaI(TI) crystals, the white colour depicts the plastic scintillators. For BUNI the dark blue ring depicts a 0.635 cm thick aluminium cylinder surrounding the core crystal, for CATS the blue ring depicts a 1 cm thick $LiCO_3$ cylinder surrounding the annulus. The DIANA annulus thickness is 4 cm.

centre to the front faces of the shielding during the April 2015 run period are shown. In the run periods in June and September 2011 the positioning of the detectors in the experimental hall was slightly different. The positioning in different run periods in summarised in Table 2.1.

The three NaI(TI) detectors have a similar design. The cross-sectional views of the detectors are depicted in Figure 2.5. The photons are detected through collecting the scintillation light that is emitted by the crystal when a charged particle causes ionisation in the NaI(TI). The scintillation light is read out by photomultiplier tubes attached to the rear faces of the crystals. All three detectors have an optically isolated core NaI(TI) crystal that is surrounded with an annulus of NaI(TI) pieces, making a full cylinder around the core. BUNI and CATS have, in addition, plastic scintillators outside of the NaI(TI) pieces.

As shown in Figure 2.5, in addition to the scintillators BUNI also has a thin layer of aluminium between the core and the quadrants, which holds the optically reflective powder in place. CATS includes a thin layer of $LiCO_3$ that serves the purpose of absorbing thermalised neutrons. The purpose of the NaI(TI) quadrants in BUNI and the sextants in CATS is to increase the total diameter of the scintillating material and capture electromagnetic shower leakage from the core crystal. The plastic scintillators are used in filtering out cosmic events. As is evident from Figure 2.5, DIANA does not have plastic scintillators. However, the diameter of the DIANA core crystal is substantially larger that that of CATS and BUNI and in the photon energy range typical in this experiment no substantial electromagnetic shower leakage to the annular segments was observed. Therefore the NaI(TI) annulus surrounding the DIANA core crystal was used for vetoing cosmic events and an additional layer of plastics was unnecessary. It should be noted that DIANA has in total twelve NaI(TI) annular pieces. Each piece is half the length of the central core crystal, such that there are six pieces surrounding the front half of the core and six surrounding the rear half of the core.

Readout of the NaI detectors

Detector	Core PMTs	NaI annulus PMTs	Plastic annulus PMTs
BUNI	7	3 per segment	2 per segment
CATS	7	4 per segment	3 per segment
DIANA	19	3 per segment	-

Table 2.2: Table summarising the readout of the detectors by PMTs.

2.1.4 Data Acquisition

A Data Acquisition (DAQ) system was employed to read out the signals from the detectors and store the information to disk. The most relevant signals and parts of the DAQ are briefly overviewed in the paragraphs below.

NaI detectors

The scintillation light from the NaI(TI) detectors was read out by Photomultiplier Tubes (PMTs) that were attached to the rear faces of the crystals. Table 2.2 provides the number of PMTs per detector that read out the core crystal, the annular NaI(TI) segments and the plastic segments. The analog signal from each core PMT was converted to digital format with a Charge-to-Digital Converter (QDC). The analog PMT signals from one segment were summed together before digitisation so that each segment could be read out by a single QDC.

Additionally, each of the three NaI(TI) detectors output a signal that could be used to trigger the DAQ. The trigger from BUNI was taken from the sum of the seven PMTs reading out the core crystal. The trigger signals from CATS and DIANA were taken from the PMT that was attached to the centre of the core crystal. The discriminators that were used to generate triggers from the detector signals are discussed further in Section 3.7, as they are related to time-walk effects.

FP detector

A PMT was attached to every counter (64 in total) of the FP detector. A hardware level AND between two PMT signals from the overlapping counters constituted an analog signal of a focal plane channel. If the signal of a FP channel was above threshold, the arrival time of the signal relative to a reference time was converted to digital format by a multihit Time-to-Digital Converter (TDC). The reference time was the trigger time of the DAQ. Additionally focal plane scalers counted the total number of hits per FP channel while data acquisition was running.

Data collection

Data was collected in 1-2 hour long runs, data from each run was stored into a separate file. The data collection was started and stopped by starting and stopping the DAQ system through a designated DAQ computer. During data collection for the π^- photoproduction and Compton scattering measurements (*production running*) the DAQ was triggered when a trigger signal was received from any of the three NaI(TI) detectors.

A different trigger setting was used for the in-beam measurements and is discussed in Section 2.2.1. As a result of the trigger the analog signals were read out by the QDCs/TDCs and stored to disk.

It is worth noting the difference between writing out the QDC/TDC signals (generally referred to as Analog-to-Digital Converter (ADC) signals) and the focal plane scalers. The ADCs read out and digitised the analog signals only when the DAQ received a trigger. For example, during an hour long production run the DAQ received approximately 10^6 triggers and therefore 10^6 events with the signals from the ADCs were written to disk. The scalers on the other hand were accumulated continuously while data acquisition was running, irrespective of the trigger count. Due to this the FP scalers could be used to determine the total number of Bremsstrahlung photons created in the tagged energy range during each production run.

2.2 Non-production measurements

Figure 2.4 depicts the floor plan of the experimental hall during production running in April 2015 for the π^- photoproduction and Compton scattering experiments. In addition to the displayed setup other configurations were used for various tasks necessary for the analysis procedure. These apparatus arrangements will be discussed briefly in the subsections below.

2.2.1 In-beam calibration

In the in-beam measurements each of the three NaI(TI) detectors was in turn moved directly into a very low intensity tagged photon beam to measure the response of the photon detector. The purpose of the in-beam measurements was to energy-calibrate the NaI(TI) spectrometers. At very low intensity the tagged photon that created the electromagnetic shower in the photon spectrometer could be identified unambiguously, allowing an accurate energy calibration of the photon detector to be performed. During the in-beam measurements the DAQ was triggered only from the detector in the path of the photon beam. This had an effect on the calibrations of the detectors; the implications are discussed in Section 3.9.

2.2.2 Tagging efficiency

Not all of the bremsstrahlung photons entered the experimental hall as many of them did not pass through the collimator shown in Figure 2.1. The ratio of tagged photons passing through the collimator to the total number of tagged photons is referred to as *tagging efficiency.* For tagging efficiency measurements a mobile Lead-glass Cherenkov detector was raised into the path of the photon beam that passed into the experimental hall. The dimensions of the Lead-glass detector were such that it contained the electromagnetic shower produced by the photons. The Lead-glass detector had a photon detection efficiency of $\sim 100\%$ and thus when placed into the beam line it could be used to count the number of photons entering the experimental hall. Daily measurements of the ratio of the bremsstrahlung photons entering the experimental hall to the electrons hitting the focal plane (equivalent to the number of produced bremsstrahlung photons) were taken. This ratio constitutes the tagging efficiency. Accurate knowledge of the tagging efficiency is of essential importance to correctly calculate the integrated tagged photon flux on the liquid deuterium target. Without knowing the integrated flux, the cross-sections cannot be determined.

2.2.3 Kapton target

To assess the effect of the 120 µm thick Kapton cell that holds the liquid deuterium, a dedicated Kapton target measurement was performed. In this case the liquid deuterium target was replaced with a dummy Kapton target that had been designed specifically for such measurements. The dummy Kapton target consisted of two hundred 80 µm thick Kapton sheets, so instead of a prolonged measurement with the actual empty cell, the background from the Kapton container could be assessed relatively quickly.

2.2.4 Cosmic background

Cosmic background was present throughout the run periods and constituted a background source that had to be eliminated. During the run periods there were occasions when the electron beam was not available for the experiment. When this occurred purely cosmic data was collected, meaning the DAQ was triggered only by the cosmic rays in the photon detectors. This data was used to establish the signature of the cosmic background events and to test the efficiency of various cosmic filters that were necessary for the data reduction process.

2.3 π^- signal identification

The idea of this experiment is to measure the π^- photoproduction cross-section on the deuteron by using the signature γ-ray spectrum of the events when the produced π^- is subsequently captured on the deuteron. To clarify how this can be achieved, the following subsection will list all the processes that can occur after the primary π^- photoproduction event

$$\gamma + {}^2\mathrm{H} \rightarrow \pi^- + 2\mathrm{p}. \tag{2.3}$$

Section 2.3.2 will then specifically address the event counting through the radiative capture reaction. Section 2.3.3 provides a brief account of the background sources.

2.3.1 Possible π^- processes

Capture on the deuteron

For negative pions with low kinetic energy (as in the Lund experiment) the most probable process is to stop inside the liquid deuterium volume and be captured on the deuteron. The capture can go through five channels:

$$\pi^- + {}^2\mathrm{H} \rightarrow 2\mathrm{n}, \tag{2.4}$$

$$\pi^- + {}^2\mathrm{H} \rightarrow \gamma + 2\mathrm{n}, \tag{2.5}$$

$$\pi^- + {}^2\mathrm{H} \rightarrow \mathrm{e}^+ + \mathrm{e}^- + 2\mathrm{n}, \tag{2.6}$$

$$\pi^- + {}^2\mathrm{H} \rightarrow \pi^0 + 2\mathrm{n}, \tag{2.7}$$

$$\pi^- + {}^2\mathrm{H} \rightarrow 2\gamma + 2\mathrm{n}. \tag{2.8}$$

Reactions (2.4) and (2.5) are the dominant channels through which the π^- capture on the deuteron occurs. The absolute branching ratios are summarised in Table 2.3. The low branching ratio values for (2.6) – (2.8) indicate that these channels occur very rarely compared to (2.4) and (2.5). The absolute branching ratio of the radiative capture reaction is 0.261 ± 0.004. This value is of great importance for the analysis presented in this thesis, as the radiative capture reaction is the channel through which the π^- photoproduction cross-section is measured. The overall capture probability is estimated from a Geant4 simulation (see Section 5.6). Combining the experimentally counted number of radiative captures with the overall capture probability from the simulation and the known branching ratio of $\mathrm{BR}_{\pi^- + {}^2\mathrm{H} \rightarrow \gamma\mathrm{nn}} = 0.261$ will allow determination of the number of photoproduced pions.

Absolute branching ratios of π^- capture on the deuteron

Channel	Branching ratio	Source
$\pi^- + {}^2\mathrm{H} \rightarrow 2\mathrm{n}$	0.739 ± 0.010	[100]
$\pi^- + {}^2\mathrm{H} \rightarrow \gamma + 2\mathrm{n}$	0.261 ± 0.004	[100]
$\pi^- + {}^2\mathrm{H} \rightarrow \mathrm{e}^+ + \mathrm{e}^- + 2\mathrm{n}$	$1.81 \cdot 10^{-3}$	[100, 101]
$\pi^- + {}^2\mathrm{H} \rightarrow \pi^0 + 2\mathrm{n}$	$1.45 \pm 0.19 \times 10^{-4}$	[102]
$\pi^- + {}^2\mathrm{H} \rightarrow 2\gamma + 2\mathrm{n}$	$1.42 \pm^{0.09}_{012}\ (\mathrm{stat}) \pm 0.11(\mathrm{sys}) \cdot 10^{-5}$	[103]

Table 2.3: Absolute branching ratios of the pion capture reactions on the deuteron [103].

Decay

The produced π^- could decay inside the liquid deuterium volume before the capture occurs. When this happens, it results in a muon and a neutrino 99.98% of the time [72],

$$\pi^- \rightarrow \mu^- \nu_\mu. \tag{2.9}$$

The muon background is investigated with a Geant4 simulation in Section 4.3.3.

Exit from target volume

In addition to the processes listed above, the π^- of reaction (2.3) could exit the liquid deuterium volume. Pion capture outside the liquid deuterium would occur mostly on iron (the housing chamber, see Section 2.1.2), carbon (Kapton and Hostaphan) or atmospheric elements. Table 1 of Ref. [104] and Table 4 of Ref. [105] reveal that on carbon, oxygen and calcium the probability for the capture reaction to be radiative is

$\lesssim 2\%$. Neither experimental data nor predictions exist for radiative capture probabilities on iron and nitrogen. It is assumed that nitrogen is similar to oxygen and iron is similar to calcium from the view point of pion capture. Thus on oxygen and iron the probability of the capture reaction to be radiative is also expected to be $\sim 2\%$. This estimation is combined with results from a Geant4 simulation in Section 4.3.4 to demonstrate that capture events outside the liquid deuterium do not constitute a substantial contamination to the measured signals.

Some pions that exit the target are expected to decay. As mentioned before, the potential decay backgrounds are addressed in Section 4.3.3.

Scattering

From the viewpoint of the event counting of this experiment, both the elastic and the inelastic scattering of the photoproduced pions

$$\pi^- + {}^2\mathrm{H} \rightarrow \pi^{-\prime} + {}^2\mathrm{H}', \tag{2.10}$$

$$\pi^- + {}^2\mathrm{H} \rightarrow \mathrm{n} + \mathrm{p} + \pi^{-\prime}. \tag{2.11}$$

do not require explicit consideration. After the scattering process, the pions of reactions (2.10), (2.11) will still be captured, decay or exit the target volume. The percentage of the negative pions that are captured will be determined from a Geant4 simulation.

2.3.2 Event counting through the radiative capture

As already mentioned at the beginning of this section, the gamma-ray of the single radiative capture channel (2.5) has a very distinct energy spectrum with a sharp peak just below 130 MeV. The maximum energy of the photon is defined by the reaction kinematics and limited to 131.458 MeV [106]. The three NaI(TI) detectors at three different angles as depicted in Figure 2.4 detected the photons emitted from the capture process. Numerous crucial pieces of information are necessary to infer the pion photoproduction cross-section from the yield of subsequent radiative captures (2.5). First of all, one needs to know how many of the produced pions stop in the target volume. Secondly, an estimate is needed for how many of the pions that stop in the target volume undergo capture and how many decay instead. Thirdly one of course needs to know the detector acceptance and solid angle. All of the specified information is inferred from a simulation using the Geant4 software package [107]. Knowing this along with the branching ratio information provided allows determination of the π^- photoproduction cross-section from the radiative capture yield.

2.3.3 Backgrounds

An important part of the analysis is a thorough estimation of the backgrounds to the photons from the radiative capture reaction. The elastic and inelastic scattering signals are potential background channels, but the scattering cross-sections are about two orders of magnitude lower and thus do not add significantly to the uncertainty of the results. Additionally, the signal from the radiative capture can be potentially contaminated by neutral pion photoproduction channels (γD $\rightarrow \pi^0 +$ X), photodisintegration channel (γD $\rightarrow$ np) and the non-radiative capture channel (2.4). The various sources of background are addressed in Section 4.3.

2.4 Compton signal identification

The measurement of the differential cross-section for Compton scattering

$$\gamma + {}^2\mathrm{H} \rightarrow \gamma' + {}^2\mathrm{H}' \tag{2.12}$$

relies on the detection of the scattered photon in one of the photon spectrometers depicted in Figure 2.4. For the Compton scattering channel the event identification is considerably simpler. The Compton events are identified through demanding that the missing energy

$$\mathrm{E}_{\mathrm{miss}} = |\mathrm{E}_{\gamma} - \mathrm{E}_{\gamma'}| \tag{2.13}$$

is less than 2.224 MeV, the binding energy of the deuteron. Although the idea behind this experiment is fairly simple, the actual extraction of the Compton signal is challenging due to its low differential cross-section. A successful analysis relies on a high quality detector calibration and on a very effective background separation.

Using Eq. (1.15), the Compton scattered photons are approximately in the following energy intervals in the three photon detectors:

- CATS at 60°: 135 to 153 MeV,
- BUNI at 120°: 125 to 142 MeV,
- DIANA at 150°: 123 to 138 MeV.

As mentioned in Section 2.3, the gamma-ray from the π^- capture on the deuteron has a characteristic spectrum that peaks just below 130 MeV and has an endpoint energy of 131.458 MeV. The π^- photoproduction cross-section is approximately two orders of magnitude higher than the Compton scattering cross-section. Thus, the Compton signal cannot be extracted at lower photon energies in BUNI and DIANA because of the contamination from π^- capture.

Apart from the π^- contamination, the only other background channels are the inelastic scattering

$$\gamma + {}^2\mathrm{H} \rightarrow \gamma' + \mathrm{p} + \mathrm{n} \tag{2.14}$$

and the scattering from the Kapton vessel. The high resolution of the photon detectors (discussed in Chapter 3) enables the inelastic channel to be separated with tight cuts on the missing energy. To account for the Kapton background the measurement with the dummy target (see Section 2.2.3) can be employed. Similarly to the π^- channel, the solid angle acceptance of the detectors is required and calculated (Section 6.3) using the Geant4 simulation.

Chapter 3

Detector calibrations

This chapter details all the analysis steps related to the calibration of the apparatus. The in-beam calibration runs discussed in Section 2.2.1 played a crucial role in calibrating the detectors. Sections 3.1 to 3.4 outline the calibration steps based only on the in-beam data. Sections 3.5 and 3.6 discuss how the stability of the calibration was monitored and corrected for throughout the data collection periods. Section 3.7 outlines the correction methods to eliminate time-walk and Section 3.8 details the filtering techniques for cosmic and charged events. The final Section 3.9 identifies two effects that caused the overall calibration results to be shifted and details how the shifts in the calibrations were corrected. Most of the calibration techniques of this chapter had been established before and are to some extent discussed in Refs. [88, 87, 108].

3.1 Focal plane timing alignment

As explained in Section 2.1.1, the tagged events were identified through a timing coincidence between a signal in one of the detectors in the experimental hall and an electron hit in one of the focal plane detector channels. From the experimental point of view the coincidence was established through measuring the time difference between a detector signal (trigger time, see Section 2.1.4) and an electron hit signal,

$$\mathrm{Coincidence}_{\mathrm{FPCh}} = \mathrm{Time}_{\mathrm{trigger}} - \mathrm{Time}_{\mathrm{FPCh\,hit}}. \tag{3.1}$$

Ideally the coincidence time would have been identical for all of the channels of the FP detector, but due to small differences in signal transit time this was not the case. The first step of the calibration procedure was to align the timing coincidence signals from all of the FP detector channels.

The in-beam calibration measurements used a very low intensity electron beam. Due to this the count rate in the FP detector was low and it was possible to unambiguously determine the electron in the FP detector that was associated with the trigger from the detector in the beam path. A histogram with the coincidence time was filled for each FP detector channel. This allowed the coincidence peak to be found for every FP channel. Using the extracted peak locations, an offset was calculated for every channel that shifted the coincidence peak to 300 ns. The absolute position of the coincidence peak was arbitrary, but it was important that all channels peaked at the same location. The timing signals from the FP channels had to be grouped together

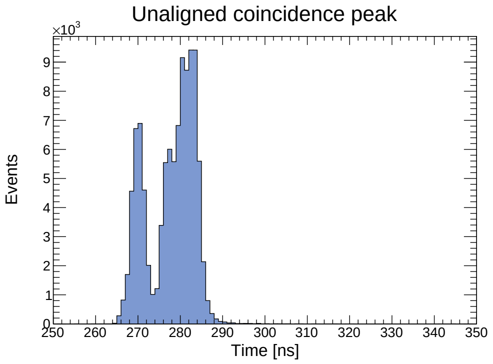

Figure 3.1: Histogram showing the timing coincidence peak over all FP channels without alignment.

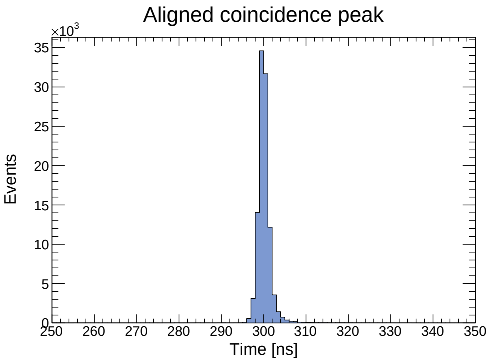

Figure 3.2: Histogram showing the timing coincidence peak over all FP channels after the alignment procedure.

in the signal extraction procedure (Chapter 5, 6), which could be done meaningfully only when the timing signals were aligned.

Once the offsets had been determined the coincidence time was calculated as

$$\text{Coincidence}_{\text{FPCh}} = \text{Time}_{\text{trigger}} - \text{Time}_{\text{FPCh hit}} + \text{Offset}_{\text{FPCh}}. \tag{3.2}$$

Figures 3.1 and 3.2 depict the timing coincidence peak over all of the FP channels before and after the alignment procedure (CATS in-beam measurement). The latter figure demonstrates clearly that after the timing alignment calibration all of the tagged events were in one narrow timing coincidence peak centred at 300 ns.

3.2 Photomultiplier pedestal subtraction

The energies of the photons entering the NaI(TI) detectors were determined through collecting the created scintillation light with photomultiplier tubes that were attached to the rear faces of the crystals and digitising the integrated charge from the anodes of the photomultipliers. Figure 3.3 depicts the uncalibrated spectrum of the in-beam events from one of the photomultipliers reading out the BUNI detector. On the x-axis of the histogram is the integrated charge from an ADC expressed in ADC channels. There are three distinct components to the spectrum. First, the sharp peak on the very left is the PMT pedestal. This corresponds to a value from the ADC when there was actually no scintillation seen by the PMT. Second, in the ADC channel region from $\sim 900-1300$ there is a wider band that was caused by the tagged photons entering the NaI(TI) detector. Note that in the depicted histogram photons from the full tagger range contributed, which is why the peak is relatively broad. Finally, on the right there is an overflow peak. The overflow peak contains the events in which the PMT signal was outside the dynamical range of the ADC.

Due to small variations in the electronics associated with signal read-out from the PMTs, the pedestals of different PMTs peaked at different locations. For a meaningful signal extraction the pedestals of different PMTs had to be aligned to 0. This was achieved by subtracting the ADC channel corresponding to the pedestal peak location from the ADC signal. Figure 3.4 displays the same data as Figure 3.3 after the pedestal subtraction.

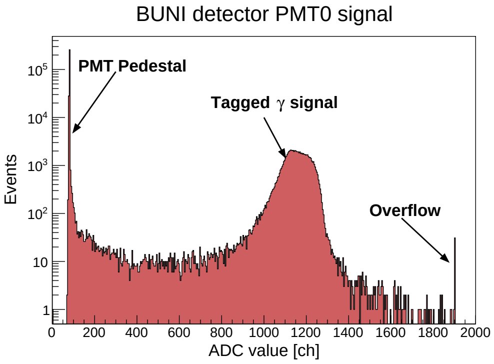

Figure 3.3: Histogram of BUNI in-beam events in one PMT before pedestal subtraction.

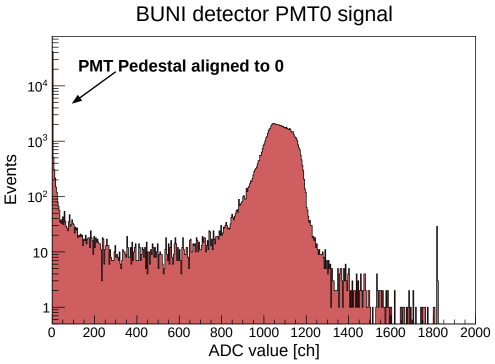

Figure 3.4: Histogram of BUNI in-beam events in one PMT after pedestal calibration.

It should be clarified here that generally the in-beam data were collected with a different trigger setting than that used for the data in Figures 3.3 and 3.4. The in-beam events triggered only from the detector which lay in the photon beam path. Due to this the pedestals were not visible in the in-beam data. The pedestals for the calibration runs were determined from data files taken immediately before or after the in-beam data. This is an important point for the energy calibration corrections discussed in Section 3.9. The data in Figures 3.3 and 3.4 are from a short test run which triggered from the FP detector, causing the pedestal to be clearly visible.

3.3 Matching photomultiplier gains

After the pedestal calibrations the PMTs had to be gain matched. The purpose of the gain matching procedure was to align all of the core PMT signals of a detector, such that the signals peaked at the same ADC channel value at a given incident photon energy. In principle this could have been achieved at the hardware level by adjusting the voltages applied to the PMTs, but in practice the fine tuning had to be performed at the software level.

Figure 3.5 illustrates the gain matching procedure. In this example spectra from three of the seven PMTs that read out the core crystal of the BUNI detector are displayed. The PMT spectra are associated with a hit in the focal plane channel 15, which corresponds to a tagged photon energy of $E_\gamma = 150.7$ MeV. The left hand histograms of Figure 3.5 depict the spectra of pedestal subtracted signals in the three PMTs before any software level gain matching was performed. The right hand histograms display the same spectra after gain matching. After the gain matching procedure the PMTs peaked at the same location, which was the desired result.

From the technical point of view the gain matching was performed as follows. For simplicity let only two PMTs be considered, PMT_0 and PMT_1. First of all, for each PMT a histogram associated with the focal plane channel 0, 5, 10, ... 30 was filled, in total 7 histograms per PMT. Then all the histograms were fitted with a reverse Landau shape (the solid black curve in the histograms in Figure 3.5) to extract the peak location. It was chosen to match the gains against PMT_0, as it was attached to the centre of the crystal and saw the most scintillation light. The extracted peak

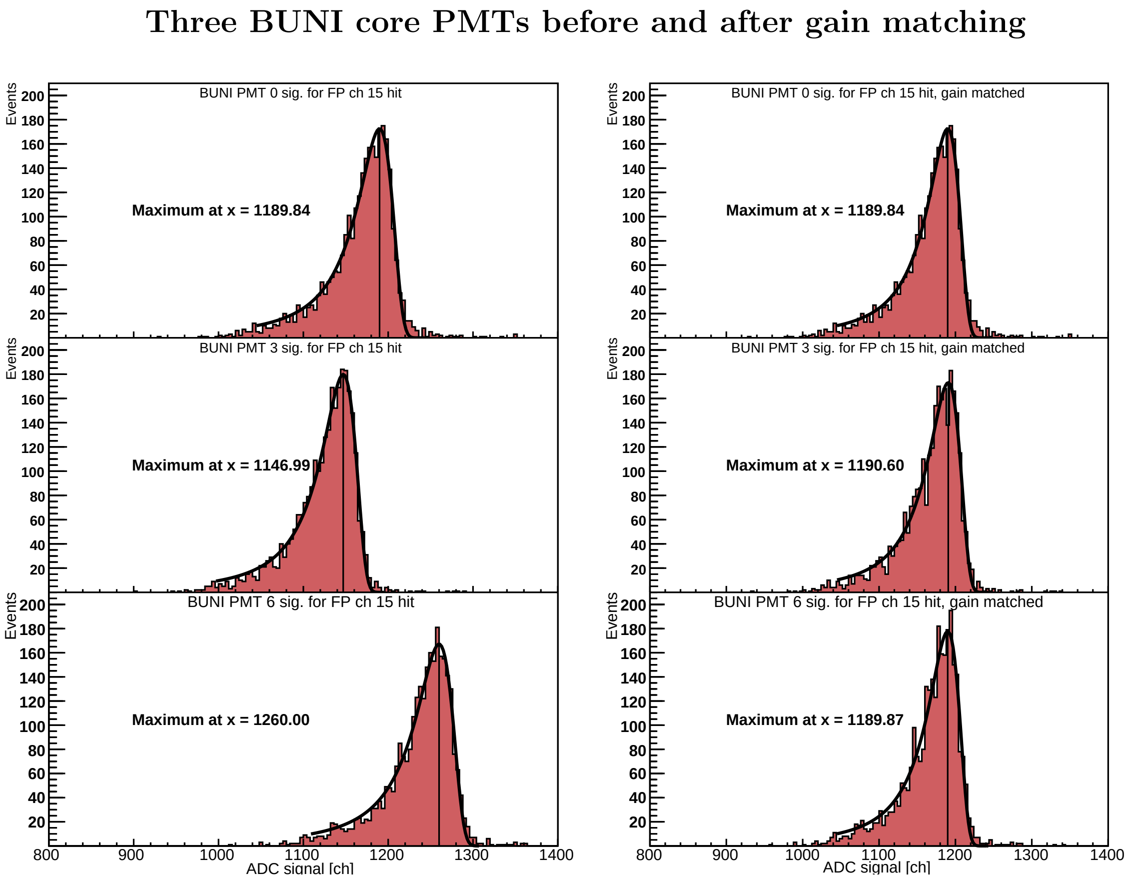

Figure 3.5: The left hand histograms display the signal spectra from three PMTs of the BUNI detector for $E_\gamma = 150.7$ MeV (FP channel 15) before gain matching. The right hand histograms depict the same signal spectra after gain matching. The fits and the extracted maxima are also shown.

locations were used to find the coefficients that moved the PMT_1 signal peak for a given FP channel to the same location as the PMT_0 signal peak. For PMT_1 in total seven coefficients were calculated as

$$\mathrm{C}_{\mathrm{PMT1\_FPCh0}} = \frac{\text{Peak PMT0}_{\mathrm{FPCh0}}}{\text{Peak PMT1}_{\mathrm{FPCh0}}},\ \mathrm{C}_{\mathrm{PMT1\_FPCh5}} = \frac{\text{Peak PMT0}_{\mathrm{FPCh5}}}{\text{Peak PMT1}_{\mathrm{FPCh5}}},\ \ldots\ . \tag{3.3}$$

The seven coefficients sampled the gain difference between the two PMTs in the full energy range of the Focal Plane detector. In principle a coefficient for each FP channel could have been calculated (31 in total), but in practice the gain difference did not reveal any dependence on the incident photon energy and a sample of seven channels was found to be sufficient. The standard deviation of the seven coefficients was typically less than 0.5% of the mean. This allowed the final gain matching coefficient $\mathrm{C}_{\mathrm{PMT1}}$ to be calculated as the average of the seven coefficients. The calibrated signal for PMT_1 could then be expressed as

$$\text{Calibrated Signal}_{\mathrm{PMT1}} = (\text{Signal}_{\mathrm{PMT1}} - \text{Pedestal}_{\mathrm{PMT1}}) \cdot \mathrm{C}_{\mathrm{PMT1}}. \tag{3.4}$$

The same procedure was repeated for the other six PMTs attached to the BUNI core crystal. The PMTs reading out the core crystals of the CATS and DIANA detectors were gain matched in identical fashion.

After the pedestal subtraction and the gain matching procedures all of the PMTs attached to the core crystal of a detector gave ADC channel value 0 when there was no signal in the detector and peaked at the same ADC channel value for a given photon energy. Due to this behaviour the average of the PMT outputs could be used as a meaningful detector response and the first energy calibration of the detectors could be performed. The energy calibration was simply the linear relation between the incident photon energy and the average of the PMT signals. The linear fit for the BUNI detector is depicted in Figure 3.6. Using the slope and intercept of the fit line allowed determination of the energy of the detected photon from the average of the pedestal subtracted and gain matched PMT signals as

$$E_{\text{core}} = \left[\sum_{\text{i}}^{\text{N}} \frac{(S_{\text{i}} - P_{\text{i}}) \cdot C_{\text{i}}}{N} \right] \cdot a_{\text{core cal}} + b_{\text{core cal}}. \tag{3.5}$$

In Eq. (3.5) S, P and C denote the signal, pedestal and gain matching coefficient of a core PMT. $a_{\text{core cal}}$ and $b_{\text{core cal}}$ are the slope and intercept of the core energy calibration from Figure 3.6 and N is the number of PMTs reading out the core crystal. The quality of the energy calibration and the detector resolution was assessed by inspecting the difference between the tagged photon energies and the detected energies. The energy balance is depicted in Figure 3.7. Ideally the energy balance would be zero, but in reality the spectrum has a width around 0 due to the resolution of the detector and a tail to the left due to electromagnetic shower leakage from the core crystal.

The calibration as illustrated in Figure 3.7 only used the core crystal of the detector. In BUNI and CATS detectors some of the electromagnetic shower leaked into the annular segments. The steps to incorporate the signals from the annular segments into the energy calibration are discussed in the next section. The core crystal of the DIANA detector was significantly larger (see Figure 2.5) and the procedures of this section resulted in a Full Width at Half Maximum (FWHM) less than 3 MeV, which was the expected 2% resolution of the detector. Thus the procedures as detailed here finalised the energy calibration of the DIANA detector.

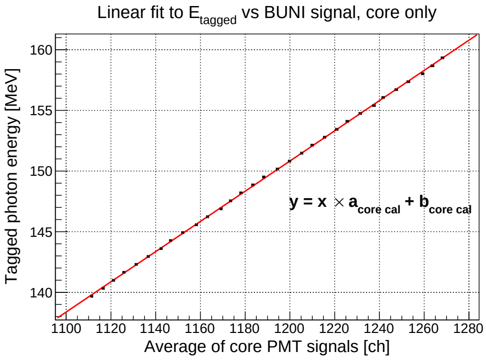

Figure 3.6: A graph depicting the energy calibration fit for the BUNI detector using only the central core crystal. The average of the calibrated core PMT signals is on the x-axis, the tagged photon energies are on the y-axis.

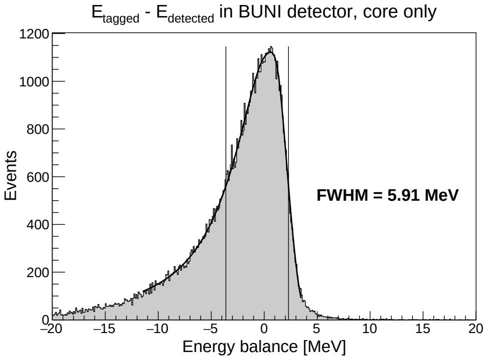

Figure 3.7: A histogram showing the difference between the tagged photon energies (full FP range) and the detected photon energies in the BUNI detector using only the core crystal. The FWHM is also indicated.

3.4 Incorporating signals from the annulus

Electromagnetic shower leakage to the annulus is best illustrated by a 2D histogram that has the pedestal subtracted ADC signal from one annular segment on the y-axis and the core energy balance on the x-axis. Such a histogram is depicted in Figure 3.8, using the core calibration of the CATS detector and annular segment 0. The tail in the energy balance spectrum towards decreasing values is accompanied by a signal in the annular segment, which indicates EM shower leakage to the annulus. The energy balance on the x-axis has been expressed in ADC channels rather than in MeV. The energy balance was calculated as

$$\Delta E_{\mathrm{core}} = \sum_{\mathrm{i}}^{\mathrm{N}} \frac{(S_{\mathrm{i}} - P_{\mathrm{i}}) \cdot C_{\mathrm{i}}}{N} + \frac{b_{\mathrm{core\,cal}}}{a_{\mathrm{core\,cal}}} - \frac{E_\gamma}{a_{\mathrm{core\,cal}}}. \tag{3.6}$$

In Eq. (3.6) ΔE_{core} is the core energy balance in ADC channels and E_γ denotes the tagged photon energy. Other notation is the same as in Eq. (3.5). Expressing ΔE_{core} in ADC channels was not a necessity, but allowed for a more convenient and consistent procedure for the calibration of the segments. Additionally due to a technical reason the value of the energy balance in ADC channels was offset by 1000[1] in Figures 3.8 and 3.9.

The purpose of the calibration procedure was to find a conversion factor that allowed the signal in the segment to be added to the calibrated core signal. The conversion factor is visualised by the slope of the black line in Figure 3.8. The line related the segment ADC value to the core energy balance value. To determine the black line, first the 2D histogram of Figure 3.8 was projected to 1D histograms at different segment ADC values. Second, the 1D histograms were fitted with a reversed Landau shape to extract the peak locations as exemplified in Figure 3.9. Third, a graph with ΔE_{core} on the x-axis and the corresponding peak locations on the y-axis was fitted linearly, resulting in the black fit line displayed in Figure 3.8.

To include the signal in the annular segments to the energy calibration of the detector, one can use a simple linear equation

$$\mathrm{Signal}_{\mathrm{seg0}} - \mathrm{Pedestal}_{\mathrm{seg0}} = \mathrm{k}_{\mathrm{seg0}} \cdot \mathit{\Delta} E_{\mathrm{core}} + \mathrm{const}, \tag{3.7}$$

where $\mathrm{Signal}_{\mathrm{seg0}} - \mathrm{Pedestal}_{\mathrm{seg0}}$ is the pedestal subtracted ADC value from segment 0, $\mathrm{k}_{\mathrm{seg0}}$ is the slope, ΔE_{core} is the core energy balance in ADC channels and const is the intercept. From Eq. (3.7)

$$\mathit{\Delta} E_{\mathrm{core}} = \frac{\mathrm{Signal}_{\mathrm{seg0}} - \mathrm{Pedestal}_{\mathrm{seg0}}}{\mathrm{k}_{\mathrm{seg0}}} - \frac{\mathrm{const}}{\mathrm{k}_{\mathrm{seg0}}}. \tag{3.8}$$

The second term on the right-hand side has no physical significance and can be neglected. This leaves a simple relation between the core energy balance and the segment ADC value. It is now assumed that the missing energy in the core energy balance was

---

[1] Without the offset the peak of the energy balance would be around 0. The change of sign around 0 on the x-axis complicated the procedure to find the black fit line in Figure 3.8.

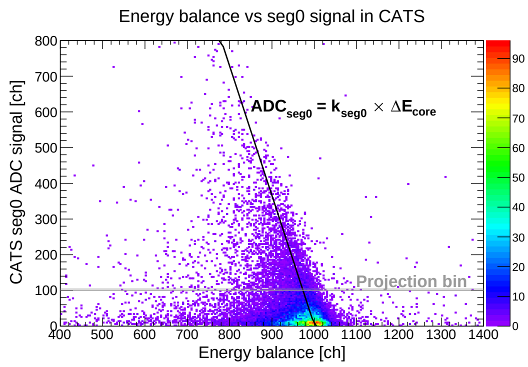

Figure 3.8: CATS core energy balance vs segment 0 ADC. The black line is a linear fit to the peak positions extracted from the reversed Landau fits to the projections along the x-axis (see Figure 3.9). The example projection bin is indicated with grey lines.

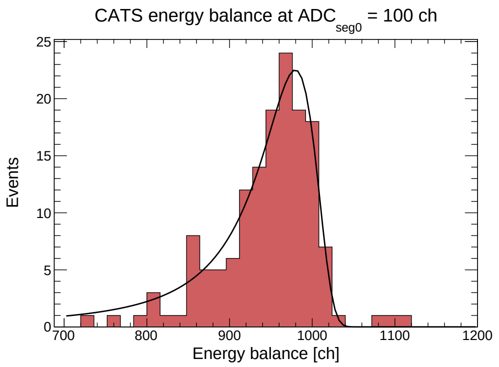

Figure 3.9: A projection along the x-axis of Figure 3.8. The grey lines in Figure 3.8 indicate the segment ADC value at which the projection was made. The black line in this figure shows the reversed Landau shape that was used to extract the peak position.

due to the electromagnetic shower leakage into the annulus. In this case one can make the Ansatz

$$\mathit{\Delta} E_{\mathrm{core}} = \frac{\mathrm{Signal}_{\mathrm{seg0}} - \mathrm{Pedestal}_{\mathrm{seg0}}}{\mathrm{k}_{\mathrm{seg0}}} \equiv -E_{\mathrm{seg0}} \tag{3.9}$$

to calculate the amount of energy E_{seg0} that leaked from the core crystal to the annular segment in question. The E_{seg0} in Eq. (3.9) is negated because the slope $\mathrm{k}_{\mathrm{seg0}}$ is negative (see Figure 3.7). Alternatively, the negative sign can be understood by realising that Eq. (3.9) relates the energy in segment 0 to the energy balance of the core, $\Delta E_{\mathrm{core}} = -E_{\mathrm{seg0}}$. Without the minus sign a negative energy balance would mean a negative energy deposit in the annular segment, which is not physical.

The quantity E_{seg0} is in the units of core PMT ADC channels and thus can be directly added to the average of the the core PMT signals. This is the reason why the energy balance in Figure 3.8 was expressed in ADC channels rather than in MeV. The procedure was repeated for each annular segment (4 for BUNI, 6 for CATS) to find the slopes of the black fit lines exemplified in Figure 3.8. The full detector response to the in-beam events was calculated as

$$\mathcal{R}_{\mathrm{cal}} = \sum_{\mathrm{i}}^{\mathrm{N}} \frac{(S_{\mathrm{i}} - P_{\mathrm{i}}) \cdot C_{\mathrm{i}}}{N} + \sum_{\mathrm{j}}^{M} \frac{(S'_{\mathrm{j}} - P'_{\mathrm{j}})}{-k_{\mathrm{j}}}. \tag{3.10}$$

In Eq. (3.10) the first sum on the right hand side is over the PMTs reading out the core crystal and the notation is explained after Eq. (3.5). The second sum on the right hand side is over the M annular segments in the detector. S' and P' are the signal and pedestal of the annular segment and k is the slope corresponding to the annular segment, determined through a fit illustrated in Figure 3.8. The presented calibration technique of the annular segments is valid if the annular signals are not correlated, meaning that in every event the shower leaks dominantly to only one of the annular pieces. No significant correlation between the signals was observed and thus the procedure is justified. The same calibration technique has been used previously in Ref. [88].

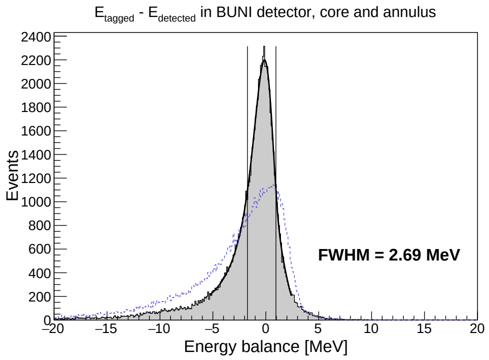

Figure 3.10: Energy balance in the BUNI detector after the signals from annular segments have been calibrated and added to the core signal. The blue dashed line depicts Figure 3.7 for comparison.

Including the signals from the annular segments in this fashion significantly improved the detector resolution. The calibration was performed through a fit similar to the one depicted in Figure 3.6, but in this case the x-axis had the full detector response as given by Eq. (3.10). Figure 3.10 depicts the energy balance in the BUNI detector over the in-beam events after the annular segments had been calibrated and added to the signal from the core crystal. The histogram from Figure 3.7 has been overlaid and is indicated with the blue dashed line. The FWHM has improved significantly from 5.91 MeV to 2.69 MeV. Taking into account that the average incident photon energy was approximately 150 MeV, a FWHM of 2.7 MeV translates to a resolution of $\sim 2\%$, which is the expected characteristic for the detectors under consideration. Similar resolution was obtained in the CATS detector. As mentioned earlier, in the DIANA detector the 2% resolution was achieved already after the steps described in Section 3.3 and no significant shower leakage to the annulus was observed.

3.5 Correction for photomultiplier pedestal drifts

For the BUNI and CATS detectors the pedestal calibration as performed in Section 3.2 was not enough, as the locations of the pedestal peaks drifted in time due to a small instability in the DAQ electronics. The drifts were corrected for by monitoring the pedestal peak locations continuously (every 10k events) through the run periods. Figure 3.11 depicts the pedestal peak of the central PMT of the BUNI detector over the full data set from September 2011. It can been seen that the pedestal shifted to higher ADC channels during the scattering runs as compared to the pedestal determined in the calibration. The pedestal tended to jump between certain values, which is indicated by the distinguishable peaks at ADC channels ~ 20, ~ 30 and ~ 45 in Figure 3.11. Figure 3.12 depicts the same data as Figure 3.11 with corrections for the pedestal drifts. The result is a narrow peak at ADC channel 0, which indicates that the correction was effective. The strongest pedestal fluctuations were observed in the BUNI detector. The effect was moderate in CATS and no pedestal drifts were observed in the DIANA detector. With the pedestal corrections the detector response during the production runs was calculated as

$$\mathcal{R}_{\mathrm{evt}} = \sum_{\mathrm{i}}^{\mathrm{N}} \frac{(S_{\mathrm{i}} - P_{\mathrm{i}} + \Delta P_{\mathrm{i}}) \cdot C_{\mathrm{i}}}{N} + \sum_{\mathrm{j}}^{M} \frac{\left(S'_{\mathrm{j}} - P'_{\mathrm{j}} + \Delta P'_{\mathrm{j}}\right)}{-k_{\mathrm{j}}}. \tag{3.11}$$

ΔP and $\Delta P'$ were the pedestal corrections for the core PMT and the signal from the annular segment for a given event. Other notation is explained after Eqs. (3.5) and (3.10).

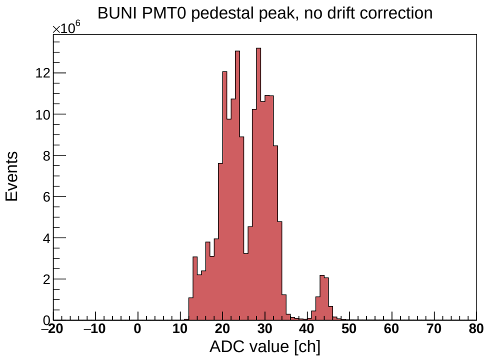

Figure 3.11: BUNI central PMT pedestal peak in September 2011 data set without correction for pedestal drift.

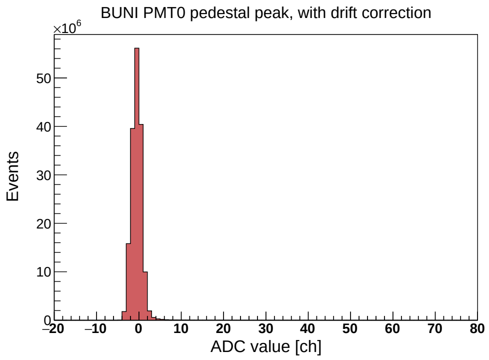

Figure 3.12: BUNI central PMT pedestal peak in September 2011 data set after correction for pedestal drift.

3.6 Correction for photomultiplier gain drifts

The gains of the photomultipliers reading out the NaI(TI) crystals were not constant, but drifted in time. In addition to the gain matching discussed in Section 3.3, the gain of each PMT had to be monitored and corrected to the value it had during the in-beam calibration run. This was done by monitoring the location of the peak in the pulse height spectrum produced by cosmic-ray muons traversing the NaI(TI) detector. The mean energy of the cosmic muons at sea level is ≈ 4 GeV [72], so that they are effectively minimum ionizing particles inside the NaI(TI). Thus the deposited energy did not depend on the muon energy, but only on the muon path length through the crystal. The annular segments of the detectors were used to select cosmic events where the muon tracks were approximately of the same length. This was achieved by only using the cosmic events where the two opposing annular pieces had a signal. The filtering process is illustrated in Figure 3.13.

An example spectrum of the selected cosmic events in the CATS detector from one data file (∼1h data collecting) is depicted in Figure 3.14. The histogram has been fitted to extract the peak location. A gain correction was calculated for each PMT for every

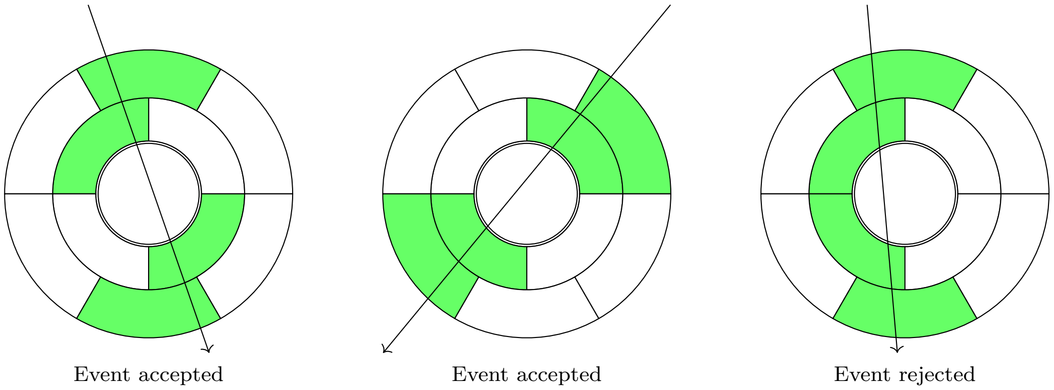

Figure 3.13: Illustration of the selection of cosmic events for monitoring photomultiplier gain drifts. The green colour highlights the annular parts with the signal for the given cosmic track. Only events with similar muon track lengths through the core crystal were selected.

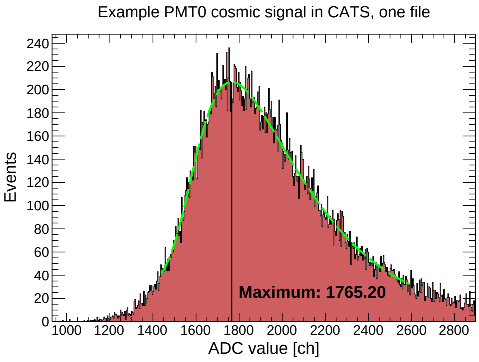

Figure 3.14: Spectrum of the selected cosmic events in the central PMT of the CATS detector for a single data run of ~1 hour. The spectrum has been fitted (green long-dashed line) to extract the location of the peak.

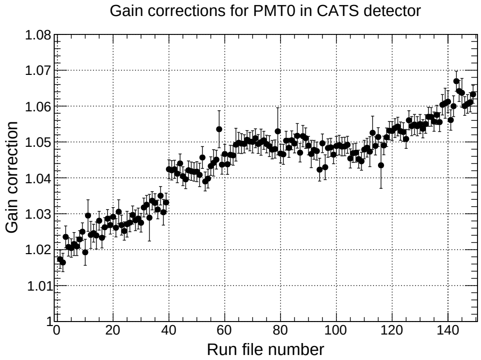

Figure 3.15: Gain corrections for the central PMT of the CATS detector over the September 2011 run period. In total 146 data files were collected, each 1-2 hours in duration.

data file by dividing the cosmic peak location in that file by the cosmic peak location for the in-beam calibration file. The gain corrections for the central PMT of the CATS detector over the full run period of September 2011 are depicted in Figure 3.15. With the gain corrections the detector response during the data collection runs was calculated as

$$\mathcal{R}_{\mathrm{evt}} = \sum_{\mathrm{i}}^{\mathrm{N}} \frac{(S_{\mathrm{i}} - P_{\mathrm{i}} + \Delta P_{\mathrm{i}}) \cdot C_{\mathrm{i}} \cdot \epsilon_{\mathrm{i}}}{N} + \sum_{\mathrm{j}}^{M} \frac{\left(S'_{\mathrm{j}} - P'_{\mathrm{j}} + \Delta P'_{\mathrm{j}}\right) \cdot \epsilon'_{\mathrm{j}}}{-k_{\mathrm{j}}}. \tag{3.12}$$

In Eq. (3.12) ϵ and ϵ' are the gain corrections for the core PMT and the annular segment signal for a given event. Other notation is explained after Eqs. (3.5), (3.10) and (3.11).

A considerable effort was made to find a stable automated fitting routine. The need for that is clear, if one considers that in the CATS detector there were 13 PMTs that had to be monitored for gain drifts, which gives $146 \times 13 = 1898$ fits for one detector in one run period alone. The best method was found to be to first fit the PMT histogram that had all the filtered cosmic events over the full run period. The line shape, which was successfully represented by a sum of a Gaussian and a Landau function, was fixed from that fit (a separate fixed line for each PMT). Filtered cosmic data from each file was then fitted separately using the fixed line shape (green long-dashed line in Figure 3.14), but allowing shifts along the x-axis and an overall scaling. The gain drifts had only a moderate effect on the shape of the cosmic spectra in individual run files and the fixed average shape was found to be a reasonable approximation. The error bars visible in Figure 3.15 are associated with the uncertainty in determining the x-shift. This method had the advantages of a reliable χ^2 value, a good numerical convergence and an easily comprehensible fit result (the shift in x).

3.7 Time-walk correction

The phenomenon where the timing of a signal is affected by its pulse height is referred to as *time-walk*. Time-walk occurs because a stronger signal passes the discriminator threshold earlier, resulting in an earlier signal in the discriminator output. Figure 3.16

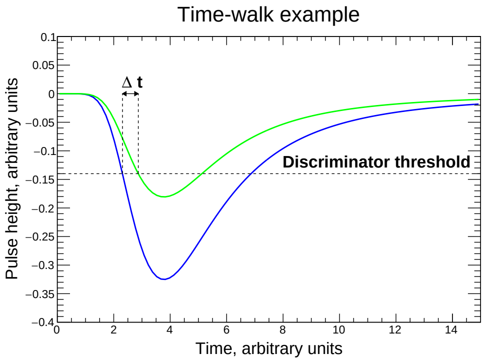

Figure 3.16: An illustration of time-walk. Stronger pulses reach the discriminator threshold earlier, resulting in a dependence between the pulse height and the discriminator output signal time.

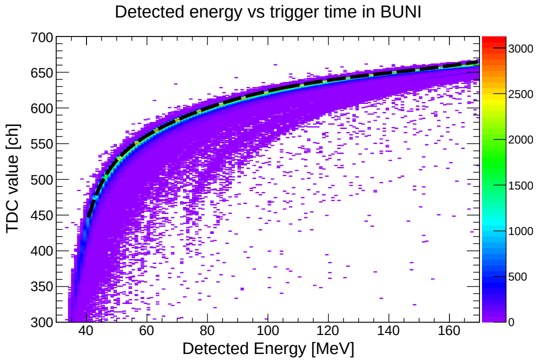

Figure 3.17: The dependence between the trigger time (in TDC channels) and detected energy in the BUNI detector. The fit to extract the relation is depicted with the black dashed line.

illustrates how different pulses reach the threshold at different times causing time-walk to occur. From the view point of this experiment, time-walk caused the trigger time from a detector to depend on the energy deposit inside the detector. Figure 3.17 depicts a 2D histogram of the BUNI in-beam data with the detected energy on the x-axis and the TDC signal from BUNI trigger on the y-axis. The relation between the trigger time and the detected energy is clearly visible from the histogram. The fit to extract the time-walk relation, using the function $f(x) = e^{c_1+c_2x} + c_3 + c_4x + c_5x^2 + c_6x^3$, has been depicted with a black dashed line.

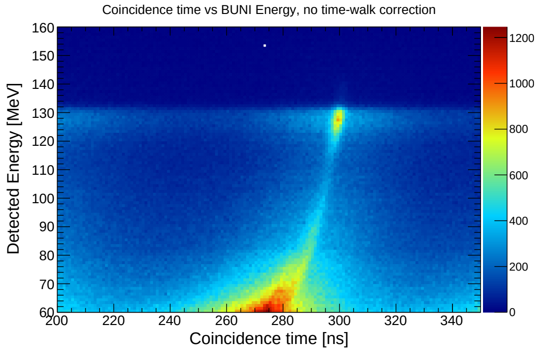

Figure 3.18: Coincidence time vs Detected Energy in the BUNI detector without time-walk corrections.

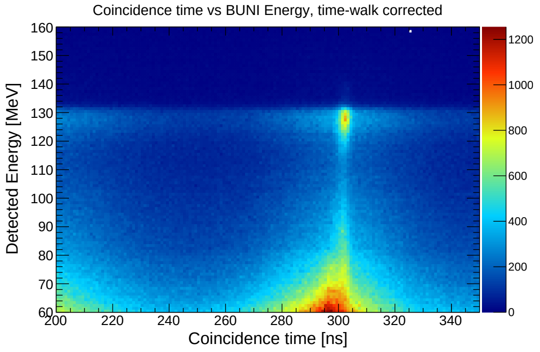

Figure 3.19: Coincidence time vs Detected Energy in the BUNI detector after time-walk corrections.

As the tagged events are identified through a timing coincidence between the Focal Plane detector and a trigger from a detector in the experimental hall, it was important to correct for time-walk. This was done by using the fit curve of Figure 3.17 to find a time-walk correction depending on the energy deposit inside the detector. The efficiency of the correction method is best visualised by 2D histograms with the coincidence time on the x-axis and the detected energy on the y-axis. The tagged events should arrive at the same time, i.e. a vertical band should be visible in the described 2D histogram. Figure 3.18 depicts the histogram without time-walk correction, Figure 3.19 displays the same data after the time-walk correction was applied.

The correction method significantly improved the coincidence timing resolution of the tagged events. Time-walk was effectively eliminated for $E_{\text{detected}} \gtrsim 100$ MeV.

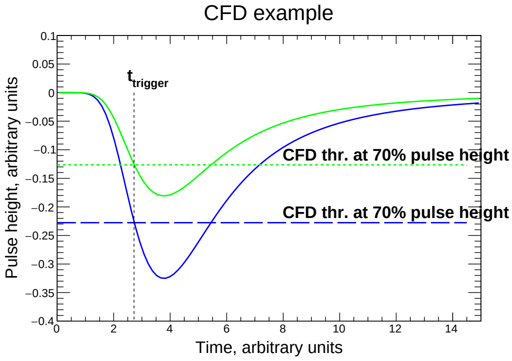

Figure 3.20: Illustration of a constant fraction discriminator. The discriminator threshold is set to a certain fraction of the pulse height (70% in this example), pulses with different heights pass the threshold at the same relative time.

The strongest time-walk effects were observed in the BUNI detector. In the DIANA detector the time-walk was moderate and no time-walk could be seen in the CATS detector. The difference between the detectors was due to hardware setup. The trigger pulse from each detector was created through feeding an analog signal (sum of the seven core PMTs in BUNI, central core PMT in CATS and DIANA, see Section 2.1.4) to a Constant Fraction Discriminator (CFD). A CFD is a device that produces a logic signal when the input pulse reaches a certain fraction of its total height. The working principle of a CFD is depicted in Figure 3.20. If a CFD is configured correctly the time-walk effects as illustrated in Figure 3.16 are eliminated. However only the CFD of the CATS trigger was properly configured and thus time-walk was present in BUNI and DIANA.

3.8 Determining cosmic filters

Cosmic muon background was present and recorded throughout the whole experiment and had to be separated from tagged-photon induced data. Filters were established by using the beam-off cosmic data (see Section 2.2.4) and the in-beam data (where the proportion of cosmic-ray events is small) to distinguish between cosmic background events and potential signal events. Cosmic rays typically caused a significantly larger energy deposit in the annulus as compared to the tagged photons that entered the detector through the front collimator. This is illustrated in Figure 3.21. The tagged events always induced the largest EM shower in the core crystal with moderate shower leakage to the annulus. The cosmic rays on the other hand always passed through at

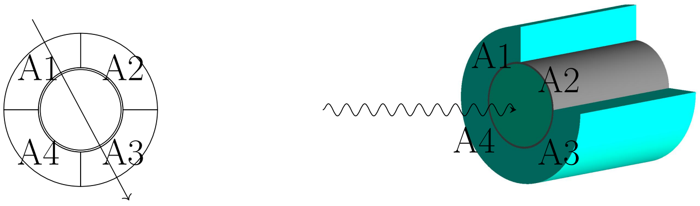

Cosmic event

Calibration event

Figure 3.21: Illustration of a typical cosmic event and a typical calibration event, BUNI detector. A1 to A4 enumerate the NaI(TI) annular segments.

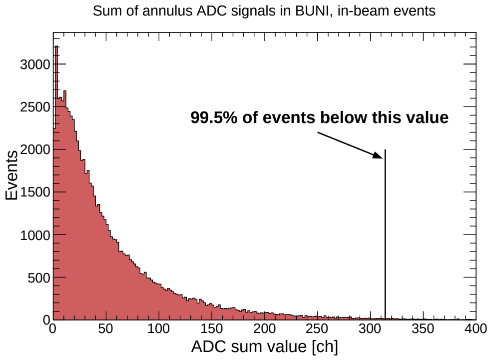

Figure 3.22: Sum of the ADC signals from BUNI NaI(TI) annulus for the in-beam events. The value below which 99.5% of the events lay is indicated.

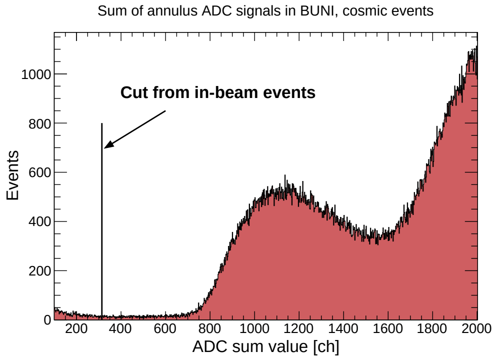

Figure 3.23: Sum of the ADC signals from BUNI NaI(TI) annulus for purely cosmic events. The cut value from the in-beam data is indicated.

least two annular pieces and thus created considerable energy deposits there.

To determine the cosmic filter for a detector, a histogram of the sum of the NaI(TI) annulus QDC signals was filled for the tagged in-beam events. The filter was defined as the ADC channel below which 99.5% of the tagged in-beam events lay. Figure 3.22 depicts the sum of the annulus ADC signals for the tagged in-beam events and the established cosmic cut in the BUNI detector. Figure 3.23 displays the sum of the annulus ADC signals for beam-off cosmic events and indicates the cut value from the in-beam events. Testing the established filters on beam-off cosmic events for all three detectors indicated cosmic identification efficiencies of $\sim$ 98%, $\sim$ 96% and $\sim$ 92% for BUNI, CATS and DIANA, respectively.

In practice the 99.5% limit established from the in-beam data (ADC channel value 314 in Figure 3.22) cut a slightly different proportion of the scattering data, because the photons from the reactions in the target were not as well collimated and were likely to have a somewhat different signature in the summed annulus ADC signal. This effect was accounted for in the acceptance calculation in Sections 5.3 and 6.3.

The front vetoes of the detectors were not used to filter events, as they output low quality signals that were not trustworthy. The front vetoes were intended to allow elimination of background induced by charged particles, e.g. the protons from the photodisintegration reaction $\gamma + {}^2\mathrm{H} \rightarrow \mathrm{n} + \mathrm{p}$. However, as discussed in Section 4.3, the background channels with charged particles in the final state were effectively eliminated with cuts on the detected energy and the front veto signals were not required.

It should be noted here for clarity that the filtering technique presented in Section 3.6 serves a different purpose than the cosmic filtering technique discussed in this section. The latter is introduced to suppress the cosmic event contribution to the π^- capture/Compton scattering signal, whereas the former aims to select out the cosmic events that have a similar path length through the core crystal.

3.9 Energy calibration correction

After the detector calibration steps presented in the previous sections, the random background removal technique discussed in the next chapter was applied to extract the tagged event (signal) energy spectrum in each detector. The spectra were necessary to correct for systematic effects that caused energy calibration offsets in the detectors.

In general, there were two aspects that affected the energy calibration of the detectors. First, the energy calibrations of the detectors were offset due to uncertainties related to the electron beam energy and the calibration of the tagging spectrometer. The relation between an electron hit position at the FP detector and the tagged photon energy depends on the electron beam energy, the magnetic field map of the tagging magnet and the positioning of the focal plane detector relative to the radiator and the tagging magnet. The calibration of the electron beam and the tagging system caused the same offset in each detector in every run period (see below).

Second, the energy calibrations were offset due to unknown pedestals during the in-beam measurements. The in-beam events were triggered only from the detector which lay in the tagged photon beam path. Therefore the pedestals were not visible in the in-beam data. The pedestal values for the analysis of the in-beam data were extracted from data files taken immediately before or after the in-beam measurement. This presented a potential problem due to the pedestal drifts described in Section 3.5. The pedestal drifts were the strongest in the BUNI detector and were also to an extent observed in the CATS detector. In the DIANA detector the pedestals were very stable throughout the different run periods. Due to this, an energy calibration offset in the DIANA detector could have only been caused by the uncertainties in the tagging system calibration. The energy calibrations of CATS and BUNI could have been affected both by the uncertainty of the tagging system calibration and the pedestal shifts.

Figure 3.24 depicts the energy calibration fit for the BUNI detector with the full detector response from Eq. (3.10) on the x-axis and the tagged photon energies on the y-axis. This is the equivalent of Figure 3.6, but the detector response includes the signals from the annulus. The detected energy for each event in the main experiment was calculated as

$$E_{\text{detected}} = \mathcal{R}_{\text{evt}} \cdot a_{\text{cal}} + b_{\text{cal}}, \tag{3.13}$$

with $\mathcal{R}_{\text{evt}}$ defined by Eq. (3.12) and a_{cal} and b_{cal} from the fit in Figure 3.24. The calibration offset of the tagging system shifted the y-axis values in Figure 3.24. Using the incorrect pedestal values for the in-beam data on the other hand affected the x-axis. In either case the slope and the intercept of the fit line were affected and caused Eq. (3.13) to yield too high or too low detected energy values. The best indication of an energy calibration offset was the location of the π^- capture peak in the signal spectrum of each detector.

The photon spectrum of the π^- capture reaction $\pi^- + {}^2\text{H} \to \gamma\text{nn}$ has a strong peak at ∼130 MeV and was simulated accurately in each detector by taking into account the theoretical model of the capture process and the detector resolution effects (see Appendix A.4). To determine the energy calibration offsets, the experimentally measured π^- capture peaks in different detectors were compared with the simulation. The comparison could be performed only after the data reduction and the random subtraction procedures, which are discussed in detail in Section 4.1 and Section 4.2, respectively. Once these steps had been carried out, the data were fitted with the shape from the simulation. The only free fit parameter was the shift of the simulated spectrum along the detected energy axis.

An example offset fit is depicted in Figure 3.25. The black data points represent

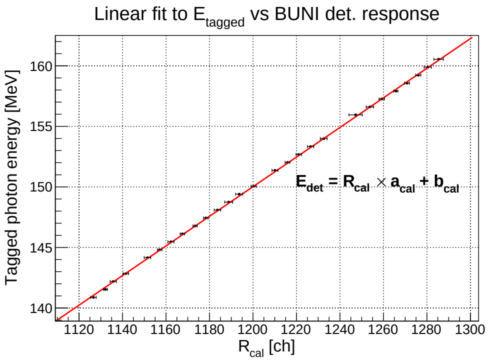

Figure 3.24: BUNI energy calibration fit. Detector response $\mathcal{R}_{\mathrm{cal}}$ (Eq. 3.10) on the x-axis, tagged photon energies of the y-axis.

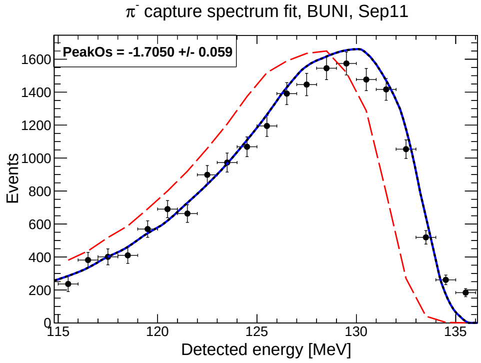

Figure 3.25: Example fit to determine the energy calibration offset.

the π^- capture peak in the BUNI detector in the September 2011 run period. The red dashed line is the model of the π^- capture peak in BUNI from the simulation. The blue line is the result of fitting the simulation to the data by allowing the model spectrum to shift along the detected energy axis. As indicated, this particular fit suggests that the peak in the measured data lay ~1.7 MeV higher than the simulated peak.

First order correction to the tagging system calibration

The calibration offset analysis was performed in multiple steps. First, the fit to the data from the DIANA detector was used to find a first order correction for the tagging system calibration. As a result, the energies of all focal plane detector channels were shifted down by $\mathrm{OS}^{(1)}_{\mathrm{tagg.sys.}} = \sim 5$ MeV. To check that a constant offset was justified, the data in the 31 focal plane detector channels was binned to eight energy bins. The π^- capture peak was fitted separately in each energy bin. No trend in the offset value was observed, indicating that the offset related to the tagging system was constant over the full range of the focal plane detector.

The constant offset could be explained by an uncertainty related to the energy of the electron beam. The tagging magnet and the focal plane detector determined the momenta of the post-bremsstrahlung electrons. The energies of the tagged photons were then calculated as $E_\gamma = E_e - E'_e$ (consult Figure 2.1). Thus, a $\mathrm{OS}^{(1)}_{\mathrm{tagg.sys.}} = \sim 5$ MeV offset in the electron beam energy would explain the observed constant offset in every focal plane detector channel. The original tagging system calibration assumed an electron beam energy of $E_e = 193$ MeV, so the 5 MeV correction means a shift of 2.6%. According to experts at MAXLab [109] such an uncertainly in the electron beam energy was plausible. However, irrespective of whether the calibration offset caused by the tagging system was due to the electron beam energy or some other effect, correct energies corresponding to the focal plane detector channels were obtained under the two following conditions. Firstly, the simulated π^- model had to be accurate. The model (Gibbs *et. al.* [110, 111]) employed has been shown to be in excellent agreement with experiment in the peak region [106] and is trustworthy. Secondly, the detector calibration as illustrated in Figure 3.24 had to remain linear down to the region where the π^- peak lies (approximately 10 MeV below the lowest tagged photon energy). This assumption is demonstrated to be correct by comparing the measured cross-section with theoretical models in Chapter 5 Figure 5.20. If the assumption was wrong, the threshold of the π^- photoproduction reaction would not match the threshold location predicted by the theoretical models. Thus it is concluded that correct energies corresponding to the focal plane detector channels were obtained.

First order combined corrections

Once the $\mathrm{OS}^{(1)}_{\mathrm{tagg.sys.}} = \sim 5$ MeV tagging system correction had been applied, the calibration steps as outlined in the previous sections had to be repeated. Then the first order combined energy calibration offsets were found. To that end the fits as depicted in Figure 3.25 were repeated for each detector in the September 2011[2] and April 2015 run periods. Each fit was performed in the energy range 100 − 140 MeV, 110 − 140 MeV and 120 − 140 MeV to assess the sensitivity of the extracted offset to the selection of the fit range. The offsets are summarised in Table 3.1.

First order combined corrections

Detector	$\mathrm{OS}^{(1)}_{\mathrm{comb.}}$ Jun/Sep11 [MeV]	$\mathrm{OS}^{(1)}_{\mathrm{comb.}}$ Apr15 [MeV]
BUNI	-1.57 ± 0.12	-0.38 ± 0.03
CATS	-0.24 ± 0.11	0.23 ± 0.05
DIANA	0.04 ± 0.03	-0.19 ± 0.03

Table 3.1: First order combined energy calibration offset corrections for different detectors in different run periods. The uncertainty indicates the sensitivity of the extracted offset to the selection of the fit range.

As the offset due to the tagging system had been corrected to first order by using the DIANA detector data from the September 2011 run period, the corresponding combined offset is very close to 0 as expected. The energy calibration offsets were the largest in the BUNI detector, especially in the June/September 2011 run period. This is believed to have been caused by the use of incorrect pedestal values in analysing the in-beam data. After the first order correction to the tagging system calibration, the offsets in the CATS and DIANA detectors were all within ±0.25 MeV. Moreover, an uncertainty of ±0.4 MeV also includes the BUNI result from April 2015. From this it was concluded that the correction method for the tagging system calibration was correct and that the CATS detector calibrations were not strongly influenced by the pedestal drifts.

Second order combined corrections

As the final step, a second order tagging system calibration correction was calculated as an average of all DIANA and CATS fits, resulting in $\mathrm{OS}^{(2)}_{\mathrm{tagg.sys.}} = -0.04$ MeV. In principle the calibration steps of this chapter should have been repeated again, after which the analysis of the above paragraph would have given the second order combined corrections. However, as the second order correction to the tagging system is very small,

---

[2] June and September 2011 data collection periods used the same in-beam calibration runs, meaning the energy calibration offsets are the same for the two datasets.

it was more practical to calculate the combined second order corrections as

$$\mathrm{OS}^{(2)}_{\text{comb.}} = \mathrm{OS}^{(1)}_{\text{comb.}} + \mathrm{OS}^{(2)}_{\text{tagg.sys.}}. \tag{3.14}$$

The combined energy calibration offsets were calculated for each detector in every run period and were all assigned an combined uncertainty of 0.4 MeV. The results are summarised in Table 3.2.

Second order combined corrections

Detector	$\mathrm{OS}^{(2)}_{\text{comb.}}$ Jun/Sep11 [MeV]	$\mathrm{OS}^{(2)}_{\text{comb.}}$ Apr15 [MeV]
BUNI	-1.6 ± 0.4	-0.4 ± 0.4
CATS	-0.3 ± 0.4	0.2 ± 0.4
DIANA	0.0 ± 0.4	-0.2 ± 0.4

Table 3.2: Second order combined energy calibration offset corrections for different detectors in different run periods.

Implications

As was discussed above, one result of the calibration offset analysis was that the tagged photon energies corresponding to the focal plane detector channels were modified. As the systematic uncertainty of the correction method was estimated to be ±0.4 MeV, the tagged photons were also determined with a systematic uncertainty of ±0.4 MeV.

The calibration corrections as summarised in Table 3.2 were taken into account when detected energies were calculated. Due to the uncertainty associated with the calibration correction method the detected energy in each detector had a systematic uncertainty of ±0.4 MeV. This affected the energy cuts, for example the energy cut $120 - 133$ MeV could have actually been constraining data to the region $120.4 - 133.4$ MeV. The effect of the uncertainty on the energy cuts is taken into account in the acceptance analyses in chapters 5 and 6.

Chapter 4

Background removal

This chapter provides a discussion of various background sources and outlines the principles of data reduction and background removal. The first section details the necessity and the procedure of data reduction. In Section 4.2 the origin and the removal of the random (untagged) events is outlined. Sections 4.3 and 4.4 provide a detailed account of the *physics backgrounds* (contaminating reaction channels) to the π^- and the Compton signals, respectively.

4.1 Data reduction

After the calibration procedures of the previous chapter the data reduction was performed. The purpose of the data reduction procedure was to exclude easily identifiable background events and produce a smaller dataset of the so-called *skimmed* events. The skimmed dataset was subjected to further analysis to extract the cross-section for π^- photoproduction (Chapter 5) and the differential cross-section for Compton scattering (Chapter 6). The reduction procedure was necessary for practical reasons. For example, the raw data from April 2015 run period amounted to $\sim$ 70 gigabytes, but the skimmed dataset was only about 500 megabytes in size. As the development of the analysis software and the signal extraction procedure required several iterations over the events, they could practically only be performed with the skimmed dataset. The data reduction filters were very simple. For each NaI(TI) detector an event was selected for further analysis if:

1. the energy in the detector was between 50 and 250 MeV *and*
2. the event was not identified as a cosmic event.

The cosmic filters that were used in the data reduction procedure are defined in Section 3.8.

4.2 Random (untagged) background

One of the key features of the analysis was the separation of the tagged events and random (untagged) events. The separation was performed with the use of the timing coincidence spectrum. As was discussed in Section 2.1.1, the tagged events (i.e. the events that had an associated electron hit in the focal plane detector) always occurred within a narrow time window. In the untagged events the true electron that emitted the Bremsstrahlung photon which led to the trigger did not create a hit in the focal plane detector. Instead the stop signal (see Figure 2.1) came from an electron in random coincidence. Because of this, the untagged events occurred over a broad range in time, some of which fell in the time window of the true coincidences. The creation of a highly energetic Bremsstrahlung photon with $E_\gamma > 160$ MeV is a good example of an untagged event. In this case the resulting post-Bremsstrahlung electron has low momentum and in Figure 2.1 it bends to the far right and misses the focal plane detector.

The ratio of signal (tagged) events to random (untagged) events is related to the intensity of the electron beam. Lowering the intensity lowers the electron hit rates in the focal plane detector channels and improves the signal to background ratio. At very low intensity, as was used during the in-beam calibration measurements, the random background is negligible. However, a high intensity electron beam was necessary to produce a high flux of Bremsstrahlung photons on the target. Running the experiment at the electron beam intensity where the random background is very small would take several orders of magnitude longer to obtain a similar number of signal events.

The procedure of random background removal is illustrated in Figure 4.1. The top left panel depicts an example timing coincidence spectrum corresponding to the skimmed events in the CATS detector. A narrow coincidence peak of tagged events is visible above the random background. The MAX-I accelerator at Lund provided a pulse-stretched electron beam, which caused the time structure of the untagged background. Pulse-stretching was necessary to turn the electron pulses from the accelerator

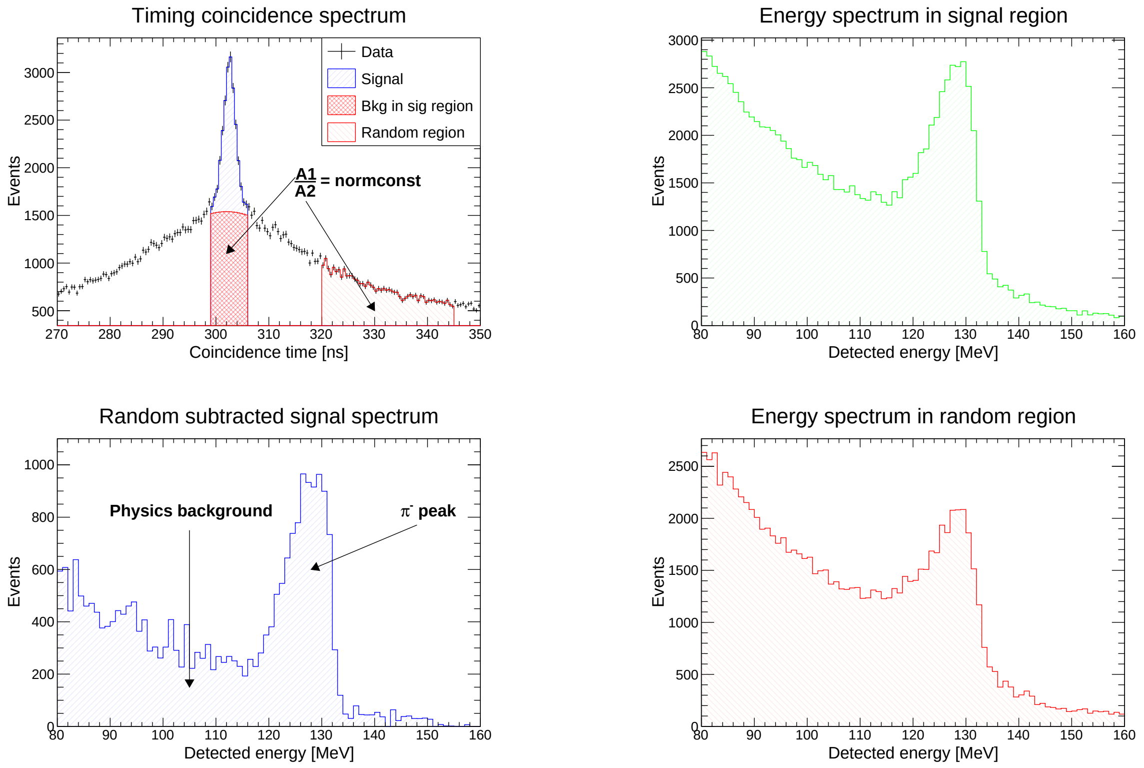

Figure 4.1: Figures illustrating the random background removal.

into a continuous wave electron beam. The experiment as described here could not have been performed with a pulsed beam, as in this case the DAQ and the detectors could not have handled the event rates in the short time intervals when the high intensity pulses arrived at the target. On the other hand, reducing the intensity of the pulses to match the capabilities of the detection system would have also been impractical, as in this case not enough events would have been accumulated in a feasible operation period. The flux of the continuous wave electron beam was modulated by a combination of factors related to the pulse-stretcher ring. The dominant modulation originated from the pulse-stretcher ring frequency of electron transits and there were also contributions from the beam extraction system [79].

To remove the random background the timing spectrum was split into two bands, a signal region and a random region. The CATS energy spectra for events within the signal region and the random region are depicted in the top right and bottom right panels of Figure 4.1, respectively. The signal region of the timing spectrum contained both the "signal" contribution (striped blue) and the "background in signal region" contribution (cross-striped red). As one is interested only in the signal events, the background had to be determined and subtracted. This was achieved through fitting the timing coincidence spectrum with a model containing a shape for the coincidence peak and a shape for the background (fit models are discussed in Section 5.2.1 and Section 6.2.1). Then, a normalisation constant was calculated as a ratio of the background events in the signal time region (denoted A1) to the background events in the random time region (denoted A2). Using the normalisation constant, the random region energy spectrum was scaled and then subtracted from the signal region energy spectrum, yielding the energy spectrum of the signal events (bottom left in Figure 4.1). As expected, in the random subtracted spectrum one can observe a strong peak from π^- capture and physics background at energies below $\sim$ 115 MeV. In principle, the signal yield could be extracted from the random subtracted spectrum by integrating over the π^- capture peak.

The untagged background subtraction technique as presented here relies on the assumption that the energy spectrum of the random events has the same shape in the random region and in the signal region. The uncertainty associated with the random subtraction can be studied through changing the time window of the random region and quantifying the difference it makes to the random subtracted spectrum. However, in this analysis the random subtracted spectra were only necessary for the systematic corrections discussed in Section 3.9. The signal yields were determined directly from the fits to the timing spectra (sections 5.2 and 6.2) and thus the uncertainty related to the random region selection was circumvented. Nevertheless, extracting the random subtracted energy spectrum was an important consistency check that the signal energy spectrum had the shape expected from the contributing reaction channels.

4.3 Physics backgrounds to the π^- signal

The random background removal of Section 4.2 does not eliminate the events produced by tagged photons via background reactions. For example, in addition to the radiative capture events the coincidence timing peak could contain events triggered by photons originating from the decay of photoproduced neutral pions. The Geant4 simulation toolkit was employed to study the physics backgrounds and establish methods for their elimination. The aspects relevant to the simulation work are summarised in Appendix A.

4.3.1 π^0 channel

One of the dominant tagged background channels was the aforementioned π^0 photoproduction, which gave energetic photons through the immediate decay $\pi^0 \to 2\gamma$. The neutral pions were created coherently on the deuteron $\gamma + {}^2\mathrm{H} \to \pi^0 + {}^2\mathrm{H}$ and incoherently $\gamma + {}^2\mathrm{H} \to \pi^0 + \mathrm{n} + \mathrm{p}$ on bound nucleons. The angular distribution of the generated π^0 was sampled from phase space. The simulated signals of π^0 photoproduction in the three detectors are depicted in red in Figure 4.2. In BUNI and DIANA detectors the photons from the π^0 decay had energies up to $\sim$ 105 MeV, in CATS the energies reached $\sim$ 115 MeV. Therefore, the π^0 background was eliminated by restraining the π^- signal integration region to $E_\gamma \geq 120$ MeV. The π^0 background was constrained to $\lesssim 120$ MeV in each detector because the two photons from the immediate decay $\pi^0 \to \gamma\gamma$, emitted back-to-back in the π^0 rest frame, could not enter the same detector due to the low kinetic energies of the π^0.

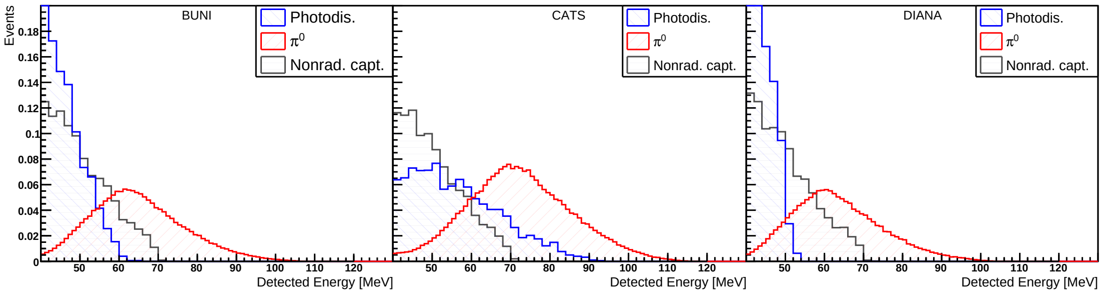

Figure 4.2: Energy spectra of the π^0, photodisintegration and non-radiative capture background reactions in the three detectors.

4.3.2 Proton and neutron background

The photodisintegration channel $\gamma + {}^2\mathrm{H} \to \mathrm{n} + \mathrm{p}$ and the non-radiative capture channel $\pi^- + {}^2\mathrm{H} \to 2\mathrm{n}$ gave energetic protons and neutrons that produced signals in the NaI(TI) detectors. In the simulation of the photodisintegration channel the differential cross-section distribution from Ref. [112] was used to sample the angular distribution of the protons and neutrons. The photodisintegration signals in the three detectors are depicted in blue in Figure 4.2. The energy cuts to remove the π^0 background also eliminated the photodisintegration background.

As the pion capture occurs at rest the non-radiative capture process $\pi^- + {}^2\mathrm{H} \to 2\mathrm{n}$ results in two back-to-back neutrons with equal kinetic energies of $\sim$ 70 MeV. The angular distribution of the neutrons was sampled from phase space. The non-radiative capture signals in the tree detectors are shown with gray in Figure 4.2. The simulated energy deposits are not greater than $\sim$ 70 MeV and the background from the non-radiative capture was eliminated with the cuts applied for the removal of π^0 background.

4.3.3 π^+ and π^- decay

Alongside the negative and neutral pions also positive pions were created. To investigate the background from positive pions 10^6 π^+ particles were created inside the target volume and tracked through the geometry of the experimental hall with Geant4. Unlike the negative pions the positive pions were not captured on the deuteron and instead decayed through $\pi^+ \rightarrow \mu^+\nu_\mu$ 99.99% of the time. The energy deposits in the three NaI(TI) detectors over the 10^6 simulated events were never higher than $\sim$ 50 MeV. Due to this any background from the π^+ photoproduction and subsequent decay was eliminated with sufficiently high energy cuts. The energy deposits in the detectors were the same in the reactions $\pi^+ \rightarrow \mu^+\nu_\mu$ and $\pi^- \rightarrow \mu^-\bar{\nu_\mu}$ and thus the background from the decay of negative pions inside or outside the target volume was also eliminated with the energy cuts.

4.3.4 π^- escape from target volume

As part of the π^- capture efficiency simulations discussed in Section 5.6 the processes where the negative pions were not captured inside the liquid deuterium were investigated to identify potential background sources. As detailed later in Chapter 5, for the π^- analysis the focal plane detector spanning the energy range $140 - 160$ MeV was divided into 8 bins, each approximately 2.5 MeV wide. For the capture analysis 10^6 π^- were created inside the target volume and tracked through the experimental apparatus in the Geant4 simulation. The angular distribution of the pions was sampled from the cross-section of the elementary reaction $\gamma\text{n} \rightarrow \pi^-\text{p}$ [40]. Table 4.1 details the π^- processes by energy bins.

Upper limits for the background contaminations from capture outside the liquid deuterium were established. In the worst case scenario approximately 10% of the pions were captured outside the liquid deuterium. As was already discussed in Section 2.3.1, capture on heavier elements is radiative $\lesssim$ 2% of the time. This means that out of the total created pions $\lesssim$0.2% underwent radiative capture that could have potentially contaminated the signal of π^- capture on the deuteron. This is well below the dominant uncertainties of this analysis and could thus be neglected. It is also worth pointing out that capture in Kapton occurred $\lesssim$ 1% of the time. As the mass fraction of hydrogen in Kapton is approximately 2%, any contamination from the reaction $\pi^- + \text{p} \rightarrow \gamma + \text{n}$ in Kapton was also small enough to neglect.

4.3.5 Scattering and Kapton container background

The simulated elastic (Compton) scattering $\gamma + {}^2\text{H} \rightarrow \gamma' + {}^2\text{H}'$ and inelastic scattering $\gamma + {}^2\text{H} \rightarrow \gamma' + \text{n} + \text{p}$ spectra in the three detectors are depicted in Figure 4.3. The angular distribution of the scattered photons was sampled from phase space. The spectra overlap substantially with the photon spectrum of the radiative capture reaction $\gamma + {}^2\text{H} \rightarrow \gamma + 2\text{n}$, through which the π^- photoproduction cross-section is measured.

π^- processes by energy bins

Bin	En. [MeV]	C_{Target}	C_{Kapton}	C_{Housing}	C_{Air}	Decay	Other
2	147.0	99.46%	0.24%	0.17%	0.02%	0.11%	0.00%
3	149.7	98.71%	0.30%	0.62%	0.10%	0.27%	0.00%
4	152.3	97.34%	0.38%	1.36%	0.25%	0.67%	0.00%
5	154.9	94.75%	0.52%	2.50%	0.77%	1.46%	0.00%
6	157.6	88.71%	0.84%	4.12%	2.24%	4.08%	0.01%
7	159.8	80.85%	1.00%	5.68%	4.03%	8.40%	0.04%

Table 4.1: π^- processes for different energy bins. "C" stands for capture, the subscript specifies the target component where the capture occurred. "Target" refers to the liquid deuterium volume, "Kapton" to the thin kapton container that holds the liquid deuterium and "Housing" to the steel housing that contains the kapton cell. Capture in air occurs when the π^- penetrates the housing wall into the experimental hall. Bin count starts from 0, energy bins 0 and 1 were below the π^- photoproduction threshold.

The scattering backgrounds could not be removed with energy cuts and were accounted for by using the experimentally measured Compton scattering cross-section.

The thin Kapton vessel that held the liquid deuterium was also a source of background. Two types of contamination originated from the Kapton vessel. First, elastic and inelastic scattering occurred from the container. The second type of contamination from the Kapton vessel originated from the events when a π^- was produced in Kapton and captured in the liquid deuterium. Correcting for the scattering (elastic and inelastic) backgrounds from the liquid deuterium and the vessel background was intricately tied to the yield extraction procedure and the relevant corrections are addressed separately in Sections 5.2.4 and 5.2.5.

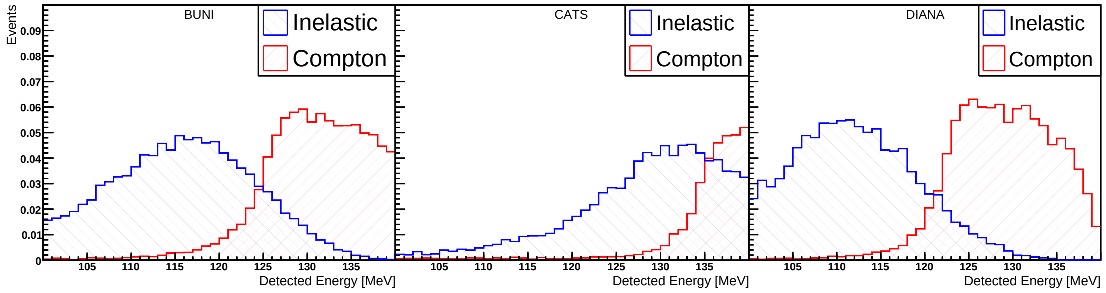

Figure 4.3: Energy spectra of the elastic (Compton) and inelastic scattering in the three detectors.

4.4 Physics backgrounds to the Compton signal

There were fewer background sources in the Compton analysis. The two contaminating channels were the inelastic scattering $\gamma + {}^2\text{H} \rightarrow \gamma' + \text{n} + \text{p}$ and the radiative π^- capture reaction $\pi^- + {}^2\text{H} \rightarrow \gamma + 2\text{n}$. Figure 4.4 depicts the missing energy spectra

$$E_{\text{miss}} = E_{\text{detected}} - E'_{\gamma} \tag{4.1}$$

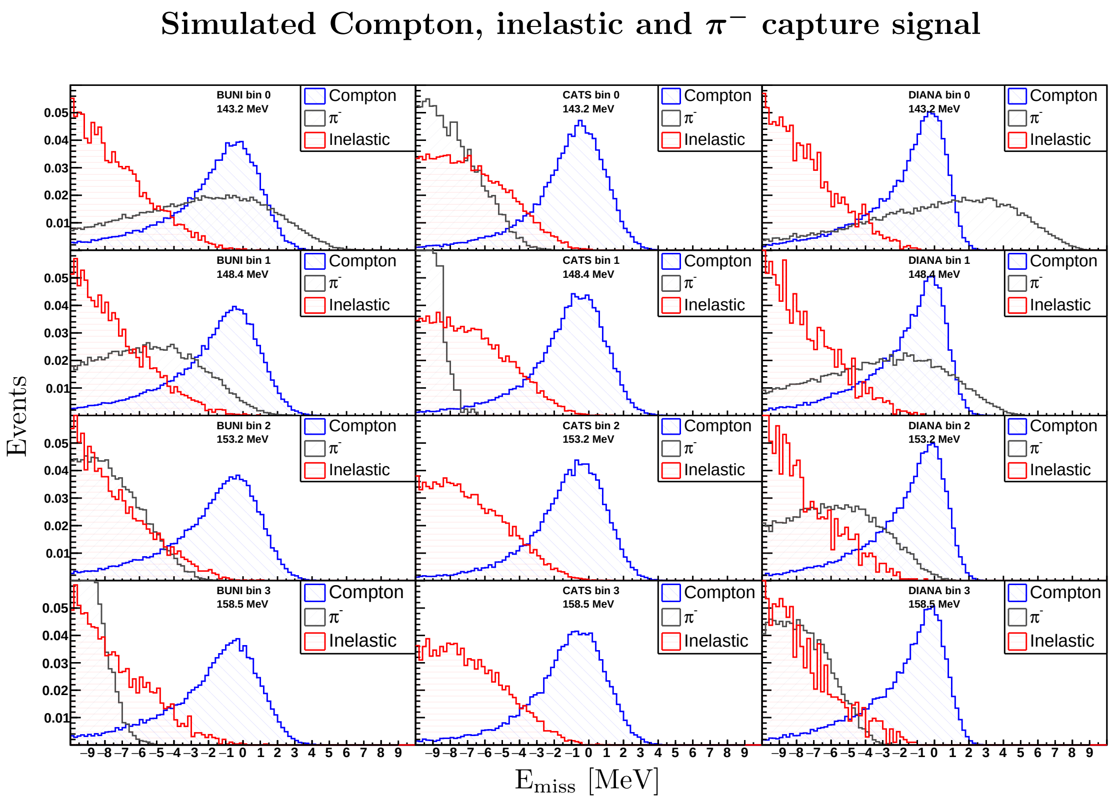

Figure 4.4: Simulated Compton, inelastic and π^- capture signal in the four energy bins used in the Compton analysis for each detector. At the backward angles (BUNI and DIANA) the π^- capture peak overlaps with the Compton signal in the lower energy bins.

in each detector and energy bin for the simulated Compton, inelastic and π^- capture signals. In Eq. (4.1) E_{detected} is the energy of the detected photon and E'_γ is the expected energy of the Compton scattered photon calculated from Eq. (1.15) by using the deuteron mass, the energy of the tagged photon and the angle between the beam direction and the detector. As discussed in Chapter 6 the Compton analysis used 4 energy bins instead of 8 due to substantially lower number of counts compared to the π^- analysis. The inelastic channel was successfully removed by constraining the Compton yield integration to $\mathrm{E}_{\text{miss}} \gtrsim -2$ MeV. The π^- capture signal, however, could not be removed and made it impossible to extract the Compton signal at backward angles in the lower energy bins.

Scattering from the Kapton vessel was a source of background to the Compton scattering signal. The run with the dummy Kapton target (see Section 2.2.3) could be used to correct for the contamination from the Kapton container. This is addressed when the yield extraction is discussed in Section 6.2.

Chapter 5

π^- signal extraction

The energy dependent cross-section for π^- photoproduction in one detector was calculated according to

$$\sigma(E) = \frac{Y(E)}{\Omega_{\mathrm{eff}} \cdot N_\gamma(E)} \cdot \frac{1}{P_c(E) \cdot \kappa_{\mathrm{eff}} \cdot \mathrm{BR}_{\pi^-\mathrm{D}\to\gamma\mathrm{nn}}} \cdot 4\pi \tag{5.1}$$

In Eq. (5.1) $Y(E)$ is the yield of π^- capture events in a given energy bin. Ω_{eff} is the detector acceptance that takes into account the solid angle and the various data cuts. $N_\gamma(E)$ denotes the integrated flux of tagged photons per energy bin. $P_c(E)$ is the energy dependent π^- capture efficiency and κ_{eff} is the effective target thickness. The former is unitless, the latter has units $1/\mathrm{cm}^2$. $\mathrm{BR}_{\pi^-\mathrm{D}\to\gamma\mathrm{nn}} = 0.261 \pm 0.004$ [100, 103] is the absolute branching ratio for the radiative capture out of all possible capture reactions. The 4π compensates for the fact that out of the isotropically emitted radiative capture photons only a fraction are detected due to the solid angle acceptance of the detector. Isotropic emission is expected because the π^- capture occurs at rest.

In every run period each detector was used to determine the cross-section. As there were three run periods, there were in total nine cross-section measurements that ideally would give consistent results.

In this chapter all of the quantities that entered the cross-section calculation are discussed at length. Section 5.1 reviews the binning of the FP detector and the detected energy cuts for signal extraction. Section 5.2 provides a detailed account of the yield extraction procedure. Section 5.3 overviews the calculation of the detector acceptances. Section 5.4 deals with the flux of the tagged photons and Section 5.5 with the effective target thickness. In Section 5.6 determination of the capture efficiency is discussed and finally Section 5.7 presents the results and discussion.

5.1 Binning and energy cuts

After the data reduction of Section 4.1 the yield extraction from the dataset of skimmed events was initiated. First, the binning for the tagged photons was selected. The focal plane detector consisted of 31 channels in the energy range from $140 - 160$ MeV. This determined a maximum energy resolution of $\sim$0.6 MeV for the tagged photons. From the point of view of the analysis such a fine resolution was impractical, mainly because the typical count of capture events associated with a single focal plane detector

Binned tagged photon energies

Bin	Energy [MeV]	Sys. err. [MeV]
Bin 0	141.8	0.4
Bin 1	144.4	0.4
Bin 2	147.0	0.4
Bin 3	149.7	0.4
Bin 4	152.3	0.4
Bin 5	154.9	0.4
Bin 6	157.6	0.4
Bin 7	159.8	0.4

Table 5.1: Tagged (incident) photon energies by focal plane detector bins.

channel was too low. The focal plane detector channels were grouped together by four, resulting in 8 tagged (incident) photon energy bins[1]. With this grouping the width of one energy bin was ~ 2.5 MeV. The average incident photon energies corresponding to the eight bins of the focal plane detector are summarised in Table 5.1. The systematic uncertainty of 0.4 MeV originates from the calibration offset analysis discussed in Section 3.9. Note that throughout this chapter the bin count starts from zero, not one.

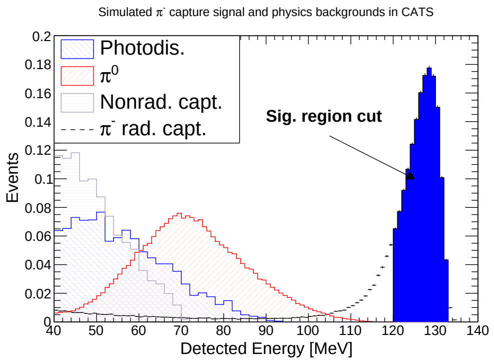

Figure 5.1: Simulated capture signal and physics backgrounds in CATS. The blue filled region indicates the energy range over which the signal was integrated.

The analysis of the physics backgrounds in Section 4.3 revealed that most of the backgrounds could be removed by constraining the lower integration limit of the π^- capture signal to 120 MeV. The theoretical end point of the capture spectrum is 131.4 MeV. Due to the resolution of the detectors the measured energy spectra extended a few MeV higher. For the analysis the energy cut $120 - 133$ MeV was used. The simulations of the π^- capture peak and the dominant physics backgrounds (see Section 4.3) in CATS are depicted in Figure 5.1. Once the energy cut was selected, the timing coincidence spectra corresponding to the eight energy bins were filled. The spectra are depicted in Figure 5.2. Due to the energy cut $120 - 133$ MeV the coincidence peaks consisted almost entirely of the π^- capture events. However, the cut did not remove the scattering backgrounds (elastic and inelastic scattering from the deuteron) and the background from the Kapton vessel (see Section 4.3.5). Neglecting these for now (scattering and Kapton backgrounds are addressed later in Section 5.2.4 and Section 5.2.5), the counts in the coincidence peaks were the π^- capture yields of Eq. (5.1). All other backgrounds were removed by the energy cut and thus gave no contribution to the timing coinci-

---

[1] The first seven bins consisted of four, the eighth bin of three FP channels.

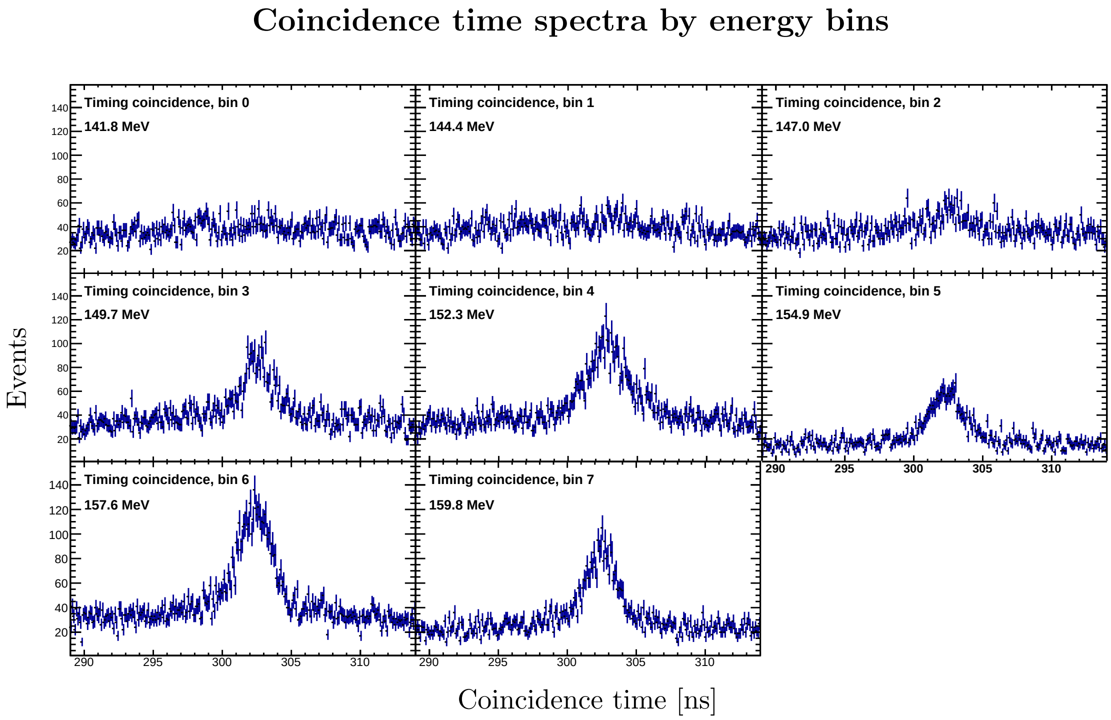

Figure 5.2: Coincidence time spectra for the CATS detector in eight incident photon energy bins, September 2011 run period. 0.1 ns binning has been used, determined by the resolution of the TDCs.

dence histograms displayed in Figure 5.2. Hence the yields were extracted directly from the fits to the timing spectra and random subtracted energy spectra as described in Section 4.2 were unnecessary for the yield analysis. The random subtracted energy spectra were only necessary for the calibration offset analysis (Section 3.9).

5.2 Yield

The extraction of the π^- capture yields relied on the fits to the timing coincidence spectra depicted in Figure 5.2. The fits were performed using the RooFit [113] package of ROOT [114]. The fitting procedure is discussed in the subsections below.

5.2.1 The fit model

As a first step a fit model with components for the coincidence peak and the untagged background had to be selected. The former was represented by a Gaussian, but modelling the latter was not trivial. As was discussed in Section 4.2, the time structure of the background was related to the electron beam stretching technique with various effects modulating the intensity of the tagged photon beam. The modelling difficulty was circumvented by using the summed spectrum of the first two energy bins to estimate the shape of the untagged background. The first two bins were below the π^- photoproduction threshold on the deuteron, as energy bin 1 extended to a photon energy of 145.5 MeV. The π^- threshold is expected at 145.8 MeV [45] and bin 2 was the first bin

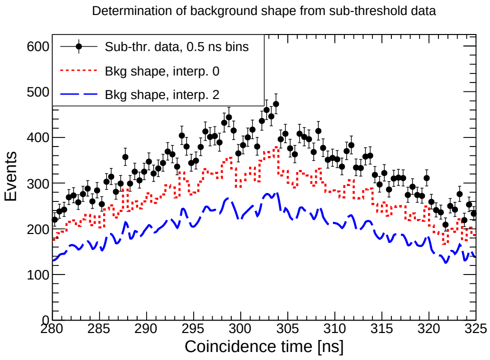

Figure 5.3: Background determination from sub-threshold data (black data points), data in 0.5 ns wide bins. Red dotted curve - extracted shape without interpolation, blue dashed curve - extracted shape with second order interpolation. The extracted shapes have been scaled down to allow visual comparison.

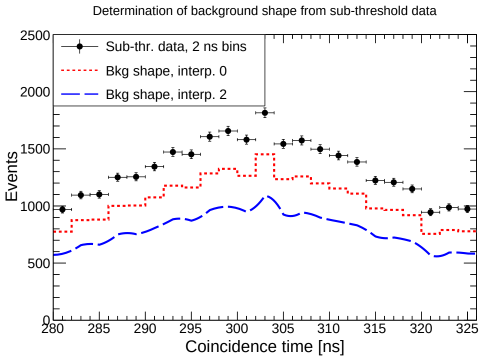

Figure 5.4: Background determination from sub-threshold data (black data points), data in 2 ns wide bins. Red dotted curve - extracted shape without interpolation, blue dashed curve - extracted shape with second order interpolation. The extracted shapes have been scaled down to allow visual comparison.

with the π^- signal. From here onward the sum of the timing coincidence histograms of energy bins 0 and 1 (first two in Figure 5.2) is referred to as sub-threshold data.

Figures 5.3 and 5.4 illustrate estimation of the background shape from sub-threshold data. In the RooFit package extraction of a fit shape from a histogram is handled by the class `RooHistPdf`. The resulting curve depends on the binning of the histogram and on an interpolation parameter that is provided as input. If the interpolation parameter is greater than zero, the software smooths the extracted shape.

The TDCs had a resolution of 0.1 ns, which determined the binning of the histograms depicted in Figure 5.2. However, fine binning was impractical for the background extraction because of the significant statistical fluctuations in individual bins and the sub-threshold data had to be regrouped to wider bins. It was important to smooth out the statistical fluctuations, as they affected the yield extraction in the lower energy bins where the count of signal events was low. In Figure 5.3 0.5 ns binning for the sub-threshold data was used. Two versions of the extracted background shape are depicted, one without interpolation and one with second order interpolation. The 0.5 ns bins were still too narrow to obtain a smooth curve. In Figure 5.4 2 ns binning for the sub-threshold data was used. In this setting the statistical fluctuations became small and the interpolated curve provided a reasonable representation of the background shape. The dashed blue line in Figure 5.4 was combined with a Gaussian for the coincidence peak to perform fits to the timing spectra in energy bins $2-7$. Example fits are depicted in Figure 5.5.

The small bump in the extracted background shape at $\sim$ 303 ns (dashed blue line in Figure 5.4) is believed to originate from the scattering background (coincidences from elastic and inelastic scattering). Thus it is not interpreted as a mere statistical fluctuation to be smoothed out by selecting a more coarse binning for the sub-threshold data. The data as displayed in Figure 5.4 is not itself sufficient to support this interpretation. However, based on the cross-sections presented in Chapter 6 and the calculations presented in Section 5.2.4 a minimum of $\sim$50 and a maximum of $\sim$200 scattering

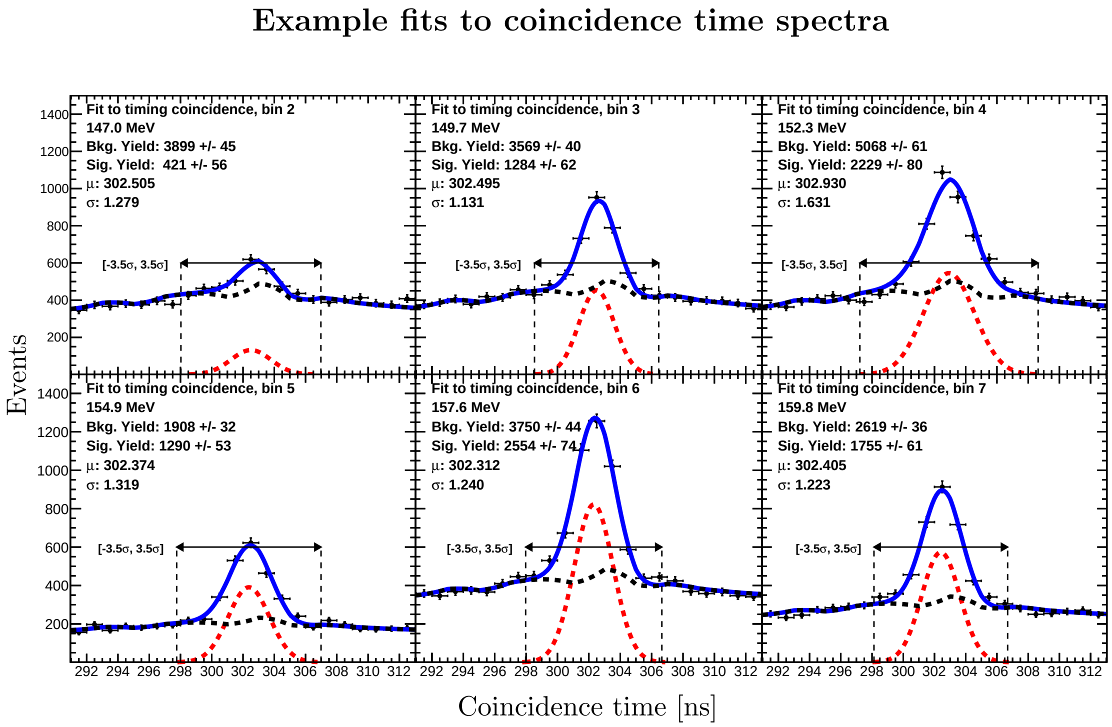

Figure 5.5: Fitted coincidence time spectra in the CATS detector in the energy bins $2-7$, September 2011 run period. The Signal Yield indicates the count of π^- capture events and the Background Yield the count of untagged background events within the yield integration range $\pm 3.5\sigma$ (see Section 5.2.2).

coincidences (Eq. (5.7)) are expected in the sub-threshold data of Figure 5.4. This estimation is the reason why the small bump is believed not to be a mere statistical fluctuation. The presence of the scattering coincidences in the background shape is discussed in detail in Section 5.2.4.

The dependence of the yields on the binning and interpolation of the sub-threshold data was investigated. To that end the background shape was also extracted from the sub-threshold data that was grouped to 1 ns bins. First, second and third order interpolations were tested. The resulting variation in the background shape changed the yields by $\sim$1% in bins $3-7$. Due to the low signal count the yield in bin 2 was slightly more sensitive and changed typically by $\lesssim$5%.

5.2.2 Yield integration range

To determine the yields from the fits exemplified in Figure 5.5 an integration range over the coincidence peak had to be selected. Figure 5.6 depicts the quantity

$$f(n) = \frac{\sum\limits_{\mathrm{i}=2}^{7} Y_{\mathrm{i}}^{(\pm n\cdot\sigma)}}{\sum\limits_{\mathrm{i}=2}^{7} Y_{\mathrm{i}}^{(\pm 5\cdot\sigma)}}, \tag{5.2}$$

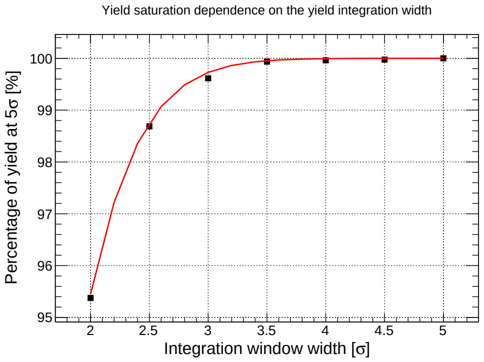

Figure 5.6: Yield saturation dependence on the yield integration width (Eq. (5.2)). The red line depicts the expected saturation curve of an ideal Gaussian. Yield integration widths are illustrated in Figure 5.7.

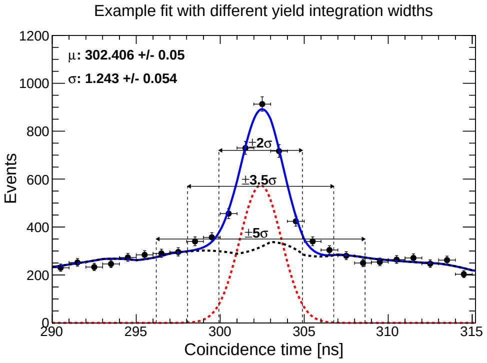

Figure 5.7: An example fit illustrating the yield integration widths on the x-axis in Figure 5.6. Black dashed - untagged background, red dashed - coincidence peak, blue solid - combined model fitted to experimental data (black data points).

where $Y_{\mathrm{i}}^{(\pm n\cdot\sigma)}$ is the signal yield in energy bin i when the integration over the coincidence peak was performed in the range $(\pm n \cdot \sigma)$. The denominator is the sum of the yields in bins $2-7$ when the integration range was $\pm 5\sigma$ (σ stands for the standard deviation of the coincidence peak). The saturation curve expected from an ideal Gaussian is depicted with the red solid line in Figure 5.6. Figure 5.7 displays an example fit and the different yield integration widths. For this analysis the yield integration range $\pm 3.5\sigma$ was used, as it contained practically 100% of the timing coincidences. The $\pm 3.5\sigma$ range was determined individually for each bin, using the standard deviation of the coincidence peak returned by the fit (σ parameter values in Figure 5.5).

5.2.3 Determination of the yield values

The π^- capture yields were determined from the fits to the coincidence spectra as exemplified in 5.5. For the fitting procedure the coincidence spectra of energy bins $2-7$ in Figure 5.2 were regrouped to 1 ns bins, as fits to the coincidence spectrum in energy bin 2 occasionally failed to converge when 0.1 ns binning was used. The regrouping had a very small effect on the extracted yields in energy bins $3-7$ ($\sim 1\%$) and a slightly larger effect in energy bin 2 ($\lesssim 5\%$). Note that the regrouping of the fitted spectra (energy bins $2-7$) does not affect the binning of the sub-threshold data discussed in Section 5.2.1.

The fitting was performed in two steps. First, each spectrum was fitted several times using a Maximum Likelihood (ML) estimation with the mean and sigma of the coincidence peak and the signal-to-background ratio as free parameters. In between fits the parameters were randomised within realistic limits. The purpose of this procedure was to make certain that the global maximum of the likelihood was found by the numeric minimiser[2]. The mean and sigma of the coincidence peak were then fixed from the result with the highest value of the likelihood and Extended Maximum Like-

---

[2] ROOT employs the MINUIT minimiser [115], which is designed to find the minimum of a function. In practice the maximum likelihood L is found through minimizing the negative of the logarithm $-\log L$.

lihood (EML) fits were performed. For the EML fits the signal-to-background ratio was replaced with two new parameters, which were the yields of the signal and the background. As before, several EML fits were performed to each spectrum to make certain that the global maximum of the likelihood was found. The fitting was performed in two steps because the EML fits tended not to converge when, in addition to the yields, the mean and the sigma of the coincidence peak were free parameters. The two-step procedure allowed this problem to be circumvented by fixing the properties of the coincidence peak from the ML fits.

It is a useful feature of the RooFit package that, with EML estimation, the signal and background yields become fit parameters that are output from the minimiser. Hence, no further manipulation of the spectra were necessary after the EML fits. With the EML method the error propagation is handled by the minimiser (see Section 3 in Ref. [116]). As the the mean and the sigma of the coincidence peak were fixed from the ML fits the background yield was the only other free parameter in the EML fits. Thus the uncertainty of the signal yield from the minimiser was the statistical uncertainty corrected by the correlation factor of the signal yield and the background yield. In this analysis the uncertainty from the minimiser is used as the estimate for the statistical uncertainty.

The extracted yields were sensitive to the fit range (not to be confused with the yield integration range of Section 5.2.2). This was addressed by performing several fits to each coincidence spectrum in different fit ranges. The narrowest range was approximately $\pm 5\sigma$ from the mean of the coincidence peak, σ being the peak width. The fit range was widened from both ends in 4 ns steps, the widest fit range was $[-5\sigma - 12\,\mathrm{ns},\ 5\sigma + 12\,\mathrm{ns}]$. The different fit ranges are illustrated in Figure 5.8. Yields were calculated as averages of the yields from the four fits

$$\overline{Y} = \sum_{i=1}^{4} \frac{Y_i}{4}. \tag{5.3}$$

Figure 5.9 depicts the quantities $(\overline{Y} - Y_i)/\overline{Y}$ for each fitted energy bin, where the index i runs over the four fits in different ranges. The selection of the fit range affected the yield typically by $\lesssim 2\%$, except in energy bin 2, where the sensitivity was increased

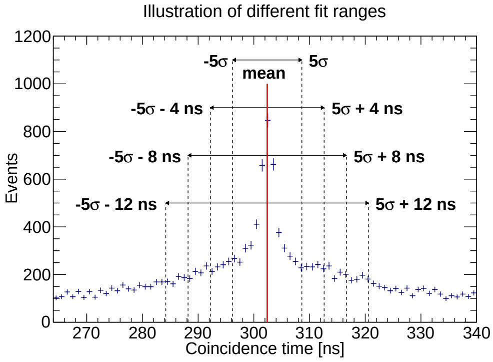

Figure 5.8: The different fit ranges were determined by the mean and the sigma of the coincidence peak.

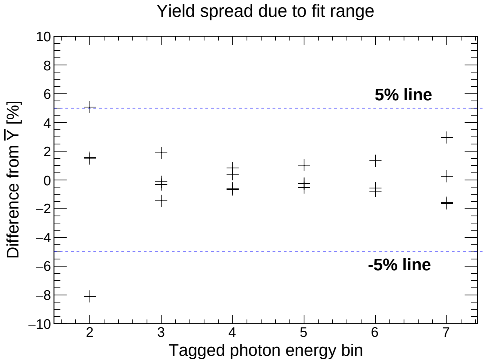

Figure 5.9: The spread of the yields from fits in different ranges. Some points overlap completely. In bin 6 one point is missing due to a non-convergent fit.

to $\sim 7\%$ due to the low count of signal events. Tables 5.2 – 5.4 provide the extracted yields in the three detectors in different run periods. Note that the yields in a detector are expected to vary between run periods due to the variation in the tagged photon flux. The yield extraction failed for energy bin 2 in CATS in the run period in June 2011. Due to low event count in that bin the fits did not converge.

Yields in BUNI in three run periods

Bin	En. [MeV]	Yield Apr. 2015	Yield Sep. 2011	Yield Jun. 2011
Bin 2	147.0	159 ± 21 (13.2%)	691 ± 62 (9.0%)	115 ± 23 (20.0%)
Bin 3	149.7	593 ± 32 (5.4%)	1971 ± 74 (3.8%)	540 ± 36 (6.7%)
Bin 4	152.3	987 ± 38 (3.9%)	3446 ± 93 (2.7%)	787 ± 39 (5.0%)
Bin 5	154.9	1426 ± 44 (3.1%)	1940 ± 62 (3.2%)	488 ± 29 (5.9%)
Bin 6	157.6	1397 ± 45 (3.2%)	4168 ± 92 (2.2%)	1122 ± 43 (3.8%)
Bin 7	159.8	1151 ± 39 (3.4%)	2801 ± 74 (2.6%)	742 ± 35 (4.7%)

Table 5.2: Yields in the BUNI detector in three run periods.

Yields in CATS in three run periods

Bin	En. [MeV]	Yield Apr. 2015	Yield Sep. 2011	Yield Jun. 2011
Bin 2	147.0	148 ± 24 (16.2%)	428 ± 57 (13.3%)	-
Bin 3	149.7	425 ± 31 (7.3%)	1282 ± 62 (4.8%)	278 ± 29 (10.4%)
Bin 4	152.3	728 ± 34 (4.7%)	2216 ± 80 (3.6%)	507 ± 35 (6.9%)
Bin 5	154.9	946 ± 38 (4.0%)	1287 ± 53 (4.1%)	360 ± 28 (7.8%)
Bin 6	157.6	986 ± 39 (4.0%)	2534 ± 74 (2.9%)	662 ± 36 (5.4%)
Bin 7	159.8	878 ± 35 (4.0%)	1760 ± 61 (3.5%)	477 ± 31 (6.5%)

Table 5.3: Yields in the CATS detector in three run periods.

Yields in DIANA in three run periods

Bin	En. [MeV]	Yield Apr. 2015	Yield Sep. 2011	Yield Jun. 2011
Bin 2	147.0	92 ± 20 (21.7%)	489 ± 60 (12.3%)	66 ± 18 (27.3%)
Bin 3	149.7	392 ± 28 (7.1%)	1204 ± 59 (4.9%)	280 ± 27 (9.6%)
Bin 4	152.3	599 ± 31 (5.2%)	2097 ± 74 (3.5%)	440 ± 30 (6.8%)
Bin 5	154.9	908 ± 37 (4.1%)	1175 ± 49 (4.2%)	311 ± 22 (7.1%)
Bin 6	157.6	864 ± 36 (4.2%)	2444 ± 71 (2.9%)	653 ± 32 (4.9%)
Bin 7	159.8	685 ± 31 (4.5%)	1464 ± 56 (3.8%)	502 ± 28 (5.6%)

Table 5.4: Yields in the DIANA detector in three run periods.

5.2.4 Scattering background

It was concluded in Section 4.3.5 that the background from elastic and inelastic scattering on the deuteron could not be eliminated from the π^- signal. An analysis was performed to estimate the contamination that originated from the scattering channels.

It should be stressed that although the scattering contamination was present, it was small because the cross-sections for elastic and inelastic scattering are approximately two orders of magnitude lower compared to the cross-section for pion production. Thus the several approximations discussed in the paragraphs below are justified in the context of estimation of a small background.

Nature of the contamination

First, the π^- yield extraction method is reviewed in the light of the scattering backgrounds. The sub-threshold data from which the background shape was extracted did not contain any π^- events, but it did contain coincidences from the scattering events. The lack of a substantial coincidence peak in the sub-threshold data (see Figure 5.4) indicates that the scattering backgrounds were relatively small and/or that the acceptance to the scattering channels within energy cut $120 - 133$ MeV was low. Nevertheless, the background shape (dashed blue line in Figure 5.4) did contain some coincidences from the scattering channels, which are contained in the small bump at ~ 303 ns.

To discuss the effect of the scattering coincidences on the background shape, let the fit to the spectrum in energy bin 3 in Figure 5.5 be considered. The coincidence peak consists dominantly of the π^- capture events with a small contribution from the scattering events. Ideally the fit would completely separate the yield of the untagged background Y'_{bkg} and the yield of the coincidences Y'_{signal}, where

$$Y'_{\mathrm{signal}} = Y_\pi + Y_{\mathrm{elastic}} + Y_{\mathrm{inelastic}}. \tag{5.4}$$

In Eq. (5.4) Y_π is the yield of the tagged pion captures and Y_{elastic} ($Y_{\mathrm{inelastic}}$) is the yield of tagged elastic (inelastic) scattering events. However, some coincidences from the scattering events were also present in the background shape. Due to this, some of the signal coincidences counted towards the background yield and not the signal yield. Instead of Eq. (5.4), the yield from the fit result was

$$Y_{\mathrm{signal}} = 1284 = Y_\pi + Y_{\mathrm{elastic}} + Y_{\mathrm{inelastic}} - Y_{\mathrm{elastic\ in\ bkg}} - Y_{\mathrm{inelastic\ in\ bkg}}. \tag{5.5}$$

In Eq. (5.5) $Y_{\mathrm{elastic\ in\ bkg}}$ and $Y_{\mathrm{inelastic\ in\ bkg}}$ stand for the elastic and inelastic scattering coincidences in the background shape.

In order to estimate the contamination from the scattering backgrounds in a consistent manner, Eq. (6.1) from Chapter 6 was inverted to calculate the yields of elastic and inelastic scattering in each energy bin used in the π^- analysis. The scattering yields were calculated as

$$Y(E) = \frac{d\sigma(E)}{d\Omega} \cdot d\Omega(E) \cdot N_\gamma(E) \cdot \kappa_{\mathrm{eff}}. \tag{5.6}$$

The tagged photon flux (N_γ) and the effective target thickness (κ_{eff}) were the same as detailed in Sections 5.4 and 5.5. The acceptance to the inelastic and elastic channels were determined from the simulation in the same manner as the acceptance to the π^- signal in Section 5.3. The estimation of the differential cross-sections is addressed in the next paragraph.

Estimating the differential cross-sections of the scattering backgrounds

The differential cross-section for elastic scattering was measured in the full energy range of the tagged photons with CATS and in the higher energy bins with BUNI (see Chapter 6). However, there is no data on the inelastic cross-section near the pion threshold. The differential cross-sections of elastic and inelastic scattering were estimated with the following procedure. First, the Compton scattering differential cross-section data from the measurements with the CATS detector (Table 6.8) was fitted linearly. The fit was used to estimate the values of the cross-section at the eight tagged photon energies used in the π^- analysis. Below the pion threshold the differential cross-section for Compton scattering reveals only moderate energy dependence [71]. Similar behaviour is expected above the pion threshold, which justifies the linear fit model. Second, the slope and intercept of the linear fit to CATS data were scaled to fit the two data points from BUNI (Table 6.9). Using the scaling factor in combination with the fit line to CATS data allowed estimation of the differential cross-section values at the eight energies in the BUNI detector. The estimation procedure is illustrated in Figure 5.10. Third, as no scattering cross-sections were extracted using the DIANA detector, it was assumed that the differential cross-sections were equal at 120° and 150°. This approximation is again based on the Compton cross-sections below the pion threshold [71], where $d\sigma/d\Omega(E_\gamma, 120°) \approx d\sigma/d\Omega(E_\gamma, 150°)$.

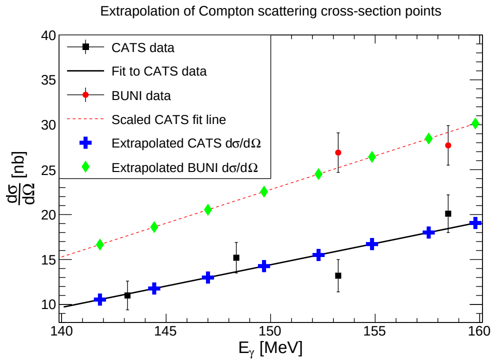

Figure 5.10: Estimating the Compton scattering $d\sigma/d\Omega$ values from data for the BUNI and CATS detectors. Tagged photon energies on the x-axis, $d\sigma/d\Omega$ values on the y-axis.

After this process, the estimated values of the differential cross-section for elastic scattering at the eight energies used in the π^- analysis were available for the three detectors. As at these energies no data exists for the cross-section for inelastic scattering, it was assumed as a first order approximation that the cross-sections for elastic and inelastic scattering have equal magnitude. This is justified as follows. Inelastic scattering from the deuteron $\gamma + {}^2\mathrm{H} \rightarrow \gamma' + \mathrm{n} + \mathrm{p}$ involves photon scattering from the bound neutron or the bound proton, resulting in the break-up of the deuteron. Recall that to the lowest order the scattering cross-section is described by the Thomson limit (see Section 1.2.2), which is proportional to the charge of the scatterer. Thus in the Thomson limit the cross-section for elastic scattering from the deuteron equals the cross-section for scattering from the proton and the neutron cross-section vanishes. Although at energies ∼ 150 MeV the Thomson limit is no longer valid, the data presented in Ref. [117] indicate that at $E_\gamma \sim 200$ MeV the cross-section for scattering from the bound neutron is approximately half of the cross-section for scattering from the bound proton. It is expected that at $E_\gamma \sim 150$ MeV the difference is more pronounced and the assumption $d\sigma/d\Omega_{\mathrm{elastic}} \approx d\sigma/d\Omega_{\mathrm{inelastic}}$ is based on that. The uncertainty due to these crude estimations is addressed at the end of the next paragraph.

Quantifying the contamination

Having estimated the cross-sections, the uncertainty associated with the scattering backgrounds could be quantified. As a first step, the sum of the coincidences of elastic and inelastic scattering in the sub-threshold data was calculated. This was done by using Eq. (5.6) to calculate the scattering yields in energy bins 0 and 1 and adding the four terms together,

$$Y_{\text{scat. bkg}} = Y_{\text{elastic bin 0}} + Y_{\text{elastic bin 1}} + Y_{\text{inelastic bin 0}} + Y_{\text{inelastic bin 1}}. \tag{5.7}$$

The shape of the background was fixed from sub-threshold data (see Section 5.2.1) and the fitting of the coincidence spectra in energy bins $2 - 7$ performed a scaling of the fixed shape. The count of scattering events in the sub-threshold data (Eq. (5.7)) scaled with the background. As a second step a scaling factor was calculated for each fitted energy bin as

$$c_{\text{bin i}} = \frac{\text{Bkg. Yield}_{\text{bin i}}}{\int_{-3.5\sigma_{\text{bin i}}}^{3.5\sigma_{\text{bin i}}} \text{Sub-thr. data}}. \tag{5.8}$$

In Eq. (5.8) the numerator was simply the yield of the background in the yield integration range $[-3.5\sigma_{\text{bin i}}, 3.5\sigma_{\text{bin i}}]$ and was output by the minimiser. The denominator was the integral over the sub-threshold data (black data points in Figure 5.4) in the yield integration range determined by the width of the coincidence peak $\sigma_{\text{bin i}}$.

As a third and final step, for each fitted energy bin the residue of the scattering coincidences in the signal peak was calculated,

$$Y_{\text{scat. residue bin i}} = Y_{\text{elastic bin i}} + Y_{\text{inelastic bin i}} - c_{\text{bin i}} \cdot Y_{\text{scat. bkg}}. \tag{5.9}$$

In Eq. (5.9) $Y_{\text{elastic bin i}}$ ($Y_{\text{inelastic bin i}}$) is the predicted yield of elastic (inelastic) coincidences in the peak from Eq. (5.6), $c_{\text{bin i}}$ is the scaling factor from Eq. (5.8) and $Y_{\text{scat. bkg.}}$ is the count of scattering coincidences in the sub-threshold data from Eq. (5.7). Eq. (5.9) determined the estimated contamination of the scattering events to the π^- capture signal.

The dominant uncertainty of the contamination as determined by Eq. (5.9) originated from the estimated cross-section values. This was addressed by varying the estimated cross-sections and repeating the analysis. The cross-sections for the elastic scattering were scaled up and down by a factor of 1.3 for BUNI and CATS to account for the systematic uncertainties of the measurements reported in Chapter 6. The elastic cross-section in DIANA was scaled up and down by a factor of 1.5 to account for the approximation $d\sigma/d\Omega(E_\gamma, 120^\circ) \approx d\sigma/d\Omega(E_\gamma, 150^\circ)$. The inelastic cross-sections had the largest uncertainties and were scaled up and down by a factor of 2 for all detectors. Thus in total nine different combinations of cross-section values were used to perform the analysis. For each energy bin the largest residual value

$$\sigma_{\text{scat. residue bin i}} = \frac{Y_{\text{scat. residue bin i}}}{Y_{\text{bin i}}} \tag{5.10}$$

from the nine combinations was determined and is reported in Table 5.5. In Eq. (5.10) the numerator is given by Eq. (5.9) and the denominator is the π^- yield from Tables 5.2 – 5.4. Table 5.5 also specifies the sign of Eq. (5.10). Generally the contamination from the scattering backgrounds was estimated to be relatively small. The analysis

Scattering contamination residue by detectors, September 2011

Bin	Energy [MeV]	BUNI [%]	CATS [%]	DIANA [%]
Bin 2	147.0	-3.6	-2.0	5.5
Bin 3	149.7	-4.1	-1.5	4.2
Bin 4	152.3	-3.2	-1.4	2.6
Bin 5	154.9	-3.0	-1.5	0.8
Bin 6	157.6	-2.9	-1.8	-1.9
Bin 7	159.8	-3.1	-2.1	-2.7

Table 5.5: Estimated scattering contamination residue in different detectors and energy bins in the September 2011 run period.

indicated that the contamination was different in the three detectors and contributed to the spread of the π^- photoproduction cross-sections measured with BUNI, CATS and DIANA.

5.2.5 Kapton background

As was explained in Section 4.3.5, there were two types of background from the Kapton vessel that held the liquid deuterium. Photons that scattered from Kapton had similar energies to the photons from the radiative capture and constituted a possible source of contamination. Secondly, pions that were produced in Kapton and subsequently captured inside the liquid deuterium caused false counts towards the yields.

The scattering from Kapton was addressed by subjecting the data collected with the empty Kapton target (see Section 2.2.3) to the analysis performed for the extraction of π^- capture yields. This revealed practically no coincidences in the timing coincidence spectra in the eight energy bins. Indeed, it was shown in Ref. [71] that the scattering from Kapton made only a small contribution to the yields of Compton scattering on the deuteron. As the Compton scattering itself was only a small contamination to the π^- signal, it was concluded that any contamination from the scattering on Kapton was negligible in the π^- analysis.

To estimate the background contribution from the pions produced in Kapton, the effective thickness of the Kapton vessel along the path of the photon beam was calculated in the same way as the effective target thickness of the liquid deuterium in Section 5.5. The chemical properties of Kapton are listed in the database of The National Institute of Standards and Technology [118]. The density is $\rho_{\text{Kapton}} = 1.42\text{g/cm}^3$. The average molar mass was calculated by using the mass fractions of the chemical compounds. The chemical elements in Kapton are Carbon (69.1%), Oxygen (21%), Nitrogen (7%) and Hydrogen (2.7%), yielding $A_{\text{Kapton}} = 12.7$ g/mol. The length of Kapton was defined by the thickness of the end-caps, totalling $L_{\text{Kapton}} = 240\,\mu\text{m}$. The effective thickness of Kapton was determined to be 0.2% of the effective thickness of the liquid deuterium.

From the calculated average molar mass A_{Kapton} six neutrons per atom were assumed. Thus in the most trivial approximation the π^- photoproduction cross-section on Kapton is approximately six times higher than on liquid deuterium. Therefore in this simple model the Kapton contamination was expected to be 1.2%. To be conservative in the uncertainty analysis 1.5% was used.

5.3 Detector acceptance

The detector acceptance was calculated from the Geant4 simulation. $5 \cdot 10^7$ photons were sampled from the theoretical spectrum of the photon energy of the reaction $\pi^- + {}^2\text{H} \to \gamma + 2\text{n}$ and thrown isotropically from the liquid deuterium. The theoretical spectrum of the photon energy (see Appendix A.4) is depicted in Figure 5.11 [110, 111]. The acceptance of each detector was determined by the number of simulated events that resulted in a detected energy within the energy cut used in the analysis (120 − 133 MeV). The acceptance was calculated as

$$\Omega_{\text{eff}} = \frac{N_{\text{det}}}{N_{\text{throws}}} \cdot 4\pi. \tag{5.11}$$

In Eq. (5.11) N_{det} is the number of events within the energy cut in a given detector and N_{throws} is the number of thrown Monte-Carlo events. Figure 5.12 displays the simulated energy spectrum of the photons from the capture reaction in the CATS detector with the energy cut that defined the acceptance (shaded blue). In the following paragraphs various aspects related to the acceptance calculation are addressed.

Detector response effects

The spectra in Figures 5.11 and 5.12 are noticeably different. The simulation took into account the detector response, which resulted in a realistic spectrum for the capture reaction (Figure 5.12). Figure 3.25 demonstrates that, after the correction for the calibration offset, the simulation and the experimental data were in excellent agreement. Simulation of the detector resolution effects is discussed in Appendix A.3. The sensitivity of the acceptance to the simulated resolution effects was investigated by varying the resolution within realistic limits. As a result the acceptance changed typically by $\lesssim 0.2\%$.

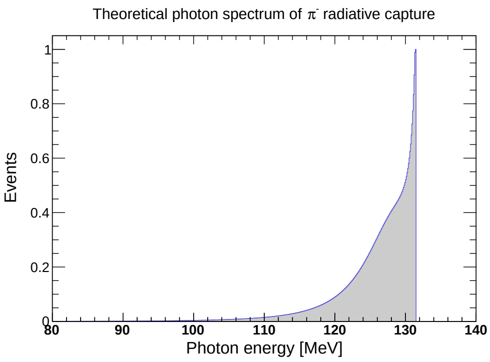

Figure 5.11: Theoretical spectrum of the photon energy of the reaction $\pi^- + {}^2\text{H} \to \gamma + 2\text{n}$ [110, 111].

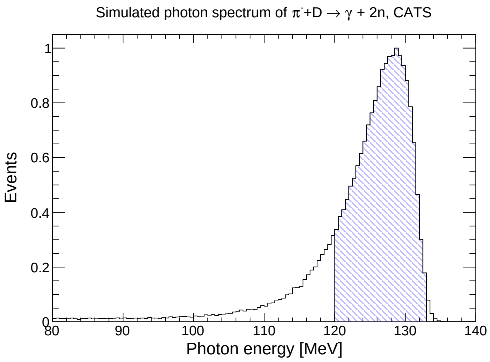

Figure 5.12: The simulated spectrum of the photon energy of the reaction $\pi^- + {}^2\text{H} \to \gamma + 2\text{n}$ in CATS. The shaded blue area indicates the energy cut that defined the acceptance.

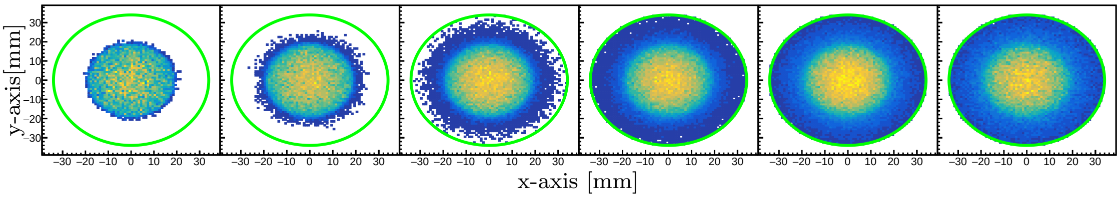
Capture locations in the x-y plane in the liquid deuterium

Figure 5.13: Capture locations in the x-y plane inside the liquid deuterium in different energy bins (energy bins 2 to 7 from left to right). The green circle indicates the radius of the target.

Reaction vertex positioning

The vertex locations of the Monte-Carlo photons were sampled from the energy dependent distributions of the π^- capture locations. The capture location distributions were determined as a part of the capture analysis discussed in Section 5.6 and are depicted in Figure 5.13. At lower incident photon energies the produced pions had low kinetic energies and their radial drift from the z-axis (beam direction) was small. At higher incident photon energies the pions travelled further inside the liquid deuterium and thus the captures occurred everywhere inside the target. However the acceptances revealed almost no dependence on the positioning of the vertices in the x-y plane.

In the experiment the vertex positions of the capture photons depended on the accuracy of the target positioning. The possible positioning errors are depicted in Figure 5.14. The accuracy of the target positioning along the direction of the photon beam (left in Figure 5.14) was $\sim$ 1 cm, which affected the acceptance by $\sim$ 1.5%. Optical lasers were used to align the target into the path of the photon beam in the X-Y plane. Due to this the rotational uncertainty (centre in Figure 5.14) was $\lesssim 2°$ and the target centre was aligned to the photon beam (right in Figure 5.14) with an accuracy of $\sim$ 2 mm. Both the rotational uncertainty and the uncertainty related to the positioning of the target to the photon beam were small and affected the acceptance by $\sim$ 0.2%.

Detector positioning

The positioning of the detectors in the experimental hall was determined with an accuracy of ±1 cm. As the detectors were at different distances from the target centre, the 1 cm uncertainty had a different effect on the acceptances of the different detectors. The uncertainty of the positioning of the detectors affected the acceptance of BUNI by $\sim$ 3%, the acceptance of CATS by $\sim$ 2% and the acceptance of DIANA by $\sim$ 1.5%.

Energy cut effect

The ±0.4 MeV uncertainty associated with the calibration corrections (see Section 3.9) propagated into the energy cut 120 − 133 MeV that determined the acceptance. The effect was quantified by determining the acceptance Ω^+_{eff} (Ω^-_{eff}) with the energy cut

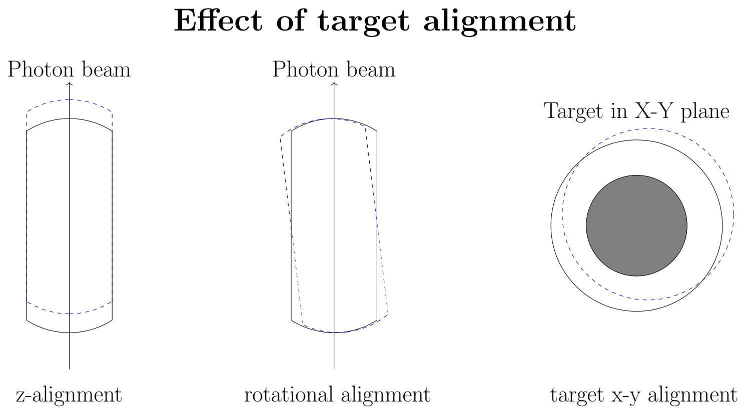

Figure 5.14: Illustration of the positioning uncertainties of the target. Left - positioning of the target along the path of the photon beam; centre - rotational alignment of the target; right - alignment of the target centre to the photon beam (gray fill).

$120.4 - 133.4$ MeV ($119.6 - 132.6$ MeV) and calculating

$$\sigma^{\pm} = \frac{\Omega_{\text{eff}}^{\pm} - \Omega_{\text{eff}}}{\Omega_{\text{eff}}}. \tag{5.12}$$

In Eq. (5.12) Ω_{eff} is the acceptance calculated with the energy cut $120 - 133$ MeV. The uncertainty determined by Eq. (5.12) varied slightly for different detectors with typical values $\sigma^{+(-)} \approx -(+)1.5\%$.

Cosmic cut effects

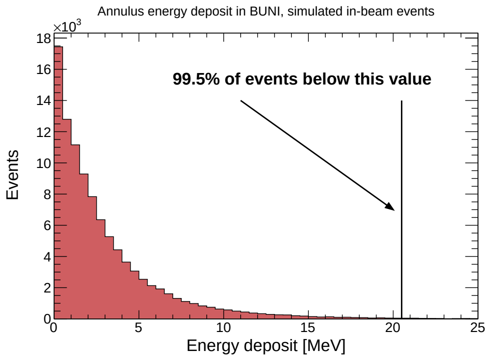

Figure 5.15: Energy deposit in the BUNI annulus in the simulated in-beam events, cf. Figure 3.22.

It was very important to take the cosmic cuts as discussed in Section 3.8 into account in the calculation of acceptances. To that end equivalent cosmic cuts were established for the simulated data as part of the simulation of the in-beam measurements (see Appendix A.3). Figure 5.15 depicts the simulated equivalent of Figure 3.22. Although the experimental data and the simulation used different units for the energy deposit in the annulus (sum of the ADC signals in the former, MeV in the latter), the cosmic cuts were equivalent as they were positioned relative to the distributions of the events. The cosmic cut had the largest effect on the acceptance of the BUNI detector, reducing it by $\sim 17\%$. The acceptance of CATS was reduced by $\sim 6\%$ and the acceptance of DIANA was reduced by $\sim 0.5\%$. This was expected, as the CATS detector had an inner collimator and the DIANA detector was significantly further from the target (see Figure 2.4), meaning that in both detectors the photons from the liquid deuterium typically entered the core crystal close to its centre. In DIANA the effect of the cosmic cut on the acceptance was further suppressed by the substantially larger diameter of the core crystal. The photons that entered the core crystal of BUNI were less constrained by the collimator and were more often misidentified as cosmic tracks.

Model dependence

The acceptance calculation depended on the selected model for the energy spectrum of the capture reaction. The model dependence was assigned an uncertainty of 5%. The model selection and the related uncertainty are discussed in detail in Appendix A.4.

Acceptances with statistical and systematic uncertainties

The positioning of the detectors was slightly different in the run period in April 2015 compared to the run periods in June and September 2011. Due to this the detector acceptances were slightly different. Table 5.6 provides the acceptances of the three detectors for the run periods in June and September 2011 and Table 5.7 for the run period in April 2015. The statistical and combined systematic uncertainties are indicated. Sufficient Monte-Carlo events were processed to reach statistical uncertainty $\sim 1\%$. The systematic uncertainty was typically $\sim 6\%$ and was dominated by the model dependence.

Detector acceptances, June/September 2011

Bin	BUNI Ω_{eff} [msr]	CATS Ω_{eff} [msr]	DIANA Ω_{eff} [msr]
3	$43.82 \pm 0.29 \pm 2.7$	$28.11 \pm 0.23 \pm 1.61$	$23.57 \pm 0.21 \pm 1.37$
4	$43.51 \pm 0.29 \pm 2.67$	$28.51 \pm 0.24 \pm 1.63$	$23.71 \pm 0.22 \pm 1.38$
5	$43.73 \pm 0.3 \pm 2.68$	$27.91 \pm 0.24 \pm 1.61$	$23.76 \pm 0.22 \pm 1.37$
6	$44.07 \pm 0.3 \pm 2.72$	$28.4 \pm 0.24 \pm 1.62$	$23.26 \pm 0.22 \pm 1.34$
7	$43.69 \pm 0.3 \pm 2.69$	$28.5 \pm 0.24 \pm 1.63$	$23.58 \pm 0.22 \pm 1.36$
8	$43.72 \pm 0.38 \pm 2.68$	$28.2 \pm 0.31 \pm 1.6$	$23.25 \pm 0.28 \pm 1.35$

Table 5.6: Acceptances of the three detectors in the run periods in June and September 2011. The first uncertainty is statistical, the second is systematic.

Detector acceptances, April 2015

Bin	BUNI Ω_{eff} [msr]	CATS Ω_{eff} [msr]	DIANA Ω_{eff} [msr]
3	$47.18 \pm 0.3 \pm 2.95$	$31.35 \pm 0.24 \pm 1.81$	$28.15 \pm 0.23 \pm 1.62$
4	$46.73 \pm 0.3 \pm 2.92$	$30.99 \pm 0.24 \pm 1.81$	$28.1 \pm 0.23 \pm 1.63$
5	$46.23 \pm 0.3 \pm 2.89$	$31.07 \pm 0.25 \pm 1.81$	$27.76 \pm 0.23 \pm 1.61$
6	$46.86 \pm 0.31 \pm 2.92$	$31.06 \pm 0.25 \pm 1.82$	$27.89 \pm 0.24 \pm 1.61$
7	$46.02 \pm 0.31 \pm 2.86$	$30.68 \pm 0.25 \pm 1.78$	$27.79 \pm 0.24 \pm 1.61$
8	$47.13 \pm 0.39 \pm 2.91$	$31.07 \pm 0.32 \pm 1.8$	$27.45 \pm 0.3 \pm 1.58$

Table 5.7: Acceptances of the three detectors in the run period in April 2015. The first uncertainty is statistical, the second is systematic.

5.4 Tagged photon flux

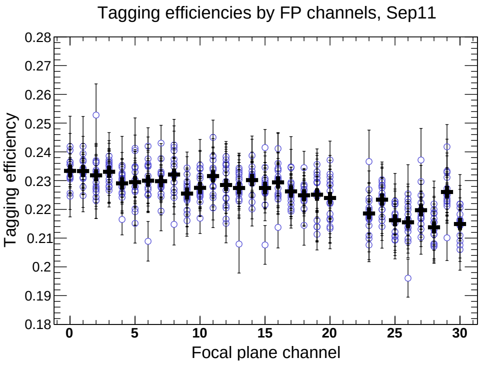

Figure 5.16: Tagging efficiency individual measurements (blue circles) and average (black crosses) in September 2011.

The integrated flux of tagged photons is the total number of tagged photons incident on the liquid deuterium target throughout the run period. The number of tagged Bremsstrahlung photons was counted through the number of hits in the focal plane detector. The resulting count had to be corrected by taking the tagging efficiency (see Section 2.2.2) into account. Tagging efficiency measurements were performed daily throughout the run periods. From each of the measurements a tagging efficiency value was calculated for every channel of the focal plane detector. Figure 5.16 depicts the results of the 15 individual tagging efficiency measurements for each channel of the FP detector that were performed during the run period in September 2011. The black crosses in Figure 5.16 indicate the averages over the fifteen measurements. For each channel the standard deviation over the measurements was calculated and interpreted as the systematic uncertainty.

The target was several meters downstream from the Lead-glass detector that was used for the tagging efficiency measurements. Thus the integrated flux had to be corrected for photons that converted to pairs ($\gamma \rightarrow e^+e^-$) along the path from the position of the Lead-glass to the target. The pair conversions occurred due to interactions in air, in the Hostaphan window (cf. Figure 2.3), in the upstream end cap of the Kapton vessel and in liquid deuterium. The correction was found by simulating 500k beam photons from the position of the Lead-glass detector towards the target and counting the photons that reached the downstream end cap of the Kapton vessel. The simulation revealed that 98.2% of the created photons reached the end cap and 1.8% converted to pairs.

Table 5.8 provides the integrated flux for each energy bin in the three run periods.

Integrated tagged photon flux by energy bins

Bin	April 2015	September 2011	June 2011
Bin 0	$(8.09 \pm 0.21) \cdot 10^{10}$	$(21.53 \pm 0.28) \cdot 10^{10}$	$(6.28 \pm 0.13) \cdot 10^{10}$
Bin 1	$(8.19 \pm 0.15) \cdot 10^{10}$	$(22.41 \pm 0.35) \cdot 10^{10}$	$(6.43 \pm 0.13) \cdot 10^{10}$
Bin 2	$(7.60 \pm 0.17) \cdot 10^{10}$	$(20.30 \pm 0.30) \cdot 10^{10}$	$(6.09 \pm 0.12) \cdot 10^{10}$
Bin 3	$(7.95 \pm 0.15) \cdot 10^{10}$	$(20.72 \pm 0.34) \cdot 10^{10}$	$(6.08 \pm 0.12) \cdot 10^{10}$
Bin 4	$(6.86 \pm 0.11) \cdot 10^{10}$	$(20.84 \pm 0.31) \cdot 10^{10}$	$(6.06 \pm 0.13) \cdot 10^{10}$
Bin 5	$(7.38 \pm 0.16) \cdot 10^{10}$	$(\ 9.37 \pm 0.24) \cdot 10^{10}$	$(2.81 \pm 0.08) \cdot 10^{10}$
Bin 6	$(6.96 \pm 0.10) \cdot 10^{10}$	$(19.06 \pm 0.30) \cdot 10^{10}$	$(5.68 \pm 0.13) \cdot 10^{10}$
Bin 7	$(5.45 \pm 0.13) \cdot 10^{10}$	$(13.15 \pm 0.22) \cdot 10^{10}$	$(4.07 \pm 0.10) \cdot 10^{10}$

Table 5.8: Tagged photon flux per energy bin in the three run periods.

The uncertainty originates from the spread of the results from the tagging efficiency measurements. The correction related to the pair conversion has been taken into account. The statistical uncertainties were negligible. In the run periods in June and September the count in energy bin 5 was somewhat lower than in the other energy bins. In that sector of the focal plane detector two channels were not counting properly and were therefore excluded from the analysis. This also explains the gap in Figure 5.16. More details on the tagging efficiency measurements are available in Ref. [119].

5.5 Effective target thickness

The effective target thickness was calculated according to the formula [71]

$$\kappa_{\text{eff}} = \frac{\rho L N_{\text{A}}}{A}. \tag{5.13}$$

In Eq. (5.13) ρ is the density of the liquid deuterium, L is the mean path length of the photons through the target, $N_{\text{A}} = 6.022 \cdot 10^{23}\,1/\text{mol}$ is the Avagadro constant and $A = 2.014\,\text{g/mol}$ is the molar mass. The mean path length of the photons through the target was determined from the Geant4 simulation. Beam photons were thrown from the location of the radiator and tracked through the liquid deuterium. The mean path length was found to be $L = (16.71 \pm 0.17)$ cm. The density of the liquid deuterium was monitored systematically throughout the run periods. The density was extremely stable and effectively constant at $\rho = 0.163\,\text{g/cm}^3$. Any boiling of the liquid deuterium would have been detected through the pressure fluctuations inside the target cell. As no pressure fluctuations were observed, it was concluded that target boiling did not occur. Combining the information, the effective target thickness was calculated to be

$$\kappa_{\text{eff}} = (8.14 \pm 0.10) \cdot 10^{23}\,\text{nuclei/cm}^2. \tag{5.14}$$

This is practically identical to the value reported in Ref. [71]. The experiment in Ref. [71] and this experiment used the same target, thus a similar value for κ_{eff} was expected.

5.6 Capture efficiency

As discussed in Section 2.3, one of the key pieces of information that had to be extracted from the simulation was the capture efficiency of negative pions inside the liquid deuterium target. Various aspects related to the extraction of the capture efficiencies are discussed in the paragraphs below.

Reliability of the simulation

First it is argued generally that the capture efficiencies determined from the simulation are trustworthy. The trajectories of the photoproduced pions in the liquid deuterium, which had kinetic energies up to ~ 20 MeV, were dominated by the well-understood electromagnetic interactions. Therefore there is little reason to doubt the predicted number of pions that exited the target. For the pions that did not exit the liquid deuterium the only alternative to capture was decay (see Section 2.3.1). The decay probability was determined by the accurately known mean lifetime of $2.6033 \pm 0.0005 \cdot 10^{-8}$ s [72]. In this perspective the number of captures could be expressed as

$$N_{\text{captures}} = N_{\text{throws}} - N_{\text{exits}} - N_{\text{decays}}. \tag{5.15}$$

In Eq. (5.15) N_{throws} is the number of simulated pions in the liquid deuterium, N_{exits} and N_{decays} are the predicted counts for the pions that exited the target and the pions that decayed. As one expects the latter two to be estimated accurately by the Geant4 software, the number of captures is also expected to be accurate.

Simulation

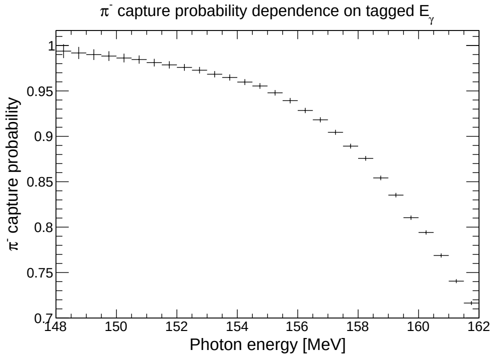

Figure 5.17: Dependence of the π^- capture efficiency on the energy of the tagged photon.

As of Geant4 version 4.10 the capture is simulated by the Bertini intranuclear cascade model and handled by the class `G4HadronicAbsorptionBertini` (see user's guide for application development [120]). The captures (N_{captures}) were identified through counting the simulated negative pions that had `hBertiniCaptureAtRest` as the last process inside the liquid deuterium. $N_{\text{throws}} = 5 \cdot 10^6$ negative pions were created inside the target. The X-Y coordinates of the vertices (π^- starting positions) were sampled from the intensity distribution of the photon beam (see Section A.2). The Z coordinates (along the direction of the beam) were distributed uniformly over the length of the liquid deuterium. In sampling the momenta of the pions the Fermi motion of the bound neutron in the deuteron, the energy of the incident photon and the $\cos\theta$ distribution of the pions in the reaction $\gamma + \mathrm{n} \to \pi^- + \mathrm{p}$ [40] were taken into account (see Appendix A.5). Figure 5.17 depicts the dependence of the capture efficiency on the energy of the incident photon. The capture efficiency was determined as

$$P_c^{\text{bin i}} = \frac{N_{\text{captures}}^{\text{bin i}}}{N_{\text{throws}}^{\text{bin i}}}. \tag{5.16}$$

In Eq. (5.16) $N_{\text{throws}}^{\text{bin i}}$ is the number of Monte-Carlo pions that were created by Bremsstrahlung photons with energies corresponding to energy bin i. $N_{\text{captures}}^{\text{bin i}}$ is the number of captured pions and $P_c^{\text{bin i}}$ is the capture efficiency. Several different Geant4 physics lists were employed to perform the capture analysis and no significant discrepancies between the resulting capture efficiencies were observed.

Beam radius

As explained above, the vertex coordinates in the X-Y plane were sampled from the simulated intensity distribution of the photon beam depicted in Figure A.4. The radius

Systematic uncertainties in the capture efficiency

Bin	sys. err. (%)	*Beam. R. [%]*	*Align. [%]*	*Model [%]*	ΔE_γ *[%]*
Bin 2	3.0	0.0	0.0	3	0.2
Bin 3	3.0	0.0	0.1	3	0.2
Bin 4	3.0	0.3	0.1	3	0.2
Bin 5	3.1	0.4	0.4	3	0.4
Bin 6	3.5	1.2	0.5	3	1.1
Bin 7	4.7	1.6	0.9	3	3.1

Table 5.9: Sources of systematic uncertainty in the capture efficiency. The column sys. err. provides the combined systematic uncertainty. Other columns detail the various sources that contributed to the combined uncertainty. *Beam. R.* - radius of the photon beam; *Align.* - positioning of the target; *Model* - model dependence; ΔE_γ - uncertainty of the photon energy.

of the beam spot was varied by ±2 mm ($\sim$ 10%) in the simulation to assess the uncertainty that could have propagated from the simulation of the beam profile to the simulation of the π^- capture efficiencies. The radius of the beam affected the capture efficiencies only in the higher energy bins (see column *Beam R.* in Table 5.9). This is expected, as at lower energies of the incident photons the radial drift of the pions from the z-axis is small (see Figure 5.13), which suppresses the dependence of the capture efficiencies on the radius of the beam spot.

Target alignment

The uncertainties related to the positioning of the target are depicted in Figure 5.14. The positioning of the target along the direction of the beam (left in Figure 5.14) did not affect the capture efficiencies, but the rotational alignment and the centering of the target into the photon beam (middle and right in Figure 5.14, respectively) had to be investigated. The simulation revealed that the combined uncertainty related to the positioning of the target was typically ~1% in the higher energy bins (see column *Align.* in Table 5.9). The effect was small because the positioning of the target in the X-Y plane was performed with the help of optical lasers and was relatively accurate.

Model dependence

A 3% uncertainty due to model dependence was assigned to the extracted capture efficiencies. There are currently no known alternatives to the performed capture analysis and thus it is difficult to provide a well-motivated estimate for the model uncertainty. It was discussed above that capture inside the liquid deuterium is the only alternative to the decay and to the exit from the target volume. As these processes are expected to be modelled accurately by Geant4 the 3% uncertainty is considered to be realistic.

Uncertainty of the photon energies

The ±0.4 MeV uncertainty of the tagged photon energies that originated from the calibration corrections (see Section 3.9) propagated into the capture efficiency analysis.

Capture efficiencies with statistical and systematic uncertainties

Bin	En. [MeV]	P_c	Stat. err.	Sys. err.
Bin 2	147.0	0.999	0.009 (0.9%)	0.030 (3.0%)
Bin 3	149.7	0.988	0.008 (0.8%)	0.030 (3.0%)
Bin 4	152.3	0.975	0.006 (0.6%)	0.029 (3.0%)
Bin 5	154.9	0.952	0.004 (0.4%)	0.030 (3.1%)
Bin 6	157.6	0.892	0.004 (0.5%)	0.031 (3.5%)
Bin 7	159.8	0.816	0.004 (0.5%)	0.038 (4.7%)

Table 5.10: Capture efficiencies by energy bins with statistical and combined systematic uncertainties.

This was addressed by determining the capture efficiency $P_c^{+(-)}$ for each energy bin with the photon energy shifted by +(−)0.4 MeV and calculating the relative difference

$$\sigma^{+(-)} = \frac{P_c^{+(-)} - P_c}{P_c}. \tag{5.17}$$

In Eq. (5.17) P_c is the capture efficiency with the unshifted photon energy as provided in Table 5.10. The uncertainty as given by Eq. (5.17) was asymmetrical, the higher value is reported in Table 5.9 in the column ΔE_γ.

Extracted capture efficiencies

Table 5.10 provides the capture efficiency for each energy bin above the π^- photoproduction threshold[3]. The capture efficiency was close to unity near threshold and started dropping more rapidly above $\sim$ 157 MeV (see Figure 5.17). Sufficient Monte Carlo events were processed to reach statistical uncertainty $\lesssim$ 1%. The various contributions to the combined systematic uncertainty are detailed in Table 5.9.

5.7 Results and discussion

The information provided in the previous sections was combined to calculate the cross-section for π^- photoproduction on the deuteron.

Comparison of nine measurements

As was mentioned at the beginning of this chapter, with three run periods and three detectors a total of nine independent measurements for the cross-section were performed. Figure 5.18 depicts the nine measurements in six graphs. Each graph in the left column has the extracted cross-sections for the three detectors in a specific run period. Additionally, the black crosses display the average of the nine measurements in each plot. The statistical uncertainties are shown, no uncertainty is displayed for

---

[3] Note that the capture efficiencies in Table 4.1 and Table 5.10 are slightly different. In Table 5.10 the capture efficiency per energy bin was calculated as a flux-weighed average of capture efficiencies corresponding to the four focal plane channels that were combined to form the energy bin. In Table 4.1 the flux has not been taken into account.

the average. The results from the three detectors were in excellent agreement in the April 2015 data. Similar consistency was observed in the lower energy bins in the June 2011 data, but in the higher energy bins the DIANA detector gave higher values of the cross-section. In the September 2011 data the results from DIANA were somewhat higher in all energy bins except for the last bin. Sorting the nine measurements by detectors was another useful way of visualising the data. In Figure 5.18 each graph in the right column depicts the cross-section measurements by a single detector in different run periods. The black crosses indicate the average of the nine measurements. Generally the agreement between the April 2015 and June 2011 data was relatively good in BUNI and CATS, the results from the September 2011 data were slightly higher. A more pronounced variation was observed in the DIANA detector.

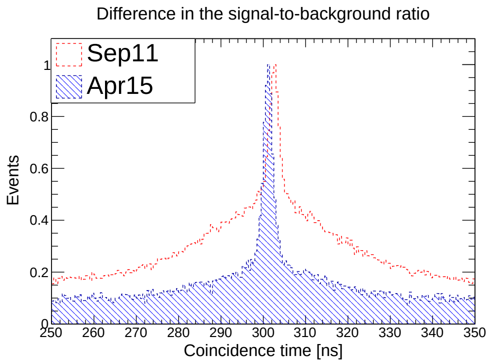

Figure 5.19: Coincidence spectra in the CATS detector in April 2015 and September 2011 run periods.

It is not clear what might have caused the systematically higher results in the September 2011 run period, especially in the DIANA detector. One possible cause is the imperfect subtraction of the random background. The intensity of the photon beam was significantly higher in the September 2011 run period, causing a less favourable signal-to-background ratio as compared to the June 2011 and April 2015 run periods. Figure 5.19 depicts the normalised coincidence spectra over all energy bins in CATS in the run periods in April 2015 and September 2011. The less favourable signal-to-background ratio may have had an effect on the yield extraction from the fits. However at this point there is no clear method to test the validity of this assumption.

Combining the measurements

Despite efforts the cause of the spread of the measurements could not be identified and therefore any exclusion of the outlying data points could not be justified. The results from the nine measurements were combined to calculate the average cross-sections and the spread of the measurements was included in the systematic uncertainty (see next paragraph). To that end the quantity

$$\zeta(E) = \frac{Y(E)}{\Omega_{\text{eff}} \cdot N_\gamma(E)} \tag{5.18}$$

(cf. Eq. (5.1)) was calculated for each detector and run period, resulting in nine $\zeta(E)$ values per energy bin. The spread of the measurements was caused by the spread in $\zeta(E)$ - in a perfect experiment there would have been no statistically significant difference between the nine $\zeta(E)$ values. The mean and the standard deviation of $\zeta(E)$

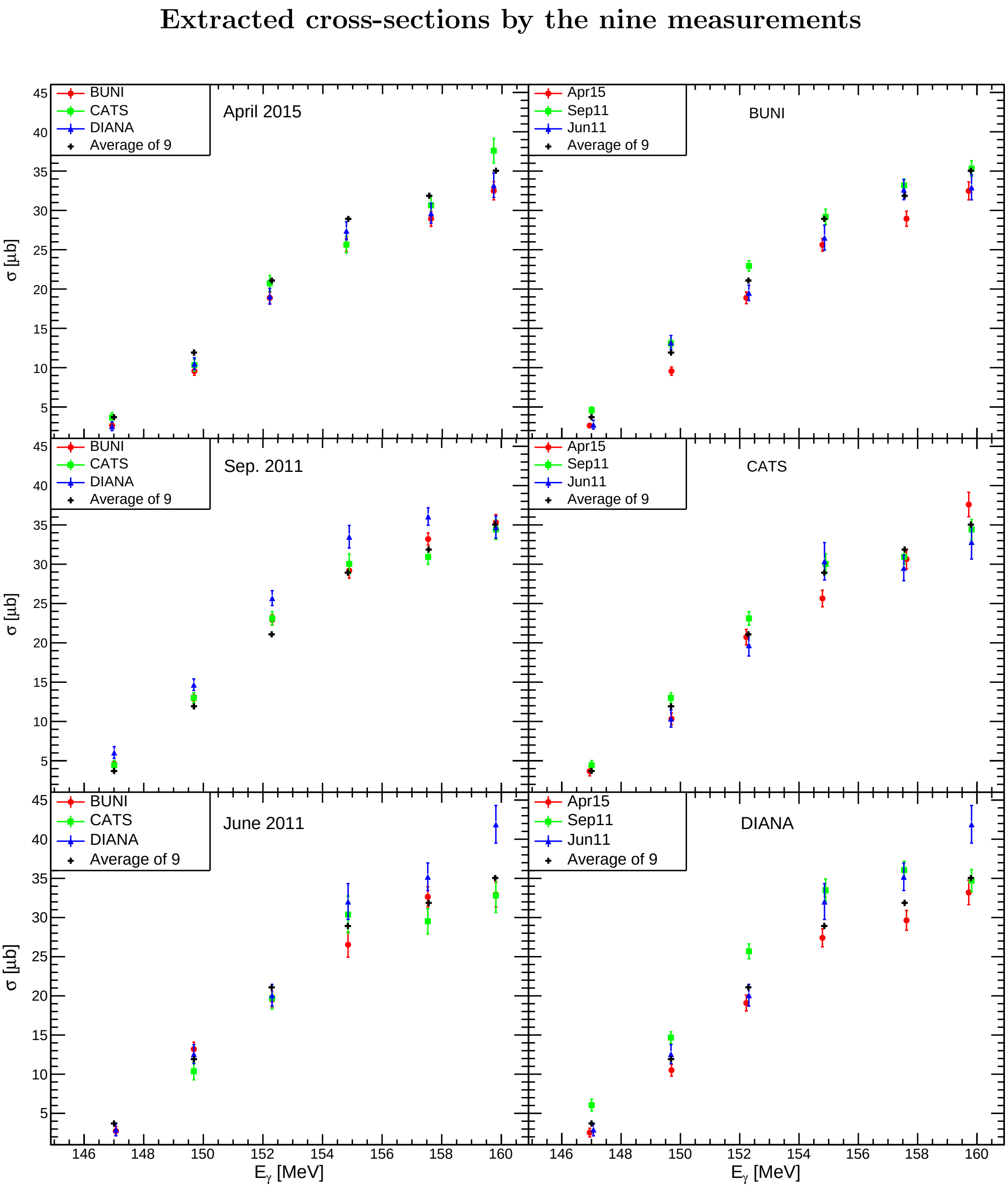
Extracted cross-sections by the nine measurements

Figure 5.18: Measured cross-sections of $\gamma + {}^2\mathrm{H} \rightarrow \pi^- + 2\mathrm{p}$ by the three detectors in three run periods. The graphs in the left column compare the measurements by the three detectors in different run periods. The graphs in the right column compare the measurements by the same detector in different run periods. Additionally the average of the nine measurements (three detectors times three run periods) is indicated in each graph by the black crosses.

were calculated as

$$\bar{\zeta}(E) = \sum_{\mathrm{m}=1}^{9} \frac{\zeta_{\mathrm{m}}(E)}{9}, \tag{5.19}$$

$$\sigma'_{\bar{\zeta}}(E) = \sqrt{\sum_{\mathrm{m}=1}^{9} \frac{\left[\zeta_{\mathrm{m}}(E) - \bar{\zeta}(E)\right]^2}{8}}. \tag{5.20}$$

The mean of Eq. (5.19) was combined with the rest of Eq. (5.1) to calculate the average cross-section from the nine measurements for each energy bin. The average cross-sections are reported in Table 5.11 in the column σ.

Systematic uncertainty

Firstly, the contamination of the yields by the scattering backgrounds (see Table 5.5) contributed to the spread of the results, as the contamination was different in each detector. Secondly, except for the model dependence all of the systematic uncertainties associated with the detector acceptances contributed to the spread. The detectors and the target had to be positioned for each run period, meaning that the error introduced by the placement of the target varied between run periods and the error introduced by the placement of the detectors varied between the run periods and the detectors. As was mentioned in Section 5.3, the uncertainty due to the energy cut was also moderately different in each detector. Thirdly, the tagging efficiencies, which dominated the uncertainty of the tagged photon fluxes (see Section 5.4), may have contributed to the spread of the results from different run periods. From the above discussion it was concluded that the standard deviation given by Eq. (5.20) was the best estimate for the systematic uncertainty associated with the combination of the yield, the acceptance and the flux (Eq. (5.18)). Additionally it accounted for "hidden" sources of systematic uncertainty that were not addressed in the analysis.

The standard deviation of Eq. (5.20) was combined with the uncertainty of the Kapton background (1.5%) and the model dependence of the solid angle calculation (5%), as these sources of uncertainty had an identical effect on the cross-sections measured by the three detectors in different run periods. The full systematic uncertainty of $\zeta(E)$ was calculated as

$$\sigma_{\bar{\zeta}}(E) = \sqrt{\sigma'_{\bar{\zeta}}(E)^2 + (0.015^2 + 0.05^2) \cdot \bar{\zeta}(E)^2}. \tag{5.21}$$

Finally the systematic uncertainty of the capture efficiency (see Table 5.10), the effective target thickness (see Eq. (5.14)) and the branching ratio (see after Eq. (5.1)) were included to calculate the combined systematic uncertainties of the extracted cross-section points.

Final results

Table 5.11 provides the final results of the analysis. The combination of the nine measurements had low statistical uncertainty in every energy bin and the systematic uncertainty dominated. The systematic uncertainty was dominated by the spread of the results from different detectors and run periods.

Extracted cross-section for π^- photoproduction

Bin	En. [MeV]	σ [µb]	Stat. err.	Sys. err.
Bin 2	147.0	3.7	0.2 (5.4%)	1.3 (35.1%)
Bin 3	149.7	11.9	0.3 (2.5%)	1.9 (16.0%)
Bin 4	152.3	21.1	0.4 (1.9%)	2.7 (12.8%)
Bin 5	154.9	28.9	0.5 (1.7%)	3.4 (11.8%)
Bin 6	157.6	31.9	0.4 (1.3%)	3.3 (10.3%)
Bin 7	159.8	35.0	0.6 (1.7%)	4.0 (11.4%)

Table 5.11: Measured cross-section points of π^- photoproduction on the deuteron.

Discussion

Figure 5.20 displays the data of Table 5.11. The statistical uncertainties are indicated with error bars, the systematic uncertainties by the blue boxes. The uncertainty of the photon energies was ±0.4 MeV and originated from the calibration corrections discussed in Section 3.9.

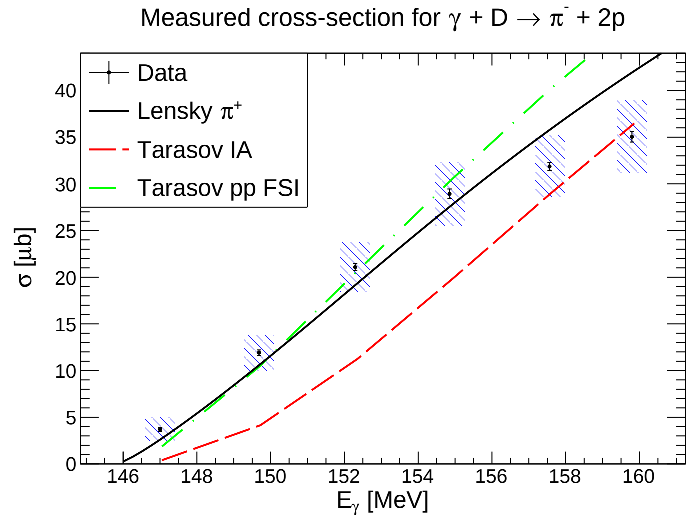

Figure 5.20: The measured cross-section for $\gamma + {}^2\mathrm{H} \rightarrow \pi^- + 2\mathrm{p}$. The statistical uncertainties are indicated with error bars, the systematic uncertainties by the blue boxes. The uncertainty of the photon energy was ±0.4 MeV (see Section 3.9). Theoretical predictions: Lensky [44, 45]; Tarasov [43, 121].

The data was compared to theoretical models. The solid black line is a ChPT based lowest order prediction for the other isospin channel, $\gamma + {}^2\mathrm{H} \rightarrow \pi^+ + 2\mathrm{n}$, by Lensky *et. al.* [44, 45]. From the theoretical viewpoint at the lowest order the elementary photoproduction amplitudes $\gamma\mathrm{p} \rightarrow \pi^+\mathrm{n}$ and $\gamma\mathrm{n} \rightarrow \pi^-\mathrm{p}$ are equal and are determined by the Kroll-Ruderman term. The data points and the theoretical prediction are in good agreement in the lower energy bins and diverge slightly at the two higher energy bins. However, the reaction $\gamma + {}^2\mathrm{H} \rightarrow \pi^- + 2\mathrm{p}$ has three charged particles in the final state and the pion-proton and proton-proton Coulomb interactions are expected to have an effect on the cross-section. Work is in progress to include the proton-proton FSI into the ChPT prediction [45].

Two other preliminary predictions by Tarasov *et. al.* [43, 121] are also displayed. The impulse approximation (denoted *IA*) excludes all final-state interactions and clearly under-predicts the cross-section at low photon energy. The second model by Tarasov includes the final state interactions of the proton-proton system. In the four lowest energy bins the FSI model from by Tarasov *et. al.* and the lowest order ChPT model by Lensky *et. al.* are relatively similar and in agreement with the data points. The models diverge from experimental data and from each other at higher energies.

It is important to note that the model selection for the energy spectrum of the capture reaction $\pi^- + {}^2\mathrm{H} \to \gamma + 2\mathrm{n}$ (see Section 5.3 and Appendix A.4) affects all of the measured cross-section points identically. If the discrepancy between the theoretical models and the experimental data in the higher energy bins remains after the former have been improved, it could not be due to the model of the capture reaction.

In summary the first measurement of the π^- photoproduction on the deuteron in the threshold region has been performed. Both the statistical and the systematic uncertainties have been evaluated. In the lower energy bins the data are in good agreement with the models that include the FSI. In the higher energy bins the models and the data diverge. It is also worth pointing out that the analysis of Ref. [43] offers a framework to extract the elementary amplitude $\gamma\mathrm{n} \to \pi^-\mathrm{p}$ from the present measurement. The latter could serve as a comparison and input to the MAID and SAID analyses (see Section 1.1.4 and 1.1.5).

Chapter 6

Compton signal extraction

The differential cross-section for Compton scattering was calculated according to

$$\frac{d\sigma(E)}{d\Omega} = \frac{Y(E)}{\Omega_{\text{eff}}(E) \cdot N_\gamma(E) \cdot \kappa_{\text{eff}}}. \tag{6.1}$$

In Eq. (6.1) $Y(E)$ is the yield of Compton scattered photons, $\Omega_{\text{eff}}(E)$ is the detector acceptance, $N_\gamma(E)$ is the tagged photon flux and κ_{eff} is the effective target thickness (in 1/cm^2). The flux and the effective target thickness were determined as part of the π^- analysis in Sections 5.4 and 5.5, respectively.

There are some differences between the pion and the Compton analyses. In the Compton analysis the differential cross-section was measured, meaning that the results from different detectors will not be equal, but the measurements by the same detector in different run periods still serve as consistency checks. In the pion analysis the yield was determined through a secondary reaction (subsequent capture of the produced pions), which introduced the branching ratio and the capture efficiency to Eq. (5.1) and the model dependence to the acceptance (see Section 5.3 and Appendix A.4). The Compton analysis was in principle simpler, as the yields were determined through the primary reaction of elastic scattering. However the low count of Compton events, high background rates and the modelling of the random background complicated the extraction of the cross-sections.

This chapter provides an overview of the analysis of the Compton measurement. Section 6.1 specifies the binning and the energy cut. Determination of the yields is discussed in Section 6.2. Two methods to model the random background are presented, one of which proposes a non-trivial way of estimating the shape of the background with `TSpectrum` software [122]. Section 6.3 reviews the calculation of the acceptances. The chapter is concluded with a summary of the results and discussion in Section 6.4.

6.1 Binning and energy cuts

The Compton signal was extracted from the dataset of skimmed events (see Section 4.1). Due to the low count of Compton events the 31 FP channels were binned in groups of eight, resulting in 4 energy bins for the incident photons, each ~ 5 MeV wide. The energy dependence of the cross-section is expected to be smooth and relatively modest in magnitude (see the experimental data below the pion threshold [71]),

Binned tagged photon energies

Bin	Energy [MeV]	Sys. err. [MeV]
Bin 0	143.2	0.4
Bin 1	148.4	0.4
Bin 2	153.2	0.4
Bin 3	158.5	0.4

Table 6.1: Tagged (incident) photon energies.

which justifies the use of wide energy bins. The average energies corresponding to the four bins are provided in Table 6.1.

The background analysis of Section 4.4 revealed that the inelastic channel could be suppressed by demanding $\mathrm{E}_{\mathrm{miss}} \geq -2$ MeV. The cut on the missing energy (Eq. (4.1)) was set to [-2 MeV, 3 MeV] and the timing coincidence spectra of the four energy bins were filled. Coincidence spectra in the CATS detector in the September 2011 run period are depicted in Figure 6.1. The energy cut suppressed the contamination from the inelastic scattering, meaning that the counts in the coincidence peaks in Figure 6.1 originated dominantly from the Compton scattering events. This allowed determination of the yields directly from the fits to the coincidence spectra. The photons from pion capture made it impossible to extract the Compton signal in bins 0 and 1 in BUNI and in bins $0-2$ in DIANA. Additionally, the solid angle acceptance of the DIANA detector was the smallest, as it was considerably further from the target compared to BUNI and CATS. Due to this the complications related to the high background rates and the low count of Compton events were the most severe in DIANA. This led to a lack of convergence of the fits and to inconsistent results for the Compton cross-sections in energy bin 3 from events triggered by the DIANA detector and thus the measurements are not presented.

6.2 Yield

Similarly to the pion analysis, the yield extraction relied on the fits to the timing coincidence spectra. The analysis was performed with the RooFit [113] package of the ROOT software [114]. Various aspects related to the the yield extraction procedure are discussed below.

6.2.1 The fit model

To perform the fits a model was necessary for the coincidence peak and the random (untagged) background. As in the pion analysis, the signal peak was represented by a Gaussian. However, a different approach was necessary to model the random background. Recall that in the pion analysis the shape of the random background was extracted from sub-threshold data (see Section 5.2.1). This was impossible in the Compton analysis, as the Compton signal was present in each energy bin. The background shape used in the pion analysis could not be applied to the Compton analysis, as it contained a portion of the Compton coincidences that are extracted

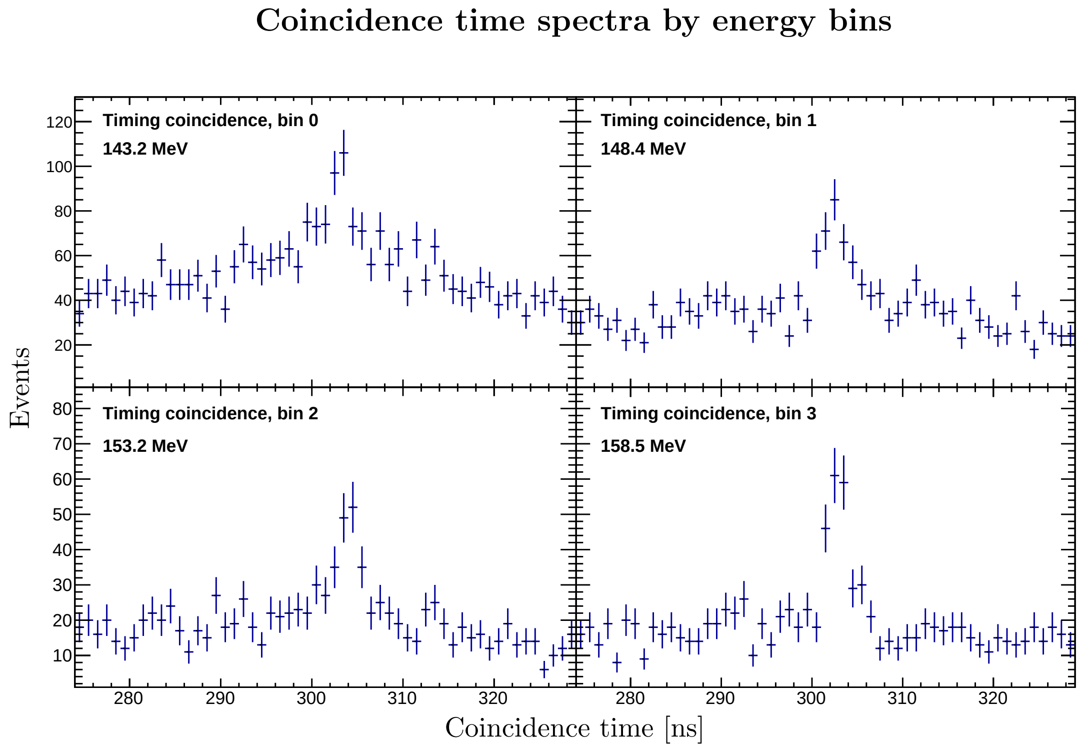

Figure 6.1: Coincidence time spectra in the CATS detector in four incident photon energy bins, September 2011 run period. 1 ns bin width was used for the coincidence spectra throughout the Compton analysis.

here.

Two different approaches to model the background are discussed, which resulted in two different fit models and ultimately in two $\mathrm{d}\sigma/\mathrm{d}\Omega$ values for each detector and energy bin in every run period. Modelling the random background is one of the key features of the Compton analysis and comparison of the results obtained with the two models is shown in Section 6.4.

Polynomial background

In the first instance the background was represented by a polynomial. The relatively low count of events in separate energy bins complicated the fitting procedure, causing the fits to the coincidence spectra not to converge when the parameters of the polynomial and the parameters of the coincidence peak were allowed to vary simultaneously. This problem was circumvented by fixing the coefficients of the polynomial from a fit to the coincidence spectrum with events over the full range of the FP detector (sum of the four histograms in Figure 6.1). From here onward the sum of the four histograms in Figure 6.1 is referred to as unbinned data, the four histograms separately are referred to as binned data.

Note that the time structure of the random background is not expected to depend significantly on the tagged photon energy. As was discussed in Section 4.2 the time structure of the random background was caused by the intensity fluctuations of the electron beam, not by the tagging system. Therefore the time structure of the random background was similar in each FP energy bin, which justified fixing the shape of the random background from unbinned data.

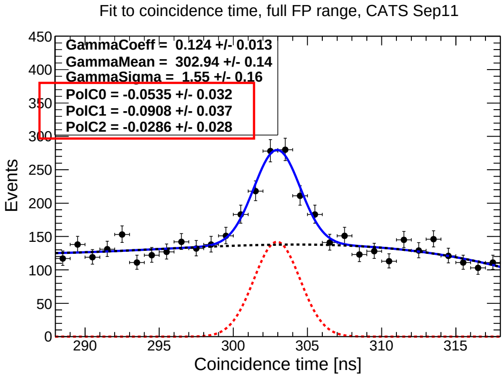

Figure 6.2: Determination of the coefficients of the polynomial background. The red box indicates the parameters that were fixed as a result of the fit.

An example fit to the unbinned data is depicted in Figure 6.2, where the parameters highlighted in the red box were used to fix the coefficients of the polynomial background that was used in fitting the binned data. Thus when the binned data were fitted the only free parameters were the mean and width (σ) of the coincidence peak and the signal-to-background ratio, which determined the scaling of the fixed polynomial shape. The random background in the run periods June and September 2011 was modelled better by a third degree polynomial. In these run periods the random background had a more complex shape (cf. Figure 5.19) and a second degree polynomial typically resulted in a higher χ^2 per degrees of freedom. On the other hand the background shape in April 2015 was flatter and a second degree polynomial provided a good representation, whereas fits with a third degree polynomial tended not to converge. After the coefficients of the polynomial were determined from the fit to the unbinned data, a fit model consisting of the coincidence peak and the polynomial background shape was constructed to fit the binned data as described in Section 6.2.2. The fit model consisting of the Gaussian for the coincidence peak and the polynomial background shape is referred to as the *polynomial model.*

TSpectrum background

Alternatively, the shape of the random background was determined by using the class `TSpectrum` [122] of the ROOT software. The `TSpectrum` software was originally developed for the separation of the background from the spectral lines in γ-ray spectroscopy, but can be used more generally to estimate the shape of a background below a narrow peak.

The `TSpectrum` software estimates the background with the Sensitive Nonlinear Iterative Peak (SNIP) clipping algorithm [123, 124]. The procedure is as follows. Let $c(i)$ be the count in bin i of the histogram. To determine the new value of the counts in bin i the average $[c(i-1)+c(i+1)]/2$ is calculated. If the original $c(i)$ is smaller than the average the bin content remains unchanged, otherwise the average becomes the new bin content. As a result the flat regions of the spectrum are not strongly affected, but the peaks are lowered ("clipped"). This procedure can be repeated numerous times and with each iteration the peaks become flatter. Choosing the correct number of iterations is up to the user and not completely trivial. The spectrum that is obtained as a result of the iterations is returned as the estimated background shape.

In the `TSpectrum` class the number of iterations is determined by the parameter `numberIterations`. The background was extracted from the coincidence spectrum of the unbinned data. Figure 6.3 displays the dependence of the extracted background shape on the parameter `numberIterations`. At too low parameter value the estimated background cut into the coincidence peak, at too high parameter value the background became too flat.

`TSpectrum` background dependence on parameter `numberIterations`

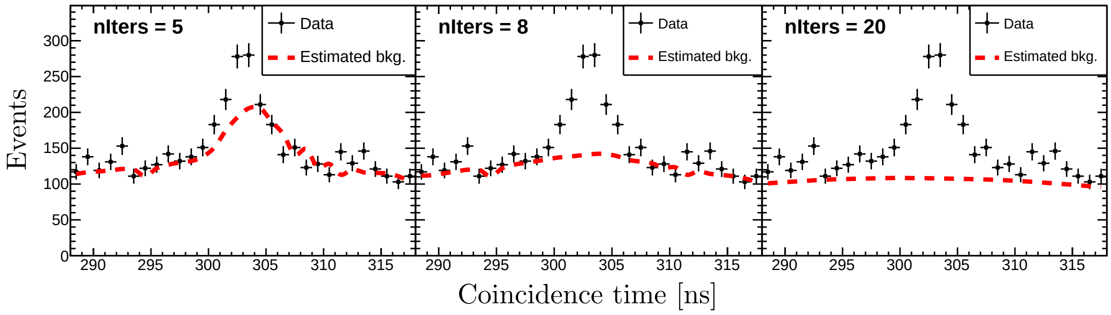

Figure 6.3: Dependence of the estimated background shape on the parameter `numberIterations`. The black data points represent the time spectrum over the full FP range for events triggered by CATS, September 2011.

Selecting the best `TSpectrum` background estimate

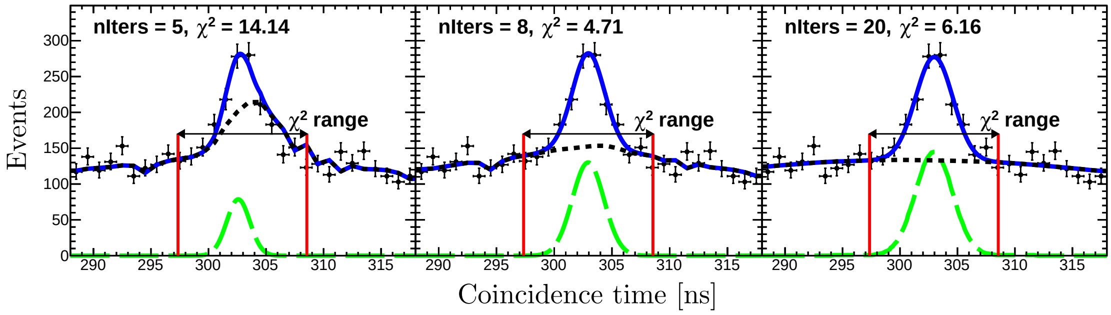

Figure 6.4: Determination of the best `TSpectrum` background estimation. The black data points represent the coincidence spectrum over the full FP range in CATS, September 2011. The short-dashed black line is the estimated background model (cf. Figure 6.3), the long-dashed green line is the Gaussian of the coincidence peak and the solid blue line is the fit result. The vertical red lines indicate the fixed region where the χ^2 was calculated.

To select the optimal representation of the background, several background shapes over a range of values of the parameter `numberIterations` were extracted. Each extracted shape was combined with a Gaussian to fit the unbinned data from which the background was extracted. These fits were separate from the fits to the binned data for the yield extraction as discussed in Section 6.2.2. Fits to the unbinned data using the three different background shapes displayed in Figure 6.3 are depicted in Figure 6.4. For each fit a χ^2 value between the model (blue line in Figure 6.4) and the unbinned data (black data points in Figure 6.4) was calculated in a fixed range centred at the coincidence peak. The dependence of the χ^2 value on the parameter `numberIterations` is depicted in Figure 6.5. The background shape which, combined with the Gaussian for the coincidences, resulted in the lowest χ^2 value was interpreted as the best representation of the background shape.

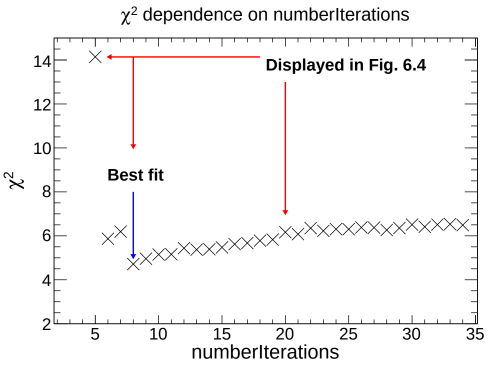

Figure 6.5: χ^2 dependence on the parameter `numberIterations`. Each parameter value corresponds to a different estimate of the background shape (cf. Figure 6.3).

Estimation of the shape of the random background with the `TSpectrum` software as described here relies on the χ^2 dependence in Figure 6.5 having a minimum. The various background shapes generated with `TSpectrum` as illustrated in Figure 6.3 can be considered as competing models for representation of the background. As described above and illustrated in Figure 6.4, the best model was selected by combining the competing shapes with a Gaussian for the coincidences and fitting the unbinned data. If the χ^2 dependence in Figure 6.5 did not have a minimum it would have been impossible to determine which of the competing shapes was the best representation for the random background.

The important difference between the `TSpectrum` model and the polynomial model of the previous paragraph is the behaviour of the background below the coincidence peak. Comparison of Figure 6.2 and Figure 6.3 illustrates the difference. The polynomial is close to flat below the coincidence peak, whereas the `TSpectrum` background can assume a more complex shape. This makes a difference when the count of signal events is low compared to the count of background events.

Finally the selected background shape (middle plot in Figure 6.3 in this example) was combined with a Gaussian for the coincidence peak to fit the binned data as outlined in Section 6.2.2. The fit model consisting of the Gaussian and the background from `TSpectrum` is referred to as *`TSpectrum` model*.

6.2.2 Determination of the yield values

Fitting procedure

Once a fit model was selected, the two-step fitting procedure as outlined in Section 5.2.3 was followed. First the coincidence spectrum in each energy bin was fitted using Maximum Likelihood (ML) estimation. In the ML estimation the mean and the sigma of the coincidence peak and the signal-to-background ratio were free parameters. As a result of the ML fit the mean and the width (σ) of the coincidence peak were fixed and two new parameters - the signal and background yield - were introduced to perform Extended Maximum Likelihood (EML) fits. As a result of the EML fit the signal yield and the background yield in the given energy bin were output by the minimiser with the associated statistical uncertainties.

Example fits to the coincidence spectra with different background shapes

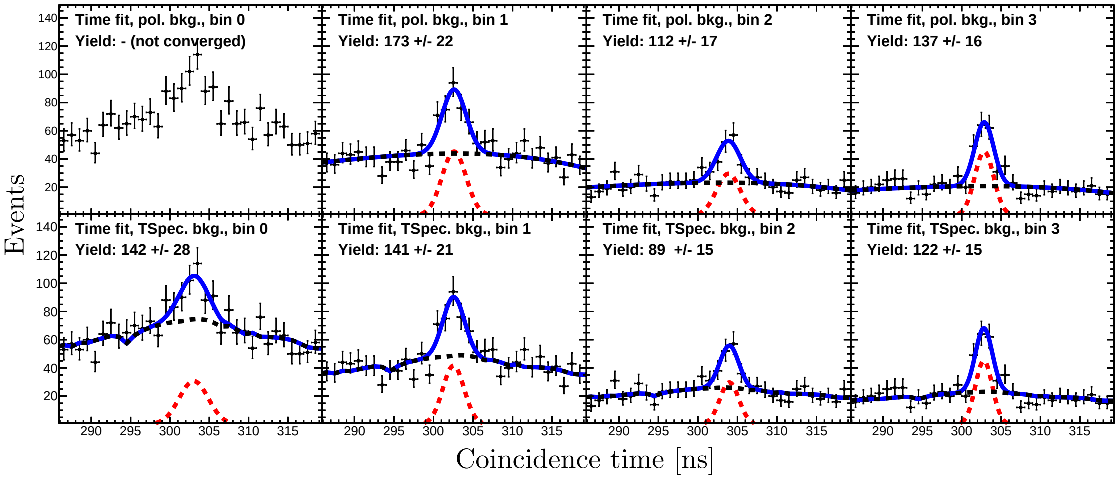

Figure 6.6: Fits to the coincidence spectra in four energy bins, CATS September 2011 data. The upper row displays the fits using the polynomial model, the lower row displays the fits using the `TSpectrum` model. The fit with the polynomial model to the spectrum in lowest energy bin failed to converge.

Extraction of the yields

The yields were sensitive to the range over which the fit was performed. As in the pion analysis, this was addressed by performing the fit to each coincidence spectrum in four different ranges and calculating the average yield from the four fits (see Section 5.2.3 and Figure 5.8). The sensitivity of the yield to the fit range was different in the three run periods. For example the sensitivity of the April 2015 yields was typically $\sim 2\%$, but the sensitivity of the September 2011 yields was $\sim 10\%$. This is related to the high count of background events in the September 2011 data. Changing the fit range affected the estimation of the background shape, which in turn propagated to the extracted yield values.

The coincidence spectra were fitted and the yields were extracted with both fit models described in Section 6.2.1. Figure 6.6 displays example fits to the four coincidence spectra in different energy bins for CATS, September 2011 data. The spectra in the upper row have been fitted using the polynomial model, the spectra in the lower row using the the `TSpectrum` model. In the lowest energy bin the fit to the September 2011 data failed to converge with the polynomial model. Tables 6.2 and 6.4 provide the yields extracted with the polynomial model, Tables 6.3 and 6.5 provide the yields extracted with the `TSpectrum` model. The selection of the fit model and the associated yields is returned to in Section 6.4, where the measurements from different run periods are combined.

Yields in BUNI in three run periods, polynomial model

Bin	En. [MeV]	Yield Apr. 2015	Yield Sep. 2011	Yield Jun. 2011
Bin 2	153.2	70 ± 10 (14.3%)	247 ± 23 (9.3%)	59 ± 10 (16.9%)
Bin 3	158.5	65 ± 10 (15.4%)	204 ± 19 (9.3%)	75 ± 10 (13.3%)

Table 6.2: Yields in the BUNI detector in three run periods, polynomial model.

Yields in BUNI in three run periods, `TSpectrum` model

Bin	En. [MeV]	Yield Apr. 2015	Yield Sep. 2011	Yield Jun. 2011
Bin 2	153.2	61 ± 10 (16.4%)	221 ± 22 (10.0%)	55 ± 10 (18.2%)
Bin 3	158.5	54 ± 9 (16.7%)	189 ± 19 (10.1%)	73 ± 10 (13.7%)

Table 6.3: Yields in the BUNI detector in three run periods, `TSpectrum` model.

Yields in CATS in three run periods, polynomial model

Bin	En. [MeV]	Yield Apr. 2015	Yield Sep. 2011	Yield Jun. 2011
Bin 0	143.2	31 ± 9 (29.0%)	-	25 ± 7 (28.0%)
Bin 1	148.4	38 ± 8 (21.1%)	170 ± 21 (12.4%)	39 ± 9 (23.1%)
Bin 2	153.2	45 ± 8 (17.8%)	109 ± 16 (14.7%)	15 ± 6 (40.0%)
Bin 3	158.5	53 ± 9 (17.0%)	134 ± 15 (11.2%)	36 ± 8 (22.2%)

Table 6.4: Yields in the CATS detector in three run periods, polynomial model.

Yields in CATS in three run periods, `TSpectrum` model

Bin	En. [MeV]	Yield Apr. 2015	Yield Sep. 2011	Yield Jun. 2011
Bin 0	143.2	30 ± 9 (30.0%)	135 ± 26 (19.3%)	21 ± 7 (33.3%)
Bin 1	148.4	37 ± 8 (21.6%)	151 ± 21 (13.9%)	33 ± 8 (24.2%)
Bin 2	153.2	45 ± 8 (17.8%)	95 ± 15 (15.8%)	13 ± 6 (46.2%)
Bin 3	158.5	52 ± 9 (17.3%)	125 ± 15 (12.0%)	33 ± 8 (24.2%)

Table 6.5: Yields in the CATS detector in three run periods, `TSpectrum` model.

Yield contamination

As part of the background analysis in Section 4.4 and the acceptance analysis in Section 6.3 it was determined that

$$\frac{\Omega_{\text{eff. inelastic}}}{\Omega_{\text{eff. elastic}}} \leq 1\%, \tag{6.2}$$

where $\Omega_{\text{eff. inelastic}}$ is the acceptance to the inelastic scattering events ($\gamma + {}^2\text{H} \rightarrow \gamma' + \text{n} + \text{p}$) and $\Omega_{\text{eff. elastic}}$ is the acceptance to the elastic (Compton) scattering events within the energy cut $-2\,\text{MeV} \leq \text{E}_{\text{miss}} \leq 3\,\text{MeV}$. Assuming that the cross-section for inelastic scattering is not more than twice as large as than the elastic cross-section (see Section 5.2.4), the contamination from inelastic scattering is expected to be $\lesssim 2\%$.

The contamination from the scattering in the Kapton vessel (see Section 4.4) can be addressed by analysing the data collected with the empty Kapton target (see Section 2.2.3). However, this requires a simulation of the geometry of the empty Kapton target which presently has not been developed. In Ref. [71], which measured the Compton cross-sections below the pion threshold in a similar setup, the contamination from the scattering in Kapton to the yields was estimated to be $(6 \pm 2)\%$ in CATS and consistent with 0 in BUNI. Similar contamination is expected above the pion threshold and the correction factors of Ref. [71] are used in this analysis. Thus the extracted yields in CATS (Tables 6.4 and 6.5) were scaled by 0.94, the yields in BUNI (Tables 6.2 and 6.3) remained unchanged.

To account for possible differences in the contamination from the Kapton below and above the pion threshold the 2% uncertainty was increased to 4%. This was combined with the 2% uncertainty related to the inelastic contamination. The combined uncertainty due to the contamination was rounded up to $\sqrt{4^2 + 2^2} \approx 5\%$. In principle this can be reduced by analysing the data from the empty Kapton target. However the uncertainty due to contaminations is rather small compared to the other sources of uncertainty. Thus the reduction of the contamination uncertainty is of limited practical value.

6.3 Detector acceptance

The acceptances of the detectors for Compton scattered photons were determined from a Geant4 simulation. To that end $5 \cdot 10^7$ Compton scattering events were simulated inside the liquid deuterium target and tracked through the experimental apparatus (generation of Monte-Carlo events is discussed in Appendix A.5). In each detector the acceptance was determined by

$$\Omega_{\text{eff}} = \frac{N_{[-2,\,3]\ \text{MeV}}}{N_{\text{throws}}} \cdot 4\pi, \tag{6.3}$$

where $N_{[-2,\,3]\ \text{MeV}}$ is the number of simulated events that resulted in a missing energy (Eq. (4.1)) between $-2\,\text{MeV} \leq \text{E}_{\text{miss}} \leq 3\,\text{MeV}$ and $N_{\text{throws}} = 5 \cdot 10^7$ is the total number of generated events. The simulated missing energy spectrum is depicted with the black line in Figure 6.8. The filled blue area depicts the region of the spectrum that defined the acceptance.

All of the systematic effects related to the detector acceptances were addressed identically as described in Section 5.3, except for the model dependence, which was not present in the Compton analysis. The systematic uncertainty of the detector acceptance in the Compton analysis was strongly dominated by the uncertainty of the energy cut. Recall that the uncertainty related to the energy cut originates from the calibration corrections discussed in Section 3.9. Due to the uncertainty the energy cut region may have been shifted by ±0.4 MeV. The reason why the uncertainty of the energy cut had a stronger effect in the Compton analysis is illustrated in Figures 6.7 and 6.8. The change in the acceptance was determined by the ratio $(A - \Delta A_1 + \Delta A_2)/A$, where A represents the integral over the yield integration range as specified in Figures 6.7 and 6.8. ΔA_1 and ΔA_2 denote the change in the integral as a result of shifting up the cut limits by 0.4 MeV. The integration range for the Compton signal in the missing

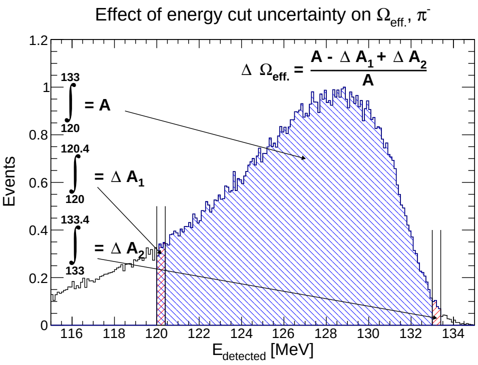

Figure 6.7: Effect of the uncertainty of the energy cut in the pion analysis. Yield integration range changed from [120, 133] MeV to [120.4, 133.4] MeV.

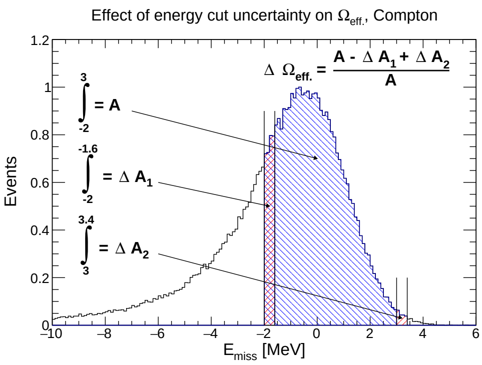

Figure 6.8: Effect of the uncertainty of the energy cut in the Compton analysis. Yield integration range changed from [-2, 3] MeV to [-1.6, 3.4] MeV.

energy spectrum was significantly narrower than the integration range for the pion capture signal in the detected energy spectrum. Due to this ΔA_1 and ΔA_2 constituted a larger portion of A in the Compton analysis as compared to the pion analysis. In principle the uncertainty could be suppressed by moving the left limit to a lower value (e.g. from -2 MeV to -4 MeV) or by adjusting the location of the right limit, such that $\Delta A_1 \approx \Delta A_2$ and thus $-\Delta A_1 + \Delta A_2 \approx 0$. However, as the effective suppression of the inelastic background depended on the left limit it could not be moved. Moving the right limit to a lower value would be possible, but this would reduce the yield count. The energy cut employed represents an optimal balance between the statistical uncertainty of the yield and the systematic uncertainty of the acceptance.

As the positioning of the detectors was slightly different in the run period in April 2015 as compared to the run periods in June and September 2011 two sets of acceptances were calculated. Tables 6.6 and 6.7 provide the acceptances of BUNI and CATS in the different run periods. Both the statistical and the systematic uncertainties are indicated. Sufficient Monte-Carlo events were processed to reach statistical uncertainty $< 1\%$. The systematic uncertainty was strongly dominated by the uncertainty due to the energy cut, which was $\sim 10\%$.

Detector acceptances, April 2015

Bin	BUNI Ω_{eff} [msr]	CATS Ω_{eff} [msr]
Bin 1	$33.03 \pm 0.18 \pm 3.27$	$27.0 \pm 0.16 \pm 2.55$
Bin 2	$31.97 \pm 0.18 \pm 3.14$	$26.17 \pm 0.16 \pm 2.51$
Bin 3	$30.82 \pm 0.18 \pm 3.06$	$26.11 \pm 0.17 \pm 2.54$
Bin 4	$29.86 \pm 0.20 \pm 2.97$	$25.75 \pm 0.19 \pm 2.61$

Table 6.6: Acceptances of BUNI and CATS in the run period in April 2015. The first uncertainty is statistical, the second is systematic.

Detector acceptances, June/September 2011

Bin	BUNI Ω_{eff} [msr]	CATS Ω_{eff} [msr]
1	$30.78 \pm 0.18 \pm 3.05$	$24.24 \pm 0.16 \pm 2.16$
2	$29.89 \pm 0.18 \pm 3.01$	$23.62 \pm 0.16 \pm 2.15$
3	$28.97 \pm 0.18 \pm 3.0$	$23.44 \pm 0.16 \pm 2.17$
4	$27.8 \pm 0.19 \pm 2.93$	$23.08 \pm 0.18 \pm 2.18$

Table 6.7: Acceptances of BUNI and CATS in the run periods in June and September 2011. The first uncertainty is statistical, the second is systematic.

6.4 Results and discussion

The yields and the acceptances were combined with the tagged photon flux (Section 5.4 Table 5.8) and the effective target thickness (Section 5.5 Eq. 5.14) to determine the differential cross-section for Compton scattering on the deuteron. Below the results in the two detectors (BUNI and CATS) are presented.

CATS (60° detector)

The cross-sections were evaluated using the yields determined with the two different fit models that employed different shapes for the random background. Figure 6.9 depicts the differential cross-section measurements in the three run periods using the CATS yields extracted with the polynomial fit model. The September 2011 data point is missing in the lowest energy bin, as the fit to the coincidence spectrum did not converge. Figure 6.10 displays the $d\sigma/d\Omega$ points evaluated with the yields extracted with the `TSpectrum` fit model. Visual comparison of Figures 6.9 and 6.10 reveals that the agreement of the measurements in the three run periods is slightly better with the yields extracted with the `TSpectrum` fit model, however the substantial statistical uncertainties make it difficult to draw firm conclusions. The spread of the results is believed to be caused by the unfavourable signal-to-background ratio, especially in the September 2011 data. The high count of background events makes the yields more

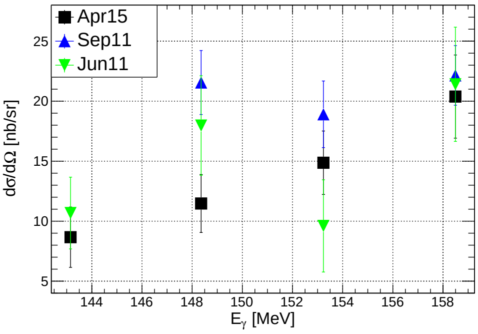

Figure 6.9: Differential cross-sections measured with CATS with the yields extracted with the polynomial fit model. The error bars indicate statistical uncertainties.

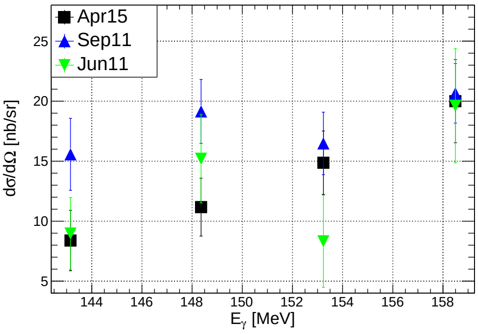

Figure 6.10: Differential cross-sections measured with CATS with the `TSpectrum` fit model. The error bars indicate statistical uncertainties.

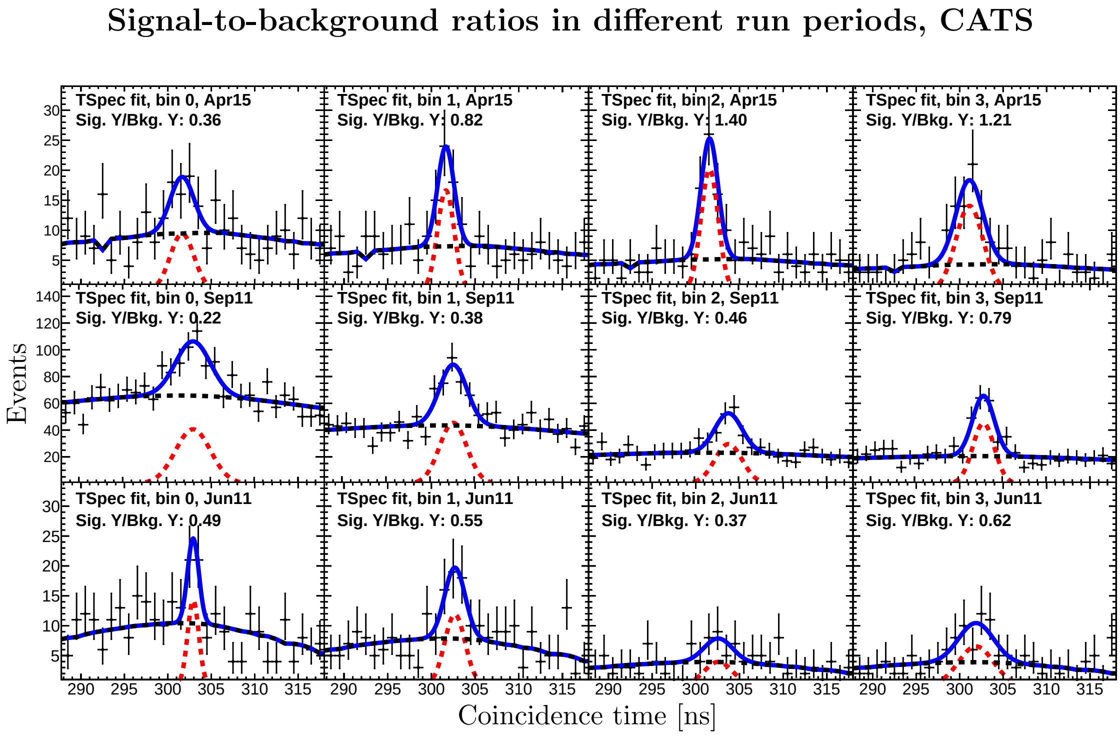

Figure 6.11: Fits to the coincidence spectra in four energy bins in the CATS detector in different run periods. Upper row - April 2015, middle row - September 2011, lower row - June 2011. The ratio of the signal yield to the background yield is indicated for each fit. The background rates were high in the two lower energy bins in September 2011.

sensitive to the background shape used in the fits. Figure 6.11 displays the fits using the `TSpectrum` model in the four energy bins in the three run periods. The upper, middle and lower row display the coincidence spectra in April 2015, September 2011 and June 2011, respectively. The quantity Sig. Y./Bkg. Y. indicates the ratio of the signal yield to the background yield. The best signal-to-background ratios were observed in the April 2015 data and the yields from that run period were also the least affected by the selection of the fit model. In the two lower energy bins the September 2011 data suffered from the worst signal-to-background ratios compared to the other run periods due to the high intensity of the tagged photon beam. In these bins the September 2011 data points seem slightly high with respect to the other run periods, but again the substantial statistical uncertainties complicate the comparison. The April 2015 and June 2011 data are consistent within statistical uncertainties in all energy bins. The September 2011 data are consistent with the April 2015 data in bins 2 and 3 and with the June 2011 data in bins 1 and 3. It does seem likely that there is some systematic spread in the results from different run periods and the dominant systematic effect is thought to come from the random background estimation.

The differential cross-section for each energy bin was taken to be average of the six points obtained from the different run periods and with the different fit models (except in the lowest energy bin, where there were five points due to the one non-convergent fit). The standard deviation of the points was interpreted as the systematic uncertainty that

Measured differential cross-section points at 60° (CATS)

Bin	En. [MeV]	$d\sigma/d\Omega$ [nb/sr]	Stat. err.	Sys. err.
Bin 0	143.2	10.5	1.6 (15.7%)	3.2 (30.5%)
Bin 1	148.4	16.1	1.8 (11.4%)	4.5 (28.2%)
Bin 2	153.2	13.8	1.8 (13.1%)	4.3 (31.2%)
Bin 3	158.5	20.7	2.1 (10.3%)	2.3 (11.3%)

Table 6.8: Measured differential cross-section points of Compton scattering on the deuteron at 60° (CATS detector).

accounted for the various sources that contributed to the spread of the measurements, including the difficulties related to the modelling of the background. The standard deviation was combined with the $\sim 10\%$ uncertainty of the detector acceptance and the $\sim 5\%$ uncertainty related to the contamination of the yields. The extracted differential cross-sections from the events in CATS are summarised in Table 6.8.

BUNI (120° detector)

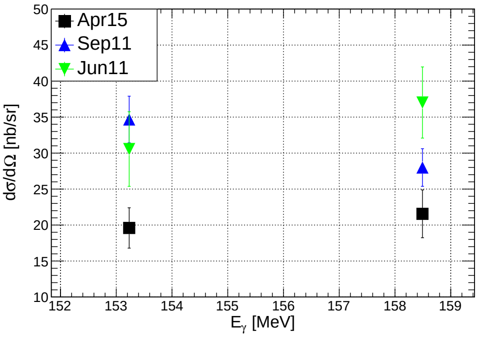

Figure 6.12: Differential cross-sections measured with BUNI with the yields extracted with the polynomial fit model. The error bars indicate statistical uncertainties.

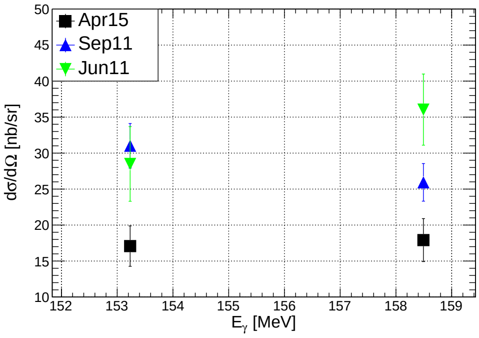

Figure 6.13: Differential cross-sections measured with BUNI with the yields extracted with the `TSpectrum` fit model. The error bars indicate statistical uncertainties.

In BUNI the differential cross-section points in the two higher energy bins were determined using the yields extracted with the polynomial fit model and the `TSpectrum` fit model and are depicted in Figures 6.12 and 6.13, respectively. Recall that the cross-sections could not be measured in the two lower energy bins due to the contamination from the π^- capture events (see Section 4.4). Generally the BUNI results are more spread out over the three run periods compared to the results from CATS, considering that the statistical uncertainties are smaller. The spread of the results is similar with both fit models. Similarly to the CATS analysis the average of the six points is reported as the differential cross-section for both energy bins. The standard deviation of the six points was combined with the $\sim 10\%$ uncertainty of the detector acceptance and the $\sim 5\%$ uncertainty associated with the contamination of the yields. The results are provided in Table 6.9. It is worth pointing out that despite the large

Measured differential cross-section points at 120° (BUNI)

Bin	En. [MeV]	$d\sigma/d\Omega$ [nb/sr]	Stat. err.	Sys. err.
Bin 2	153.2	26.9	2.2 (8.3%)	7.5 (27.9%)
Bin 3	158.5	27.7	2.2 (7.8%)	8.2 (29.5%)

Table 6.9: Measured differential cross-section points of Compton scattering on the deuteron at 120° (BUNI detector).

systematic uncertainties, the results in Table 6.9 served as reasonable estimates for Compton contamination analysis presented in Section 5.2.4.

Discussion

Figure 6.14 depicts the data from Tables 6.8 and 6.9. Currently no theoretical predictions are available for comparison. The differential cross-section at 60° increases with increasing incident photon energy. The Compton scattering cross-section on the proton starts to increase above the pion threshold (see e.g. [65]) and similar behaviour is expected for the Compton scattering cross-section on the deuteron. Although the high count of background events and the low count of Compton events complicated the analysis, the results from different run periods were in reasonable agreement. The differential cross-section measurements in different run periods at 120° were somewhat more spread out and the average results displayed in Figure 6.14 have sizeable systematic uncertainties.

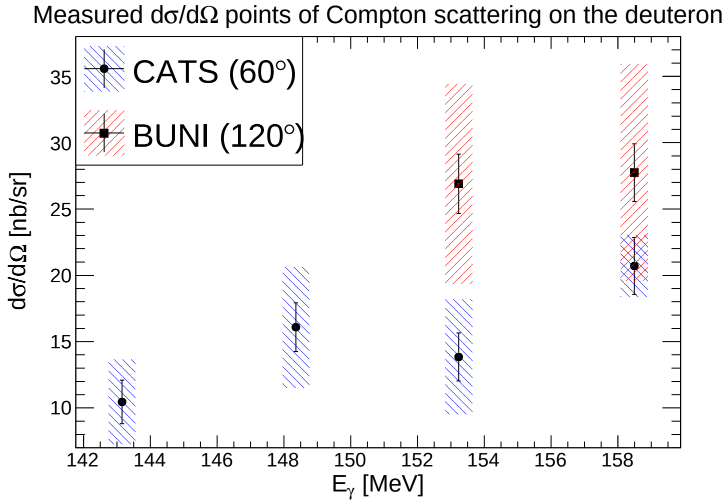

Figure 6.14: Measured differential cross-section points of Compton scattering on the deuteron at 60° (CATS detector) and 120° (BUNI detector). The error bars indicate statistical uncertainty, the striped boxes indicate the systematic uncertainties.

In summary, results of the first measurement of Compton scattering on the deuteron above the pion threshold have been presented. The modelling of the random background and the low count of Compton events have been identified as the main difficulties of the analysis. Two different methods to model the background have been presented and the results obtained with the different background models have been compared. The measured differential cross-sections at 60° revealed better consistency compared to the differential cross-sections at 120° and increase with increasing incident photon energy, which is the expected trend. Despite the sizeable systematic uncertainties this data will offer a benchmark for the theoretical models that aim to describe Compton scattering on the deuteron above the pion threshold.

Conclusions and outlook

This thesis presented the first measurement of the cross-section for π^- photoproduction and the differential cross-section for Compton scattering on the deuteron near the pion threshold. The measured cross-section for π^- photoproduction was compared to available theoretical models. The experimental data and the theoretical predictions were in good agreement in the vicinity of the threshold, in the higher energy bins the models and the data diverged. Improvement of the theoretical models is currently under way, which may reduce the discrepancy between the predictions and the experimental data. The theoretical treatment of the final state interactions in the reaction $\gamma + {}^2\mathrm{H} \rightarrow \pi^- + 2\mathrm{p}$ is the most challenging part of the calculation and is believed to be the most probable cause of the observed divergence. A theoretical model that succeeds in describing the experimental data in the full energy range has thus the potential to give valuable insight into the final state interactions. An improved understanding of the latter may have an important role to play in the interpretation of future experiments that involve complicated final states, for example as encountered in hadron spectroscopy.

In total six differential cross-section points for Compton scattering were extracted. The Compton scattering measurement was complicated by the low count of Compton events and the non-trivial structure of the random background. Currently no theoretical predictions for comparison with the experimental data are available. Despite the substantial statistical and systematic uncertainties the presented results can serve as an important benchmark for the future theoretical calculations. Further experiments with wider angular acceptance and higher statistical significance are required to substantially constrain the uncertainties of neutron polarisabilities. One such experiment, employing a Helium Gas Scintillator Active Target, is considered in Appendix B of this thesis.

Appendices

Appendix A

Lund simulations

Simulations played a very important role in the analysis of the Lund experiment. However, it was difficult to present all of the relevant aspects of the simulation within the analysis chapters without breaking the flow of thought. Instead, the results from the simulations were presented throughout the thesis where appropriate. This appendix summarises the few aspects that were important for accurate simulation results, but were inappropriate to introduce elsewhere. The simulations were carried out with the Geant4 [107] toolkit version 4.10.3. Section A.1 summarises the implementation of the geometry of the apparatus. In Section A.2 the simulation of the beam spot on the target is discussed. Section A.3 overviews the inclusion of the detector resolution effects and Section A.4 summarises some important aspects related to the simulation of the π^- capture reaction. Finally, Section A.5 discusses the generation of Monte-Carlo events.

A.1 Experimental hall geometry

The target and the detector geometries were realised according to the descriptions provided in Sections 2.1.2 and 2.1.3 and references therein. The positioning of the detectors in the experimental hall in different run periods is described in Table 2.1 and was varied accordingly in the simulation. The visualisation of the simulation is depicted in Figure A.1. The vacuum chamber and the Hostaphan windows of the target that were omitted from Figure 2.4 were included in the simulation are are indicated in Figure A.1.

A.2 Beam spot simulation

The beam properties at the target location were determined from the simulation. Knowledge of the beam radius and intensity profile was important, as it was used to determine the distribution of Monte-Carlo events in the X-Y plane inside the target. For example the X-Y starting coordinates of the simulated pions in the capture analysis (Section 5.6) were sampled from the simulated intensity distribution of the beam spot. Clearly a different beam radius would affect the number of pions that exit the target volume.

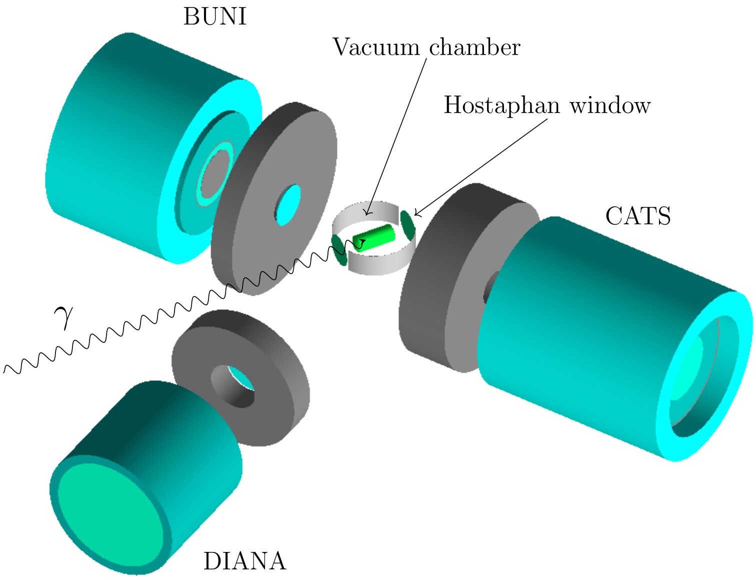

Figure A.1: Visualisation of the simulation of the experimental setup.

The beam properties at the target location were studied by realising the geometry of the beam line in Geant4. The geometry consisted of a radiator, a thin collimator with a diameter of 19 mm and an ideal detector at the target location. The distance between the radiator and the collimator was 3715 mm, the distance between the radiator and the ideal detector was 7435 mm (see Section 2.1.1). The geometry is illustrated in Figure A.2. Bremsstrahlung photons were produced by simulating a mono-energetic electron beam with an energy of 190 MeV impinging on the radiator. The generation of the resulting Bremsstrahlung photons was handled by the Geant4 software. The ideal detector registered the X-Y position of every Bremsstrahlung photon that passed through the collimator (solid green trajectory in Figure A.2). Photons that traversed some part of the shielding of the collimator (red dashed trajectory in Figure A.2) were not counted. Through this the radius and the intensity distribution of the beam spot at the target location were determined. It should be clarified that the actual collimator included significantly more shielding material compared to Figure A.2. Realistic shielding was not necessary in the simulation as it checked whether photons reaching the ideal detector had traversed any collimator material en route. The photons

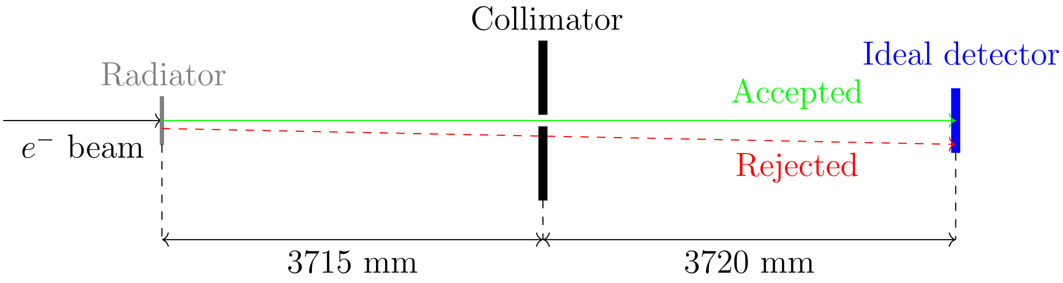

Figure A.2: Illustration of the beam line geometry (not to scale) for the beam spot simulation.

that traversed the material of the collimator shielding were not counted by the ideal detector.

Figure A.3 depicts a photo of the beam spot at the target location taken during the April 2015 run period. Figure A.4 displays a 2D histogram with the beam profile from the simulation. The radius of the simulated beam spot is in very good agreement with the radius of the photographed beam spot.

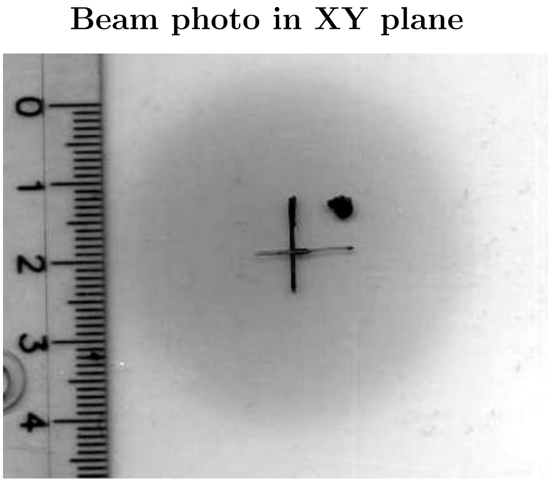

Figure A.3: Beam photo taken during the April 2015 data collection at the target centre location.

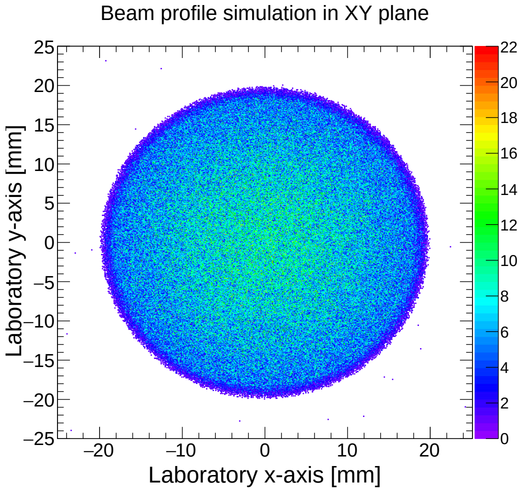

Figure A.4: Simulation of the beam radius and intensity distribution at the target centre location.

A.3 Detector response simulation

Accurate simulation of the detector response was very important to obtain correct simulated energy spectra. The best measure of the detector response was provided by the experimental in-beam data. After the calibration procedures of Chapter 3 the detected energy E_{detected} in each in-beam event was calculated and a histogram with the energy balance $E_{\text{detected}} - E_\gamma$ was filled, where E_γ was the energy of the tagged photon. The experimental in-beam data in the DIANA detector is depicted in Figure A.5 with black data points. Electromagnetic shower leakage from the crystals caused the energy balance spectrum of the experimental in-beam data to tail to the left. Several factors contributed to the resolution of the detector, which determined the width of the peak of the experimental in-beam data around zero. The blue dotted line in Figure A.5 is the energy balance in the DIANA detector from the simulation of the in-beam measurement. The simulation of the experimental setup for the in-beam measurement is illustrated in Figure A.6. In the simulation additional smearing of the detected energy was necessary to accurately emulate the response of the detector. The smearing was applied on an event-by-event basis by sampling a random number from a Gaussian distribution and adding it to the detected energy. The width of the Gaussian encoded the resolution of the detector. The parameters of the Gaussian were determined by convoluting the blue dotted line in Figure A.5 (the simulated energy balance without resolution smearing) with a Gaussian and fitting the experimental in-

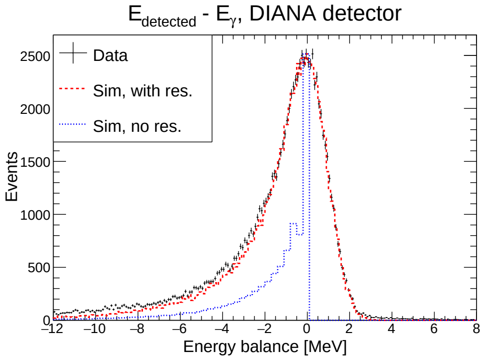

Figure A.5: Black points - in-beam experimental data from DIANA; blue dotted - simulation without smearing; red dashed - simulation with smearing.

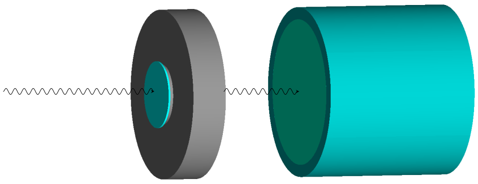

Figure A.6: Illustration of the in-beam simulation, DIANA detector.

beam data. The fit returned the mean and the width of the convoluting Gaussian. The red dashed line in Figure A.5 depicts the simulated in-beam data with the resolution effects taken into account. Clearly good agreement with the experimental data has been achieved. The parameters of the Gaussian function were found for each detector and similar agreement between the simulated and the experimental in-beam data was obtained.

A.4 π^- capture spectrum simulation

The Geant4 software simulated the capture of negative pions once they came to halt inside the liquid deuterium. However, it did not distinguish between the various scenarios listed in (2.4) – (2.8) and thus the photon from the radiative capture (2.5) was never emitted. This is a deficiency of the Geant4 software which had to be circumvented. The radiative pion capture was emulated by throwing photons sampled from the theoretical photon spectrum of the radiative capture reaction $\pi^- + {}^2\text{H} \rightarrow \gamma + 2\text{n}$.

The photon spectrum of the radiative capture reaction has been researched thoroughly, because the location of the peak is sensitive to the neutron-neutron scattering length a_{nn}. The most accurate measurement of the spectrum near the peak was performed by Gabioud *et. al.* in 1979 [106] using a pair-spectrometer with a resolution of 720 keV. Several theoretical models have been developed to describe the experimental data, two of them originate from the 1970's. The model by Gibbs, Gibson and Stephenson from Los Alamos [110, 125, 126] has been subsequently used in the analysis of later experiments performed in 1998 [127] and 2008 [128]. The model by de Téramond [129] was compared extensively to the experimental data by Gabioud *et. al.* in the 1980s [130, 131, 132]. In addition a more recent model that employs Chiral Perturbation Theory was published by Gårdestig *et. al.* in 2006 [133].

For this analysis the model by Gibbs *et. al.* [110, 125, 126] was used, as it was the only one that was readily available. The model by Gårdestig *et. al.* is expected to give similar results [134]. It was demonstrated already in Ref. [106] that both the models by Gibbs *et. al.* and by de Téramond agree with the experimental data extremely well in the region $E_\gamma \geq 127$ MeV. However the model by de Téramond uses rather simplistic descriptions for the deuteron and the neutron-neutron wavefunctions, which makes the prediction less trustworthy at lower photon energies (higher relative neutron-neutron momenta) [135].

A well motivated estimate of the model dependence can be obtained by comparing the different predictions by Gibbs *et. al.* de Téramond and Gårdestig *et. al.* As already mentioned, the latter two were not available for this analysis and additionally the model by de Téramond requires further improvement for a reliable description at low photon energies. The model by Gibbs *et. al.* has a theoretical uncertainty of $\lesssim 5\%$ at photon energies above $E_\gamma > 100$ MeV. The uncertainty increases with decreasing photon energy, but in this region the relative strength of the spectrum becomes weak and the uncertainty is suppressed [111]. The 5% theoretical uncertainty of the model by Gibbs *et. al.* was used as the model dependence in the acceptance analysis in Section 5.3.

Figure A.7 depicts the theoretical photon spectrum (gray fill) of the capture reaction by Gibbs *et. al.* [111]. The striped blue spectrum displays the simulated capture spectrum in the BUNI detector, when the capture photons were sampled from the displayed theoretical spectrum. The detector response modifies the theoretical spectrum significantly by widening the peak and shifting it to a lower energy. This affects the calibration offset analysis (Section 3.9) and the acceptance analysis (Section 5.3), illustrating the importance of the accurate simulation of the detector response effects discussed in the previous section.

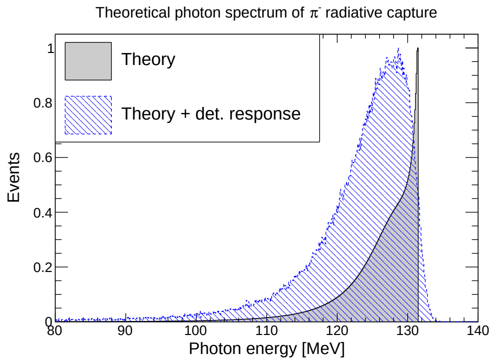

Figure A.7: Theoretical capture spectrum from Gibbs *et. al.* (gray fill) and the resulting detected energy spectrum (striped blue).

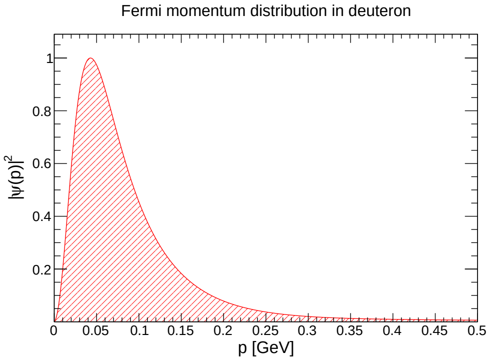

Figure A.8: Modulus square of the deuteron wavefunction in momentum space [136].

A.5 Generation of Monte-Carlo events

Inclusion of Fermi motion

In the simulation of Monte-Carlo events the dynamics of the proton and the neutron inside the deuteron had to be taken into account. For instance the charged pions were not created coherently on the deuteron, but either on the bound neutron (π^-) or the bound proton (π^+). In the following the generation of Monte-Carlo events of π^- photoproduction is considered as an example.

First, the magnitude of the Fermi momentum $|\vec{p}_{\rm cm}|$ was sampled from the modulus square of the momentum space wave-function $\Psi(p)$ [136] of the deuteron (depicted in Figure A.8). $\cos\theta_{\rm cm}$ and $\phi_{\rm cm}$, that determined the direction of $|\vec{p}_{\rm cm}|$ in the centre-of-momentum frame (deuteron at rest), were sampled from phase space. The Fermi-momentum three-vector was calculated as

$$p_{{\rm cm}_x} = |\vec{p}_{\rm cm}| \sin\theta_{\rm cm} \cos\phi_{\rm cm}, \tag{A.1}$$

$$p_{{\rm cm}_y} = |\vec{p}_{\rm cm}| \sin\theta_{\rm cm} \sin\phi_{\rm cm}, \tag{A.2}$$

$$p_{{\rm cm}_z} = |\vec{p}_{\rm cm}| \cos\theta_{\rm cm}. \tag{A.3}$$

The spectator nucleon (proton in this example) was forced on mass-shell by creating a momentum 4-vector

$$p_{\rm spectator} = (\sqrt{|\vec{p}_{\rm cm}|^2 + M^2_{\rm spectator}},\ -\vec{p}_{\rm cm}), \tag{A.4}$$

where $M_{\rm spectator}$ is the invariant mass of the spectator. The target nucleon (neutron in this example) was off mass-shell and the corresponding momentum 4-vector was

$$E_{\rm qf} = M_{\rm deuteron} - \sqrt{|\vec{p}_{\rm cm}|^2 + M^2_{\rm spectator}}, \tag{A.5}$$

$$p_{\rm qf} = (E_{\rm qf},\ \vec{p}_{\rm cm}). \tag{A.6}$$

In Eq. A.5 $M_{\rm deuteron}$ is the invariant mass of the deuteron and $E_{\rm qf}$ is the total energy of the off-shell target nucleon. In this example Eq. (A.6) defined the 4-momentum of the bound neutron target in the frame where the deuteron was at rest (laboratory frame).

To create the 4-momentum of the simulated π^- a “reaction” particle with a 4-momentum

$$p_{\rm reaction} = p_{\rm qf} + p_\gamma \tag{A.7}$$

was created. In Eq. (A.7) p_γ was the 4-momentum of the beam photon in the laboratory frame with an energy sampled from a Bremsstrahlung distribution (approximated by $f(x) = 1/x$) in the energy range $140 - 160$ MeV. $p_{\rm qf}$ was given by Eq. (A.6). The particle described by Eq. (A.7) was decayed in its rest frame to the reaction products, in this case to a π^- and a proton. The magnitude of the momentum $|\vec{p}_{\rm cm'}|$ of the decay products was completely determined by the kinematics. When possible the $\cos\theta_{\rm cm'}$ was sampled from a known distribution. For instance in case of π^- photoproduction the $\cos\theta$ distribution of the pions in the elementary reaction $\gamma + {\rm n} \to \pi^- + {\rm p}$ was used [40]. Otherwise the angular distribution was sampled from phase space. The angles ($\theta_{\rm cm'}$, $\phi_{\rm cm'}$) and $|\vec{p}_{\rm cm'}|$ were used to form three-momenta according to Eqs. (A.1) – (A.3). As a final step the 4-momenta

$$p^{({\rm cm'})}_{\pi^-} = (\sqrt{|\vec{p'}_{\rm cm}|^2 + M^2_{\pi^-}},\quad \vec{p'}_{\rm cm}), \tag{A.8}$$

$$p^{({\rm cm'})}_{\rm p} = (\sqrt{|\vec{p'}_{\rm cm}|^2 + M^2_{\rm p}}\ ,\ -\vec{p'}_{\rm cm}), \tag{A.9}$$

were boosted from the rest frame of the reaction particle to the laboratory frame, resulting in $p^{({\rm lab})}_{\pi^-}$ and $p^{({\rm lab})}_{\rm p}$. In Eqs. (A.8) – (A.9) M_{π^-} and $M_{\rm p}$ stand for the invariant masses of the π^- and the proton, respectively.

It is understood that the outlined method had limitations. For instance it neglected the baryon-baryon Final State Interactions, which may have been substantial. However it did offer a kinematically more accurate picture compared to the situation where the Fermi motion was not included.

Coherent dynamics

In the generation of Monte-Carlo events where the deuteron acted as the target (e.g. elastic scattering $\gamma + {}^{2}\mathrm{H} \to \gamma' + {}^{2}\mathrm{H}'$) the steps before Eq. (A.7) were unnecessary. In this case the reaction particle was defined as

$$p_{\mathrm{reaction}} = p_{\mathrm{D}} + p_{\gamma}, \tag{A.10}$$

where p_{D} was the 4-momentum of the deuteron at rest. Otherwise the generation of the events was identical.

Appendix B

Compton scattering on ^{3}He

Recently a Helium Gas-Scintillator Active Target (HeGSAT) [79, 80] was reported for a total photoabsorption cross-section measurement on ^{4}He. In parallel, as a theoretical advancement the Compton scattering reaction

$$\gamma + {}^3\mathrm{He} \to \gamma' + {}^3\mathrm{He}' \tag{B.1}$$

has been formulated in a manner suitable for extraction of the neutron polarisabilities [76, 77] (see also Section 1.2). Combining these two separate developments led to a proposal [137] to use the HeGSAT for Compton scattering measurements on ^{3}He and ^{4}He isotopes at the the tagged photon facility [138, 81] at MAMI [139] in Mainz, Germany. Although the Program Advisory Committee gave the proposal the highest rating, it soon became apparent that a modified HeGSAT would be preferable for use at Mainz. A new HeGSAT design was proposed by Annand at the University Of Glasgow in November 2014. The feasibility study of the new design with the Geant4 toolkit [107] is the subject of this appendix. Section B.1 will provide a brief introduction to the working principle of an Active Target. Section B.2 reviews the original HeGSAT and outlines the main reasons for upgrade. Section B.3 discusses the upgraded HeGSAT design. Sections B.4 and B.5 form the the heart of this appendix, with the former providing an overview of the development of the simulation and the latter reviewing the assessment of the detector design with the help of this simulation. The appendix is finalised with a brief summary in Section B.6.

B.1 Working principle of an Active Target

In Compton scattering the energy of the scattered photon is determined by Eq. (1.15). On a proton target the Compton scattered events are easy to identify by calculating the expected energy of the scattered photon and demanding the energy balance to be zero,

$$E'_\gamma - E_{\mathrm{detected}} = 0. \tag{B.2}$$

In Eq. (B.2) E'_γ is the expected photon energy calculated from Eq. (1.15) and E_{detected} is the experimentally detected energy at a certain laboratory angle.

Things are slightly more complicated for light nucleus targets, which are necessary to probe Compton scattering on the neutron. For Compton scattering on ^{3}He there are quasi-free channels in addition to the coherent Compton scattering

$$\gamma + {}^{3}\mathrm{He} \rightarrow \gamma' + {}^{3}\mathrm{He}'. \tag{B.3}$$

For instance the photon could scatter from a neutron inside the nucleus, resulting in

$$\gamma + {}^{3}\mathrm{He} \rightarrow \gamma' + \mathrm{n} + 2\mathrm{p}. \tag{B.4}$$

In this case the energy of the scattered photon is reduced by at least the binding energy of ^{3}He. However, due to the finite resolution of the detector and the Fermi motion of the neutron the quasi-free channel (B.4) may be difficult to separate from the coherent channel (B.3).

This problem can be overcome by using an *Active Target*. An Active Target is a device that performs as a target for the photon beam and a detector for recoiling particles. This is possible, for example, with noble gas targets because they scintillate light when energetic particles deposit energy in the gas medium. The number of emitted scintillation photons is proportional to the deposited energy. If this light can be collected the energy deposits of the particles traversing the gas medium can be measured.

More specifically, for the experiment at hand, using an Active Target enables one to detect the energy of the recoiling ions, such as the ${}^{3}\mathrm{He}'$ in Eq. (B.3) and the protons in Eq. (B.4). It is expected that the energy signature in the Active Target is different in the coherent scattering and the break-up reactions. Combining this information with a high quality photon calorimeter (such as the Crystal Ball detector [138] in Mainz) should allow efficient separation of the coherent Compton scattering signal from the background channels.

B.2 Original HeGSAT and reasons for upgrade

The original Helium Gas-Scintillator Active Target was developed at the University Of Glasgow by Al Jebali and Annand. An excellent overview of that process is presented in the PhD thesis of Al Jebali [79] with a shorter summary available in a subsequent publication [80]. Here it is thus only considered briefly with the main aim to clarify the motivation for the upgrade.

The original HeGSAT is depicted in Figure B.1. The detector consisted of four identical gas container cells with four optical windows per cell for the scintillation light readout. When operational, photomultiplier tubes were attached to the HeGSAT optical windows to register the emitted scintillation light. In addition to the four main cells two end cells were present to separate the beryllium pressure windows from the four main cells. The end cells were present to register and remove background events where the incident photon interacted in one of the beryllium pressure windows. The inside of each cell was covered with reflective paint to maximize the amount of scintillation light that would reach the optical windows and be registered by the PMTs.

Helium scintillates in UV, which is difficult to detect with conventional PMTs. To that end a small amount of Nitrogen (500 permille) was added to the helium gas to act as a wavelength shifter. In the $\mathrm{N}_2 - \mathrm{He}$ gas mixture the scintillation occurs in the visible

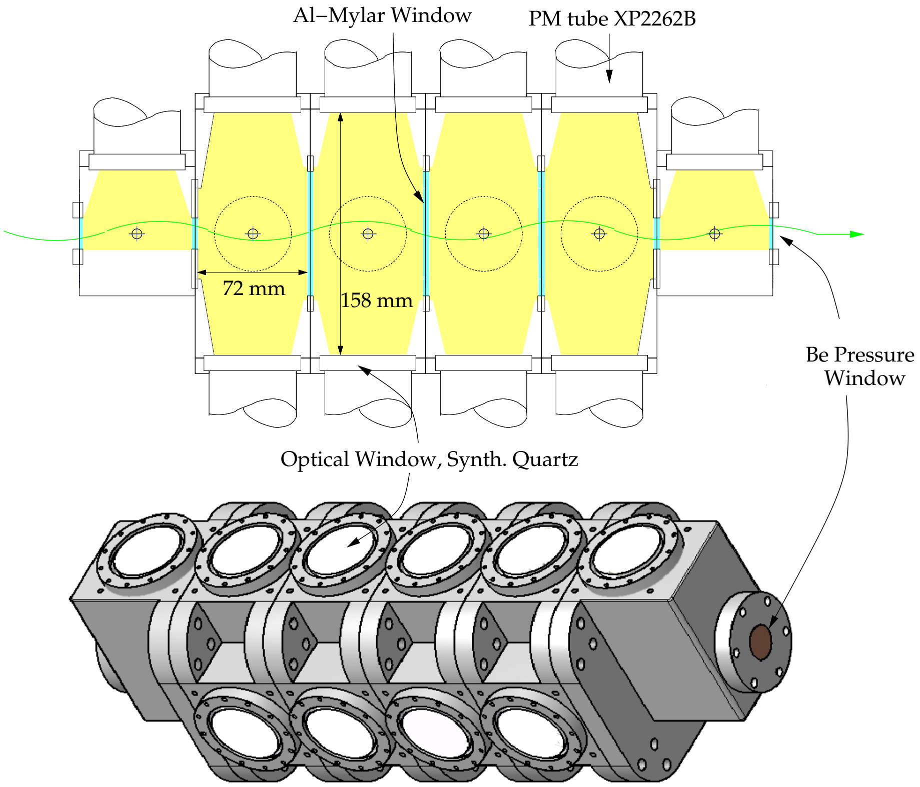

Figure B.1: Original HeGSAT design. The photon beam is depicted with the green wave. The upper image depicts the cross-sectional view of the four main gas cells and the two end gas cells. The lower image depicts the 3D model of the full HeGSAT. Image from Ref. [79].

region around a wavelength of 420 nm, which is optimum for the photomultipliers. The gas pressure during measurements could be varied, but typically 20 bar was used.

Although the design discussed above has been proven to work, it became evident that using the original HeGSAT for the experiment in Mainz would impose considerable difficulties. The main concern was the pressure safety of the vessel. The experimental set-up would have the HeGSAT placed inside the Crystal Ball detector [138]. The Crystal Ball is a large spherical photon calorimeter built out of sodium iodide crystals. It has almost 4π angular coverage and the inner chamber of the detector where HeGSAT would be placed has a radius of 25.3 cm. If one of the optical windows of the HeGSAT were to break due to the high pressure inside the device, it could cause significant damage to the Crystal Ball calorimeter.

Secondly, the original HeGSAT was designed to measure the total photoabsorption cross-section of ^{4}He in Lund, where there was ample space around the device. Fitting the original HeGSAT into the Crystal Ball detector would be dimensionally challenging. In addition a special support mechanism would need to be developed to hold the HeGSAT in place.

Thirdly, the mechanical design of the original HeGSAT is non-trivial and achieving complete pressure tightness at 20 bar is difficult. This does not constitute a problem for experiments with ^{4}He as the gas is in ample supply and leakage can be easily compensated. ^{3}He however is expensive and any leakage of that would be very costly.

B.3 Modified design

Due to the reasons presented in the previous section, a new design for the Helium Gas-Scintillator Active Target was proposed by Annand from the University of Glasgow in November 2014. The original drawing is depicted in Figure B.2. The pressure vessel of the new design consists of a cylindrical main cell (inner diameter 102 mm, inner length 420 mm) and two cylindrical extension cells (inner diameter 20 mm, inner length 206 mm). The extension cells serve the same purpose as the end cells of the original HeGSAT. They are present to exclude background from the beryllium pressure windows from entering the main cell of the device. Note that the diameter of the main cell is less than that shown in the drawing. Also the PTFE diameter is 82 mm, not 190 mm. The reasons for the radius reduction are provided in Section B.5. The material of the vessel is aluminium alloy (5 mm thickness). Both extension cells have a pressure tight beryllium window (0.5 mm thickness) at one end for photon beam entry and exit. The upstream end wall of the main cell has pressure tight connectors for connection to the optical sensors and electronics located inside the cell.

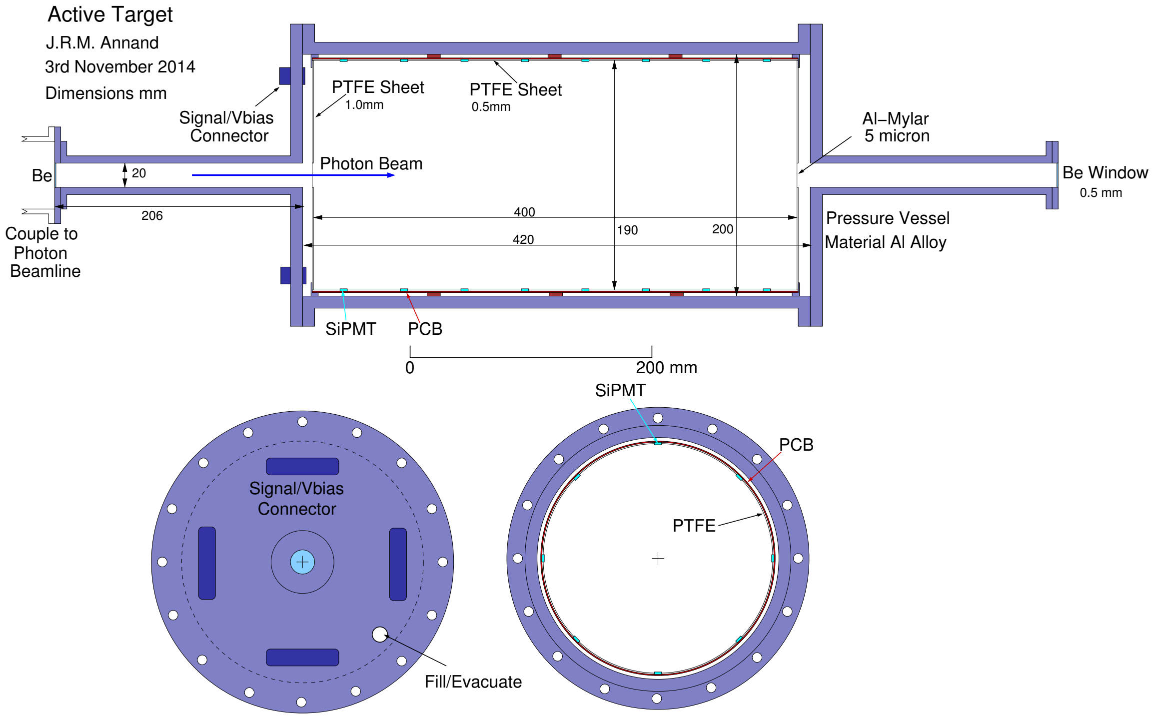

Figure B.2: New HeGSAT by Annand in November 2014, original drawing. Two dimensions are not indicated. The pressure vessel wall thickness is 5 mm, the PCB thickness is 1 mm. Also, two dimensions have been changed. The new inner diameter of the PTFE cylinder has been reduced from 190 mm to 92 mm and the inner diameter of the pressure vessel has been reduced from 200 mm to 102 mm. See Section B.5.2.

Inside the main cell is an optically isolated volume and the Compton scattering events that occur inside that volume will be recorded for the cross-section measurement. The optically isolated volume is built from a cylindrical Printed Circuit Board (PCB) (1 mm thick) with an outer layer of reflective Polytetrafluoroethylene (PTFE) (0.5 mm thick). PTFE is a commonly used reflector, see e.g. [140, 141]. The PCB cylinder is closed from both ends with PTFE sheets (1 mm thick) that have aluminised mylar windows at the centre (5 μm thick, 20 mm diameter) for beam entry and exit. Aluminised Mylar is a thin polymer film that is coated with a layer of aluminium to make it reflect light. There are sixty four 6×6 mm Silicon photomultiplier (SiPM) cells attached to the PCB cylinder to collect scintillation light. The PTFE has apertures where the SiPMs are located.

Compared to the original HeGSAT outlined in the previous section, the upgraded version addresses all of the main concerns related to the proposed experiment in Mainz. The simpler mechanical construction and shape increase the pressure safety of the vessel and make it straightforward to fit the HeGSAT into the Crystal Ball detector. Additionally, moving from the conventional photomultiplier tubes to the silicon photomultipliers eliminates the need for optical windows, which constituted a concern for the engineers in Mainz. In general the new design has much less material which might attenuate the scattered γ's.

B.4 Detector simulation development

B.4.1 Geometry

Geant4 based software [107] was used to create a simulation of the new HeGSAT design. The initial geometry was programmed according to the dimensions depicted in Figure B.2. The procedure was relatively straightforward, but there are some technicalities that are worth addressing in detail.

Hierarchy of volumes

In Geant4 the geometrical realisation of any detector design relies on the concept of "volumes" (see Section 2.2 of Ref. [120]). Any user can choose their own way of building the hierarchy of volumes, depending on their needs. For this project two distinct ways to build the volume hierarchy were considered.

1. Define "The World" volume as the only mother volume and define all other parts of the detector as equal daughters of "The World" volume. This would result in an easily comprehensible two-level volume hierarchy. One of the advantages of having equal level components is that these volumes are not allowed to overlap by Geant4 (see 4.1.11 of Ref. [120]), meaning that any programming errors that could cause detector component displacements would be easier to detect. Such a volume hierarchy is depicted in Figure B.3.

2. Define a structured hierarchy of volumes, such that the pressure vessel volume is the daughter of "The World" volume, PCB volume is the daughter of the pressure vessel volume etc. In such a set-up Geant4 issues an overlap error only if the daughter volume is outside or partly outside of the mother volume. The benefit of such a hierarchy structure is that it is much easier to place smaller detector components into a larger compound. This volume hierarchy is illustrated in Figure B.4.

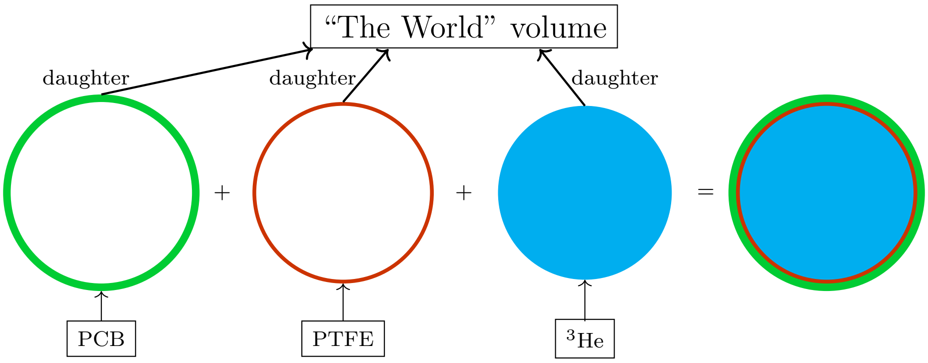

Figure B.3: Simple two-level volume hierarchy in the Geant4 simulation of the HeGSAT. The rings show the cross-sections of the cylindrical shapes that were used to build the optically isolated volume with one mother volume and multiple equal level daughter volumes.

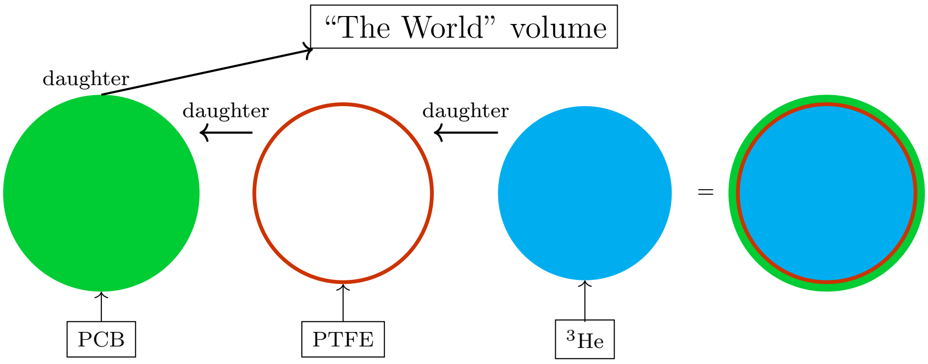

Figure B.4: Multi-level volume hierarchy in the Geant4 simulation of the HeGSAT. In this case the ^{3}He volume is the daughter of the PTFE volume and the PTFE volume is the daughter of the PCB volume.

As seen in the right-hand images of Figures B.3 and B.4, the geometrical result of the two methods is the same. However, with the two-step volume hierarchy the PTFE layer did not behave as a reflector and optical photons reached the PCB. Implementing the geometry with the multi-level volume hierarchy (as illustrated in B.4) avoided this problem and optical photons reflected from the PTFE. The malfunction of the simpler hierarchy was not investigated. Defining an optical property of a material in Geant4 means defining a behaviour for the optical photons when they reach a boundary of that material (e.g. should the photon reflect, refract or absorb, see Section 5.2.5.4 of Ref. [120]). It is possible that the unexpected behaviour with the two-step hierarchy was related to confusion of the boundaries between the equal level daughter volumes, as well as to the placement of the silicon photomultipliers inside the helium volume (see the next paragraph).

Silicon photomultiplier placement and geometry

The helium gas inside the optically isolated volume is programmed as a daughter of the PTFE volume. This configuration demanded a slight modification to the inner shape of the PTFE cylinder in order to avoid the SiPMs expanding into both the helium and the PTFE, which is not allowed by Geant4 for this volume hierarchy. For that reason some "flattening" of the inner radius of the PTFE cylinder was performed, such that the SiPMs are placed wholly inside the helium volume and make smooth contact with the PTFE. Figure B.5 illustrates how the flattening was performed. The red lines show a part of the cross-section of the PTFE cylinder. The blue box is a cross-section view of a simple box that has the length of the cylinder. Variable x is half the width of the SiPM, such that the full width of the flattening box exactly fits a SiPM cell on top. The thickness of the flattening box was calculated as

$$h = R_{\mathrm{PTFE}} - \sqrt{R_{\mathrm{PTFE}}^2 - x^2}, \tag{B.5}$$

where x stands for half the length of the SiPM cell and R_{PTFE} is the inner radius of the PTFE cylinder. The flattening box volume and the PTFE volume were united in the Geant4 simulation using `G4UnionSolid` boolean operators, see 4.1.2.2 of Ref. [120]. A flattening was introduced for each row of SiPMs along the HeGSAT length (z). This means that each of the SiPM rows visible in the bottom right drawing of Figure B.2 has a suitably oriented flattening box under it.

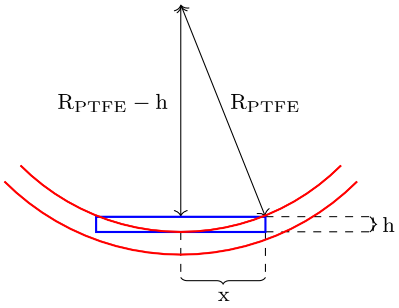

Figure B.5: Illustration of how the flattening box and the PTFE are merged together. R_{PTFE} is the inner radius of the PTFE cylinder, x is half the width of the SiPM cell and h is calculated such that the cylinder and the box are fully unified.

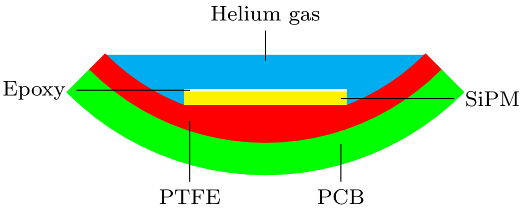

Figure B.6: Illustration of the detector geometry in the Geant4 simulation. SiPMs and the covering epoxy films are daughter volumes of the helium gas volume; flattening of the inner PTFE cylinder enabled smooth contact between the PTFE and the SiPMs.

Figure B.6 illustrates a part of the cross-section view of the optically isolated volume (the dimensions are not to scale). As indicated, the SiPMs are covered by a protective epoxy layer. The simulation has been developed with silicon photomultipliers from SensL in mind. The specific model is C-series 6 × 6 mm SiPMs [142]. The epoxy layer is 200 μm thick and has a refractive index of 1.54 at $\lambda = 589$ nm. More detailed properties of the epoxy layer were considered "commercially sensitive information" and were therefore not disclosed by the company.

The epoxy films are realised as simple shapes the same length and width as the SiPMs with a thickness of 200 μm, that are placed on top of the SiPM cells. The presence of these films does not have a strong influence on the number of detected photons. The main effect of the epoxy layers in the simulation is controlling that only optical photons that strike the SiPMs from the top side produce a signal (photons that do not pass epoxy are not counted).

B.4.2 Material properties

In the simulation seven materials are used to build the HeGSAT. Many of these materials were already used in the original HeGSAT design and had been programmed for the simulation of that detector. These material compositions were re-used in the new simulation, the others were defined anew. Below a list of the material compositions is provided. All the chemical elements that were used to build the materials were retrieved automatically from the National Institute of Standards and Technology (NIST) database [118] by the Geant4 `G4NistManager` class.

1. Beryllium windows. The beryllium windows used in the previous target were custom-made specifically for that detector and were implemented in Geant4 according to the specification sheet that came with the order [143]. The new design will re-use the beryllium windows and the properties were copied from the simulation of the original HeGSAT. The windows consist of: i) 0.06% silicon; ii) 98.73% beryllium; iii) 0.15% carbon; iv) 0.75% oxygen; v) 0.08% magnesium; vi) 0.1% aluminium; vii) 0.13% iron. The density of the material is 1.84 g/cm^3.

2. Helium-nitrogen gas mixture. The gas mixture comprises of 99.95% ^{3}He and of 0.05% nitrogen. The density of the gas is calculated from the ideal gas law using pressure 20 bar, molar mass of 3.0160293 g/mol for ^{3}He, temperature 293 K and ideal gas constant 8.314 J/(mol · K). In the first approximation the nitrogen concentration can be ignored.

3. Aluminised Mylar. The aluminised Mylar windows were also used in the previous HeGSAT. The material is defined according to the chemical composition of Polyethylene terephthalate, $C_{10}H_8O_4$, which gives mass fractions 62.5% carbon, 33.3% oxygen and 4.2% hydrogen. The aluminium layer that covers the polymer film to make it reflect light is very thin and therefore negligible in the material composition. The density of Mylar is set to 1.40 g/cm^3.

4. PTFE reflector. The PTFE reflective material was defined using the chemical composition of Polytetrafluoroethylene, $(C_2F_4)_n$, which yields mass fractions 24% carbon and 76% fluorine. The density of PTFE is set to 2.2 g/cm^3.

5. Epoxy film covering the SiPMs. As was mentioned earlier, very little information about the epoxy layer was available from the company. With no better options available, a version of an epoxy from the A2 Collaboration detector simulation was used. The epoxy is defined to consists of 80% epoxy resin and of 20% amine hardener with an overall density of 1.2 g/cm^3. In turn, the epoxy resin is programmed according to the chemical formula $C_{21}H_{25}ClO_5$ with a density of 1.15 g/cm^3. The amine hardener is defined according to $C_8H_{18}N_2$ with a density of 0.94 g/cm^3.

6. SiPMs. The silicon photomultipliers are defined to consist of only silicon with a density of 2.329 g/cm^3.

7. PCB. The printed circuit board is defined to consist of only carbon, material taken directly from NIST database.

8. Aluminium. The vessel material was defined to consist of only aluminium, material taken directly from NIST database.

Due to the nature of the experiment the material properties of the vessel and the gas mixture are by far the most important ones. The beryllium windows have moderate effect, the chemical composition of the other materials is expected to have very little relevance. The reason for that stems from the distinct energy regimes that are present in the experiment and from the detection mechanism. There are three typical energy bands for the particles involved in the experiment. The γ photons from the beam have typical energies from 50 to 200 MeV. The recoiling particles (either ^{3}He or protons, neutrons and deuterium atoms from helium break-up) have kinetic energies up to $\sim$20 MeV. The scintillation photons are in the optical region, peaking around an energy of $\sim$3 eV ($\approx$400 nm wavelength).

The photons from the beam that collide with ^{3}He and then exit the target have high energies compared to other participating particles. With the dimensions of the target in mind, the only media that have enough substance along the high-energy photon trajectories to produce a non-negligible interaction probability are: i) the gas mixture along the beam direction; ii) the pressure vessel; iii) the beryllium windows. All other parts of the detector are too thin to produce significant high-energy photon interactions.

The recoiling particles have energies that allow them to penetrate into the PTFE layer, the PCB layer, the pressure vessel and even exit the HeGSAT. For an accurate simulation of the recoiling particles that do not stop in the gas mixture most of the material properties are relevant. However, the first aim of the simulation is to study the detector acceptance for the Compton scattering reaction on ^{3}He. The extraction of the Compton scattering signal on ^{3}He relies on the recoiling helium stopping inside the gas mixture. This allows one to determine the kinetic energy of the recoiling helium through collecting scintillation light and makes the experiment kinematically complete. If the recoiling helium does not stop in the gas, the Compton event will not be accepted. Where the recoiling particle ends up in this case is irrelevant. Obviously the only parameters of the detector geometry that determine how well the recoiling helium atoms stop inside the gas mixture are the dimensions and properties of the gas mixture. All other material properties only affect the events that are not of interest.

In Geant4 the optical photons are treated differently from high-energy photons. The behaviour of the optical photons is determined by the optical properties that are attached to the materials through `G4MaterialPropertiesTable` class. Therefore the chemical properties of the materials that were discussed in this subsection do not affect the optical photons; the relevant parameters are discussed separately in the following subsection.

B.4.3 Optical properties

The effective collection of the scintillation light is at the heart of the detector design. One of the main purposes of the detector simulation is to determine how many of the produced optical photons reach the SiPMs. Therefore it is important to model the optical properties of the parts of the detector that determine the behaviour of the optical photons as accurately as possible. This, however, is not trivial. The uncertainty is largely dominated by the limited information available on the scintillation spectrum and the scintillation yield of the helium-nitrogen gas mixture. Thus the optical properties of the He-N system are discussed separately in the following paragraph, the optical properties of the other relevant materials are discussed in the second paragraph of this subsection.

Optical properties of the He-N gas mixture

Gas scintillation is a complex atomic process which depends on the pressure and the temperature and in this case also on the nitrogen concentration of the gas mixture. Public information on the specific system is sparse. The gas mixture properties relevant for the previous HeGSAT design were studied in Ref. [79]. Importantly it has been confirmed with measurements that the inclusion of nitrogen does shift the helium scintillation light to the visible region. From the emission spectrum of nitrogen, from quantum efficiency spectrum of the photomultiplier tubes that were used with the previous target (see Section 2.4.6 of Ref. [79]) and the observed scintillation signal, it was concluded that the scintillation spectrum of the gas mixture peaks around 400 nm wavelength. Indeed, under the simplistic assumption that the helium scintillation is absorbed by nitrogen and then re-emitted, strong intensity around 400 nm is expected from the reported spectral lines [118]. In addition, a book by Brouns [144] references unpublished work by Brauer and co-workers, who claim to have seen the brightest scintillation lines from a He-N mixture (0.2% nitrogen) at 391.4 nm and 426.9 nm.

The range of the scintillation spectrum of the He-N gas mixture is largely unknown. An argon-nitrogen mixture, where nitrogen is added as a wavelength shifter, is reported to scintillate in the region 337 - 520 nm [145]. As similar physical processes lead to scintillation in the visible region in both the He-N and the Ar-N mixture, the interval quoted above can be considered as a very rough indicator for the scintillation spectrum band of the He-N system. However it is not clear from Ref. [145] whether higher wavelengths were studied. The scintillation spectrum of nitrogen at very low pressure (< 0.1 Pa) has been measured in the interval 200 - 600 nm in Ref. [146]. The spectrum reveals strong lines around 400 nm, consistent with the discussion above, with lower intensity lines appearing all the way up to 600 nm wavelength. The scintillation spectrum of nitrogen at low pressure is only an approximate indicator of the scintillation spectrum of the He-N system, yet it does seem to suggest that one might expect scintillation photons over a wide band of wavelengths.

With all of the above taken into account, in the simulation the scintillation spectrum was defined in the range 320-660 nm with a strong peak from 400 to 440 nm. The band 320 - 660 nm corresponds to the region where the SiPMs have detection efficiency greater than 10% (see Figure B.10). It is understood that constraining the scintillation spectrum only to the sensitive region of the SiPMs does not reflect the full physical reality, yet from the viewpoint of the simulation it does not make sense to include photon energies that cannot be detected. The scintillation spectrum that is used in the Geant4 simulation is depicted in Figure B.7.

Additionally the simulation required a value for the parameter `SCINTILLATIONYIELD`. The parameter determines the number of optical photons that are generated per deposited MeV (see 5.2.5.2 in Ref. [120]). The energies of the generated photons are determined by the scintillation spectrum depicted in Figure B.7. As a first estimate the scintillation yield value 250 photons per deposited MeV was used. This number is based on private communication with the author of the previous HeGSAT design (Annand) and with the author of the Geant4 simulation of the previous HeGSAT (Al Jebali).

In the end the value of the parameter `SCINTILLATIONYIELD` will be obtained from experimental measurements using the detector. This procedure is best explained by an example. Assume that an alpha source that emits particles with energy E_α is placed inside the optically isolated volume. Low E_α values are assumed, such that all alpha particles stop inside the gas mixture. Each event will result in a signal in the SiPMs. The alpha particles can be simulated and the value of the parameter `SCINTILLATIONYIELD` can be tuned to match the output from the simulation to the output from the detector.

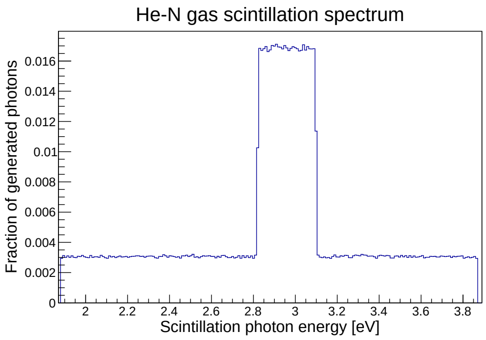

Figure B.7: The scintillation spectrum of the He-N gas mixture as defined in the Geant4 simulation. The distribution is normalised to 1. More photons are generated into the spectrum range from 400 nm - 440 nm (3.1 eV - 2.8 eV).

The absorption length of the He-N gas mixture is expected to be negligible compared to the absorption in the PTFE reflector and is set to a constant 3500 cm. The refractive index of the He-N gas is set to a constant value of 1.00003 [147]. In Geant4 one can control the time structure of the scintillation through parameters `FASTTIMECONSTANT`, `SLOWTIMECONSTANT` and `YIELDRATIO` (see 5.2.5.2 in Ref. [120]). The time structure of the He-N scintillation was studied extensively in Ref. [79] and the new simulation re-uses the values reported therein (30 ns, 60 ns and 1, respectively). These values do not affect the results presented in this appendix, but will be relevant if analysis involving hit timing is performed.

Optical properties of other relevant materials

The optical properties of the PTFE reflector are better known. The reflectance of PTFE is ∼95% and relatively flat over the wavelength region of interest [140]. PTFE is a Lambertian reflector, therefore the `G4OpticalSurface` model was defined with parameters `unified, groundfrontpainted, dielectric_dielectric` (see 5.2.5.4 in Ref. [120]).

The reflectance of aluminised mylar windows was measured for the previous HeGSAT design and is reported to be flat at 95% in the optical region [79]. The refractive index of the mylar windows is not known precisely. However this parameter does not affect the number of detected photons as it controls the trajectories of the optical photons that exit the optically isolated volume. A constant refractive index of 1.68 is used, which is based on [148]. The optical surface of the mylar windows was defined similarly to the PTFE with the parameter `groundfrontpainted` changed to `polishedfrontpainted`. This change accommodates the fact that aluminised mylar is a spike reflector and not a Lambertian reflector.

The epoxy film is set to have a constant refractive index of 1.54 and transmittance

1.0 over the full optical spectrum. The specified photon detection efficiency of the SiPMs has been determined with the epoxy layer present. Including an absorption spectrum for the epoxy layers would thus double count the reduction in the number of detected photons. The optical surfaces of the epoxy films are defined similarly to PTFE, but this time the parameter `groundfrontpainted` is changed to `ground`. This is a slightly more complicated model, which allows transmittance through the material, and requires a value for parameter `sigmaalpha`. This parameter describes the microscopic structure of the surface and a value of 0.21 rad (12°) is used, based on [141]. It could be argued that, with the limited information available on the epoxy films, it might be better to omit them from the simulation. However, the presence of the epoxy films allows an easy way to control that only photons incident on the top side of the SiPMs are counted, resulting in more realistic simulation results.

Finally, the optical surfaces of the SiPMs are defined with a 100% photon detection efficiency over the full scintillation spectrum, such that any photon that reaches the SiPM surface through the epoxy layer creates a hit. The optical surfaces of the SiPMs are defined using the `unified` model with the same parameters as were used for the aluminised mylar, but any model could be used that allows 100% detection. A realistic detection efficiency was included by using the detection efficiency curve of the SiPMs (Figure B.10) in post-processing the output from the simulation.

B.4.4 Physics list

The simulation uses three standard physics lists, which are `G4OpticalPhysics`, `G4EmStandardPhysics` and `G4DecayPhysics`. This means:

1. no nuclear interactions between scattered beam photons and nuclei;
2. no **nuclear** interactions between the recoiling ^{3}He and the surrounding gas (stoppage through EM interactions only).

In reality of course the scattered high-energy photons could have photonuclear reactions with the gas. However, these scenarios are currently not of interest (but may be of interest later for background studies). Additionally, the cross-sections are low and, despite the high pressure, the gas medium is not “dense” in terms of g/cm^2. Therefore the probability that the beam photon interacts twice inside the optically isolated volume is very low. The exclusion of the photonuclear interactions from the simulation should thus have a negligible effect on the behaviour of the high energy photons.

The electromagnetic forces are expected to dominate the interactions between the recoiling particle and the surrounding gas. The energies of the recoiling particles are too low for significant hadronic interactions. Thus the exclusion of the hadronic reactions is expected to have very little influence, especially in the context of the initial studies considered here.

Finally, the behaviour of the optical photons is fully covered by `G4OpticalPhysics`. This means that the scintillation collection efficiency analysis performed in the next subsection is not affected by the other physics lists.

B.5 Detector design assessment from initial simulation

After the simulation was implemented as described in Sections B.4.1 - B.4.4, initial feasibility studies of the new HeGSAT design were carried out. The three main questions were:

1. What percentage of the scintillation photons are detected?
2. How completely do the recoiling helium particles stop inside the gas volume?
3. Are enough photons detected per event to resolve the energy deposit of the recoiling particle?

These three questions are addressed in the three subsections below. The studies used ROOT v5.34.19 and Geant4 v4.10.00.

B.5.1 Scintillation collection efficiency

A simple ROOT based event generator macro was used to create 10^6 optical photons that were then processed through the Geant4 simulation. The photons were created into a volume box with coordinates $x = (-10\,\mathrm{mm}, 10\,\mathrm{mm})$, $y = (-10\,\mathrm{mm}, 10\,\mathrm{mm})$, $z = (50\mathrm{mm}, 60\mathrm{mm})$. The photon directions were chosen randomly, the photon energies were drawn randomly from the scintillation spectrum (Figure B.7). The chosen coordinate box represents a segment of the optically isolated volume along the photon beam where Compton scattering from ^{3}He can occur. Figure B.8 depicts the HeGSAT with the coordinate system used in the Geant4 simulation and the numbering convention of the SiPMs.

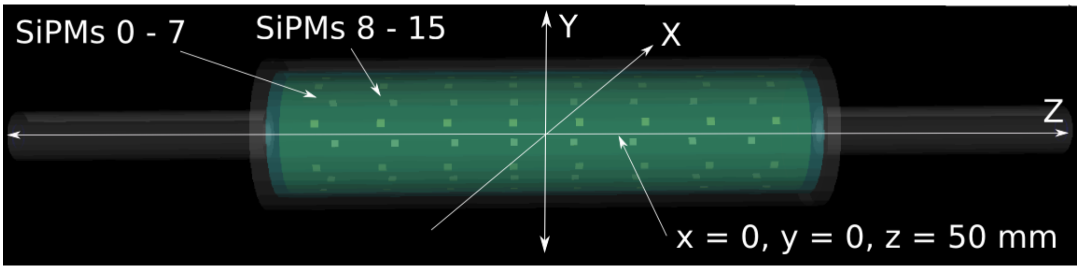

Figure B.8: Figure depicting the new HeGSAT simulation. The position of the box where the simulated optical photons of Section B.5.1 originate is shown. The numbering scheme of the SiPMs in the Geant4 simulation is indicated. The leftmost ring has SiPMs 0 - 7, the next ring 8 - 15, etc. up to the last ring with SiPMs 56 - 63.

Out of the 10^6 optical photons, about 26% reached a SiPM. This number depends mostly on the well known reflectively of PTFE. The fraction of detected photons was found to be 7.1% by taking into account the photon detection efficiency of the SiPMs at overvoltage 3.5 V (see Figure B.10). The percentages seen by individual SiPM rings[1]

---

[1] A ring of SiPMs that have the same z coordinate is meant. For instance SiPMs 0-7 are referred to as ring 1, 8-15 ring 2 etc. There are 8 rings all together. See also Figure B.8.

are plotted in Figure B.9. The SiPM rings closest to the photon source detected the largest fraction of the photons.

Figuratively speaking, the percentage of detected photons depends on the convolution of curves B.7 and B.10 multiplied by the PTFE reflectivity. The latter two are relatively well established and the dominant uncertainty comes from the scintillation spectrum. However, the end result is quite insensitive to this uncertainty. Using a uniform scintillation spectrum from 320 nm - 660 nm yields a total detection efficiency of 5.8%, meaning a change of about $\approx$ 20%.

The fact that the SiPM rings closest to the photon source see the largest fraction of the scintillation photons also implies that the position of the Compton scattering event in the optically isolated volume can be extracted by comparing the size of the signals from individual rings.

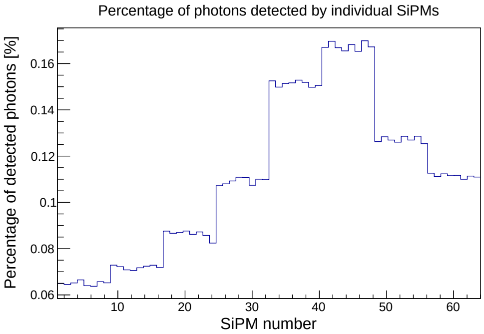

Figure B.9: Percentage of photons detected by individual SiPMs. In total 7.1% of the photons are detected. SiPM rings closest to the photon source (see Figure B.8) detect the largest fraction of the photons.

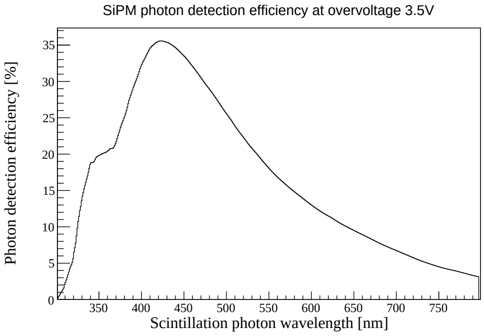

Figure B.10: SiPM photon detection efficiency at overvoltage 3.5 V [142].

An overall scintillation collection efficiency of 7.1% is close to the reported value of the previous HeGSAT design, which was $\approx$ 8%. The previous design has been successfully used for the total photo-absorption cross-section measurement of ^{4}He in Lund, Sweden [80]. The scintillation photon collection efficiency is a key feature of the design, therefore the value of 7.1% seems to suggest that the new design has comparable capabilities for the experiments relying on scintillation collection.

B.5.2 Recoiling particle stoppage efficiency

The extraction of the Compton scattering signal relies on the recoiling ^{3}He particles stopping inside the helium gas volume. In this case all the kinetic energy of the recoiling ^{3}He particle is “captured” by the surrounding gas. A fraction of that energy is converted to scintillation light, which is collected by the silicon photomultipliers. As a simple example, if a recoiling ^{3}He has a kinetic energy of 5 MeV and stops inside the gas volume, one expects to detect about 90 photons over all 64 SiPMs. If, however, the recoiling ^{3}He deposits 3 MeV in the gas, then hits the PTFE and deposits 2 MeV there, one will detect about 50 photons instead of 90. In the end, the size of the signal seen by the SiPMs is used to extract the energy deposit. In the latter case, 2 MeV will be missing. The Compton scattering signal is identified by selecting events where the missing energy is zero[2],

$$E_\gamma - E_{\gamma'} - E_{\text{recoil}} = 0. \tag{B.6}$$

In Eq. (B.6) E_γ and $E_{\gamma'}$ are the energies of the incident and scattered photon, respectively. E_{recoil} is the energy of the recoiling particles determined by the Active Target (in case of Compton scattering the energy of the recoiling $^3\text{He}'$). Therefore, in order to assess the feasibility of the Compton signal extraction, it is important to know whether the gas inside the optically isolated volume is dimensionally large enough and has high enough density to stop the recoiling ^{3}He particles before they reach the PTFE reflector.

To this end $5 \cdot 10^6$ Compton scattering events

$$\gamma + {}^3\text{He} \rightarrow \gamma' + {}^3\text{He}' \tag{B.7}$$

were processed through the simulation. The energies of the tagged photons incident on the target were sampled from a Bremsstrahlung spectrum in the energy range 50-200 MeV. The target ^{3}He was assumed at rest. The events were distributed evenly over the full z length of the optically isolated volume, $z = [-200\text{ mm}, 200\text{ mm}]$. The x and y coordinates of the events were distributed evenly over the cross-section of the beam spot, such that $x = [-10\text{ mm}, 10\text{ mm}]$ and $y = [-10\text{ mm}, 10\text{ mm}]$ with a constraint $\sqrt{x^2 + y^2} <= 10\text{ mm}$.

To get the exact energy deposit of the recoiling $^3\text{He}'$, the helium gas inside the optically isolated volume was turned into a *sensitive detector* (see Section 4.4.2 of Ref. [120]) in order to record the deposited energy. It should be noted that the analysis in this subsection does not make use of the optical properties of the simulation. The acceptance as studied here depends mainly on the material properties of the helium gas (density and isotope mass, both well known) and the actual geometry of the detector (dimensions of the optically isolated volume).

Simple analysis of the simulation results was then performed. It was demanded that

$$|E_\gamma - E_{\gamma'} - \text{Edep}_{\text{He3}'}| < 1\text{ MeV}, \tag{B.8}$$

$$\text{Edep}_{\text{He3}'} \geq 1\text{ MeV}. \tag{B.9}$$

In the equations above $\text{Edep}_{\text{He3}'}$ is the energy deposited inside the helium gas volume by the recoiling $^3\text{He}'$. Condition (B.8) demands that to be able to detect a Compton scattering event, the absolute value of the energy balance has to be less than 1 MeV. This is merely a statement saying that the Compton scattering events can be identified when the recoiling $^3\text{He}'$ deposits the bulk of its kinetic energy to the surrounding gas, and the scattered photon penetrates the pressure vessel to be detected by the Crystal Ball spectrometer. The second statement requires the energy deposited by the recoiling helium to be larger than 1 MeV. If the deposition is less than 1 MeV, too few scintillation photons will be detected to produce a signal above the SiPM noise level. The cut values (B.8) and (B.9) are in no way canonical, but rather represent starting-point values for the initial analysis.

Figure B.11 shows a 2-dimensional histogram of the HeGSAT acceptance for Compton scattering events within cuts (B.8), (B.9). The y-axis has the energy of the incoming beam particle γ, the x-axis has the angle of the scattered γ' ($\cos\theta = 1$ is the

---

[2] In practice a cut region is used, e.g. $E_{\text{miss}} = [-1\text{ MeV}, 1\text{ MeV}]$.

direction of the beam). There are two regions where the acceptance is very low. One of the regions is in the top-left corner of Figure B.11, a combination of high beam energy and backward scattered γ' photons. Due to backward scattering of the γ', the recoiling $^3\mathrm{He}'$ gains a large momentum along the beam direction and tends to hit the end PTFE wall of the optically isolated volume and deposit at least some of its energy there. Figure B.12 illustrates the stopping positions of the recoiling helium particles in the events outside the cuts (B.8) and (B.9). Many stop at coordinate $z = 200\,\mathrm{mm}$, which is the position of the PTFE end wall.

The second region where the acceptance is very low is the bottom-right corner of Figure B.11, at forward scattering angle and low beam energy. This region is associated with cut (B.9), in which case the recoiling $^3\mathrm{He}'$ gets too weak of a "kick" in the Compton scattering event. In this case the recoiling particle stops inside the gas, but the energy deposit is below 1 MeV due to low initial kinetic energy. In Figure B.12 the "tube" along the full z length of the optically isolated volume illustrates the stopping positions of the recoiling particles that have too low initial kinetic energy.

It should be noted that the present analysis only studies the HeGSAT and does not aim to make predictions for the acceptance using the full experimental apparatus. This means that in Eq. (B.8) it has been assumed that the energy of the incoming γ is known exactly. The energy of the scattered γ' is also assumed to be known exactly, given that it escapes the pressure vessel. If, instead, it reacts with the aluminium and e.g. decays through $\gamma \to e^+e^-$, the event is not accepted as a Compton event.

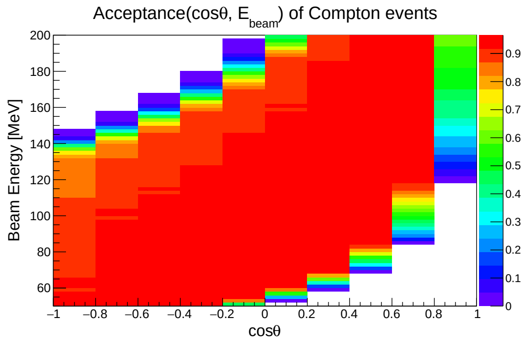

Figure B.11: HeGSAT detector acceptance of Compton events dependence on the incident beam energy and the angle of the scattered γ'. Energy bin width 2 MeV, $\cos\theta$ bin width 0.2.

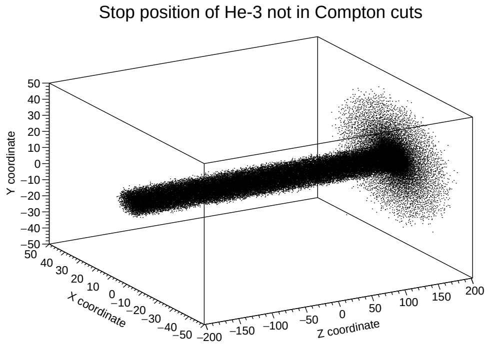

Figure B.12: Stop positions of recoiling $^3\mathrm{He}'$ that are not inside Compton cuts (B.8) and (B.9).

The acceptance presented in this analysis is consistent with that in the experimental proposal [137]. The loss of backward angles at higher beam energies and the loss of forward angles at lower beam energies is expected. The fact that there are no angle-regions completely uncovered is positive. From comparison with fully covered regions, extrapolation techniques might allow insight into the experimentally inaccessible areas. The analysis presented in this subsection was also used to reduce the radius of the target. The original drawing specified a PTFE cylinder radius of 95 mm. During the acceptance studies it was noticed that the radial travel of the recoiling particles with respect to the z-axis (beam direction) is significantly less than that. Through testing different radii, it was decided to reduce the inner radius of the PTFE cylinder to 46 mm. When it was reduced to less than 40 mm, one could see that the recoiling particles also started to hit the PTFE cylinder as well as the end wall of the optically isolated volume. Reducing the radius is beneficial because it reduces the amount of helium gas required and, even more importantly, increases the scintillation photon collection efficiency (better SiPM surface to reflector surface ratio).

B.5.3 Energy resolution

The simulation was used to study the detector capability for event-by-event analysis. The fundamental question is how well can one extract the energy deposition by the recoiling $^3\mathrm{He}'$ by collecting scintillation photons per event. The analysis in this subsection makes use of all the optical properties described in B.4.3 and also includes the scintillation yield. This is unlike the analyses presented in the two previous subsections. The scintillation collection efficiency study used the scintillation spectrum but not the yield. In that case the optical photons were generated as primary particles, as opposed to being generated through the scintillation process. The recoil stopping efficiency study did not make use of the optical properties, but relied on the detector geometry and on the material properties of the helium gas.

To study the correlation between the energy deposition and the number of detected photons, $0.5 \cdot 10^6$ Compton scattering events were processed through the Geant4 simulation with two different settings. In the first case the full optical simulation was used with silicon photomultipliers as sensitive detectors. Each of the $0.5 \cdot 10^6$ Compton events resulted in creating some distribution of detected scintillation photons over the 64 SiPMs. In the second case the helium gas volume was set as the sensitive detector and the optical simulation was not used. This gave the energy deposit by the recoiling $^3\mathrm{He}'$ in each of the $0.5 \cdot 10^6$ Compton events. The two different runs were linked event-by-event, so that from the optical run one got the number of detected photons, from the other run one got the exact energy deposit of the recoiling particle.

A Simple analysis of the simulation output was performed. Detectable Compton scattering events were identified by cuts

$$|\mathrm{E}_\gamma - \mathrm{E}_{\gamma'} - \mathrm{Edep}_{\mathrm{He3}'}| < 1\,\mathrm{MeV}, \tag{B.10}$$

$$\#\,\text{of detected photons} \geq 10. \tag{B.11}$$

Note the change between Eqs. (B.11) and (B.9). Cut (B.11) reflects the actual experimental set-up more accurately, as in the end one will need to decide whether the deposited energy can be resolved based on the signal seen by the SiPMs. Of course, for more realistic results the quantity $\mathrm{Edep}_{\mathrm{He3}'}$ in (B.10) should also be extracted by using the number of detected photons and the linear correspondence from Figure B.13. However, with the large uncertainty associated with the scintillation yield such an analysis is impractical at this stage.

The correlation between the energy deposit by the recoiling particle and the number of detected photons is depicted in Figure B.13. As one might expect, there is an almost linear correspondence between the energy deposit and the number of detected photons. A projection of the histogram in Figure B.13 along the x-axis is shown in Figure B.14 for events with an energy deposit (2.1 ± 0.1) MeV. At an energy deposit of 2 MeV the average number of detected scintillation photons is ≈ 37 with $\sigma \approx 6$. At 1 MeV, the corresponding values are ≈ 20 and $\sigma \approx 4.5$. This shows that the energy resolution is ~0.5 MeV at 95% confidence level (2σ). However, this result is highly dependent on the scintillation yield and has been obtained with simplifications (e.g. assumption of the exact values in cut (B.10)). It is likely that a 0.5 MeV energy resolution is an overestimate of the accuracy, yet the order of magnitude gives grounds for optimism towards the detector design.

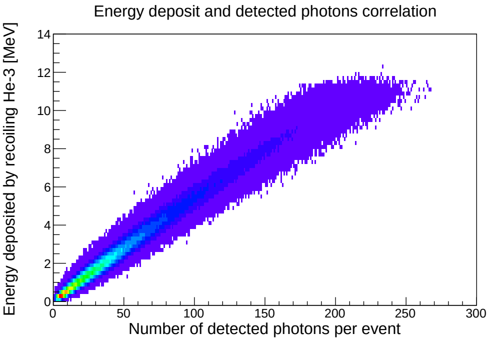

Figure B.13: Energy deposit of the recoiling particle versus the number of detected photons in an event. Energy bin width 0.2 MeV, nr. of photon bin width 1.

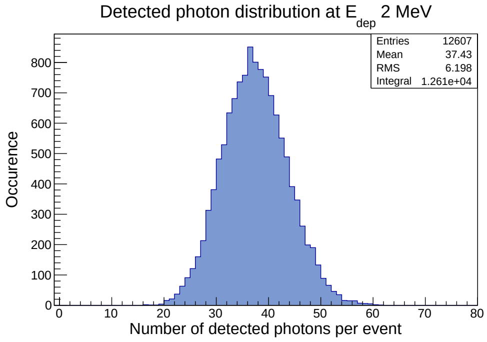

Figure B.14: Number of detected photons distribution over the Compton scattering events where the energy deposit by the recoiling particle is (2.1 ± 0.1) MeV.

B.6 Summary and outlook of new HeGSAT development

The results presented in Section B.5 suggest that the new HeGSAT design is suitable for the planned Compton scattering measurement on ^{3}He. However, the results are preliminary and especially the uncertainty associated with the scintillation yield needs to be addressed. At the time of writing the building of the pressure vessel of the new HeGSAT is being planned in Mainz, Germany. After the important parameters of the simulation are calibrated against experiments with this detector, the simulation should provide a very useful tool to help analyse the experimental results.

After the analysis presented in this appendix a further improvement to the design has emerged. It is in the planning to increase the number of SiPMs from 64 to 256. This is expected to increase the scintillation collection efficiency approximately by a factor of 4 from $\sim 7\%$ to $\sim 28\%$ and improve the projected energy resolution of the new HeGSAT. The improved design of the new HeGSAT that resulted from the analysis presented in this appendix is depicted in Figure B.15.

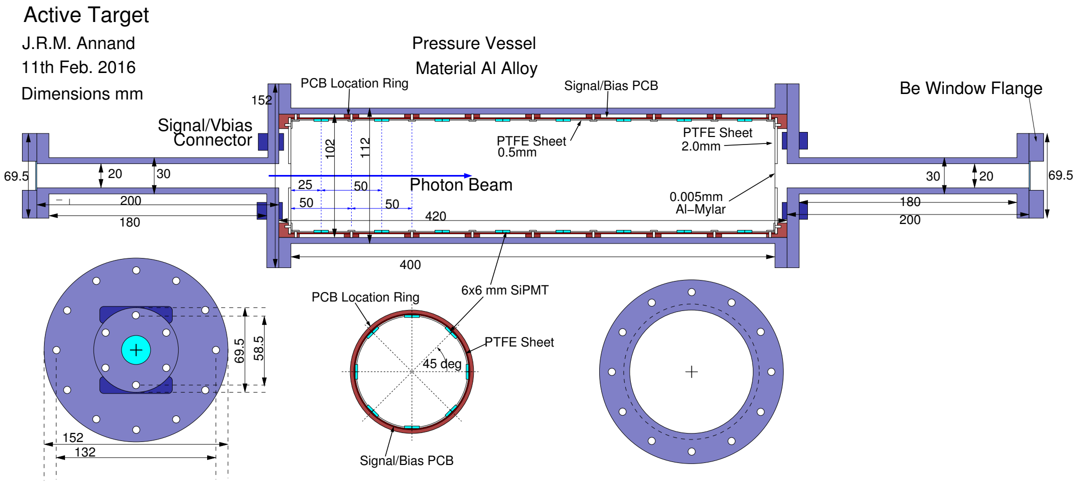

8 rings of SiPMT, each ring consisting 8 groups of 4 6x6mm tiles.
Total number of SiPMT 8x8x4 = 256.
Readout in groups of 16, each group connected to an op–amp.
16 signal outputs
2 vias–voltage inputs

Figure B.15: The improved new HeGSAT design by Annand in February 2016. The number of SiPMs has been increased from 64 to 256 and the inner diameter of the pressure vessel has been decreased from 200 mm to 102 mm (cf. Figure B.2).

Bibliography

[1] M. Hilt, S. Scherer, and L. Tiator. "Threshold π^0 photoproduction in relativistic chiral perturbation theory". *Phys. Rev. C* 87 (2013), p. 045204. DOI: `10.1103/PhysRevC.87.045204`.

[2] P. De Baenst. "An improvement on the Kroll-Ruderman theorem". *Nucl. Phys. B* 24 (1970), p. 633. DOI: `10.1016/0550-3213(70)90451-7`.

[3] G. F. Chew et al. "Relativistic Dispersion Relation Approach to Photomeson Production". *Phys. Rev.* 106 (1957), p. 1345. DOI: `10.1103/PhysRev.106.1345`.

[4] J. S. Ball. "Application of the Mandelstam Representation to Photoproduction of Pions from Nucleons". *Phys. Rev.* 124 (1961), p. 2014. DOI: `10.1103/PhysRev.124.2014`.

[5] D. Drechsel and L. Tiator. "Threshold pion photoproduction on nucleons". *J. Phys. G* 18 (1992), p. 449. DOI: `10.1088/0954-3899/18/3/004`.

[6] M. Hilt et al. "Pion photo- and electroproduction in relativistic baryon chiral perturbation theory and the chiral MAID interface". *Phys. Rev. C* 88 (2013), p. 055207. DOI: `10.1103/PhysRevC.88.055207`.

[7] W. B. Jensen. "The Origin of the s, p, d, f Orbital Labels". *J. Chem. Educ.* 84 (2007), p. 757.

[8] O. Hanstein, D. Drechsel, and L. Tiator. "A dispersion theoretical approach to the threshold amplitudes of pion photoproduction". *Phys. Lett. B* 399 (1997), p. 13. DOI: `10.1016/S0370-2693(97)00272-4`.

[9] G. Ecker and U.-G. Meissner. "What is a low-energy theorem?" *Comments Nucl. Part. Phys.* 21 (1995), p. 347. arXiv: `hep-ph/9409442 [hep-ph]`.

[10] M. Gell-Mann and M. L. Goldberger. "Scattering of Low-Energy Photons by Particles of Spin 1/2". *Phys. Rev.* 96 (1954), p. 1433. DOI: `10.1103/PhysRev.96.1433`.

[11] F. E. Low. "Scattering of Light of Very Low Frequency by Systems of Spin 1/2". *Phys. Rev.* 96 (1954), p. 1428. DOI: `10.1103/PhysRev.96.1428`.

[12] N. M. Kroll and M. A. Ruderman. "A Theorem on Photomeson Production near Threshold and the Suppression of Pairs in Pseudoscalar Meson Theory". *Phys. Rev.* 93 (1954), p. 233. DOI: `10.1103/PhysRev.93.233`.

[13] E. Mazzucato et al. "Precise measurement of neutral-pion photoproduction on the proton near threshold". *Phys. Rev. Lett.* 57 (1986), p. 3144. DOI: `10.1103/PhysRevLett.57.3144`.

[14] R. Beck et al. “Measurement of the $p(\gamma, \pi^0)$ cross section at threshold”. *Phys. Rev. Lett.* 65 (1990), p. 1841. DOI: `10.1103/PhysRevLett.65.1841`.

[15] S. Weinberg. *The Quantum Theory of Fields.* Vol. 1. Cambridge University Press, 1995. DOI: `10.1017/CBO9781139644167`.

[16] M. Gell-Mann, M. L. Goldberger, and W. E. Thirring. “Use of Causality Conditions in Quantum Theory”. *Phys. Rev.* 95 (1954), p. 1612. DOI: `10.1103/PhysRev.95.1612`.

[17] M. L. Goldberger. “Causality Conditions and Dispersion Relations. I. Boson Fields”. *Phys. Rev.* 99 (1955), p. 979. DOI: `10.1103/PhysRev.99.979`.

[18] M. L. Goldberger, H. Miyazawa, and R. Oehme. “Application of Dispersion Relations to Pion-Nucleon Scattering”. *Phys. Rev.* 99 (1955), p. 986. DOI: `10.1103/PhysRev.99.986`.

[19] O. Hanstein, D. Drechsel, and L. Tiator. “Multipole analysis of pion photoproduction based on fixed t dispersion relations and unitarity”. *Nucl. Phys. A* 632 (1998), p. 561. DOI: `10.1016/S0375-9474(98)00818-5`.

[20] D. Drechsel, B. Pasquini, and L. Tiator. “A dispersive approach to pion photo- and electroproduction”. *Few-Body Syst.* 41 (2007), p. 13. DOI: `10.1007/s00601-007-0184-4`.

[21] Y. Nambu. “Axial Vector Current Conservation in Weak Interactions”. *Phys. Rev. Lett.* 4 (1960), p. 380. DOI: `10.1103/PhysRevLett.4.380`.

[22] Y. Nambu and G. Jona-Lasinio. “Dynamical Model of Elementary Particles Based on an Analogy with Superconductivity. I”. *Phys. Rev.* 122 (1961), p. 345. DOI: `10.1103/PhysRev.122.345`.

[23] J. Goldstone. “Field theories with <<Superconductor>> solutions”. *Nuovo Cimento* 19 (1961), p. 154. DOI: `10.1007/BF02812722`.

[24] J. Goldstone, A. Salam, and S. Weinberg. “Broken Symmetries”. *Phys. Rev.* 127 (1962), p. 965. DOI: `10.1103/PhysRev.127.965`.

[25] S. Weinberg. “Dynamical Approach to Current Algebra”. *Phys. Rev. Lett.* 18 (1967), p. 188. DOI: `10.1103/PhysRevLett.18.188`.

[26] S. Weinberg. “Phenomenological Lagrangians”. *Physica A* 96 (1979), p. 327. DOI: `10.1016/0378-4371(79)90223-1`.

[27] J. Gasser and H. Leutwyler. “Chiral perturbation theory to one loop”. *Ann. Phys. (N.Y.)* 158 (1984), p. 142. DOI: `10.1016/0003-4916(84)90242-2`.

[28] J. Gasser, M. E. Sainio, and A. Švarc. “Nucleons with chiral loops”. *Nucl. Phys. B* 307 (1988), p. 779. DOI: `10.1016/0550-3213(88)90108-3`.

[29] S. Scherer. “Introduction to chiral perturbation theory”. *Adv. Nucl. Phys.* 27 (2003), p. 277. arXiv: `hep-ph/0210398 [hep-ph]`.

[30] S. Scherer and M. R. Schindler. “A Primer for Chiral Perturbation Theory”. *Lect. Notes Phys.* 830 (2012), pp.1. DOI: `10.1007/978-3-642-19254-8`.

[31] B. Strandberg. “Low-energy processes with three pions in the final state”. MA thesis. Uppsala University, 2012. URL: `http://urn.kb.se/resolve?urn=urn:nbn:se:uu:diva-175774`.

[32] M. Gell-Mann. “Symmetries of Baryons and Mesons”. *Phys. Rev.* 125 (1962), p. 1067. DOI: `10.1103/PhysRev.125.1067`.

[33] J. A. McGovern, D. R. Phillips, and H. W. Grießhammer. “Compton scattering from the proton in an effective field theory with explicit Delta degrees of freedom”. *Eur. Phys. J. A* 49 (2013), p. 12. DOI: `10.1140/epja/i2013-13012-1`.

[34] G. Colangelo et al. “Review of lattice results concerning low energy particle physics”. *Eur. Phys. J. C* 71 (2011), p. 1695. DOI: `10.1140/epjc/s10052-011-1695-1`.

[35] S. R. Beane et al. “$SU(2)$ low-energy constants from mixed-action lattice QCD”. *Phys. Rev. D* 86 (2012), p. 094509. DOI: `10.1103/PhysRevD.86.094509`.

[36] Chiral MAID web interface. URL: `https://maid.kph.uni-mainz.de//chiralmaid/`.

[37] V. Bernard, N. Kaiser, and U.-G. Meißner. “Chiral corrections to the Kroll-Ruderman theorem”. *Phys. Lett. B* 383 (1996), p. 116. DOI: `10.1016/0370-2693(96)00699-5`.

[38] A. Gasparyan and M. F. M. Lutz. “Photon- and pion-nucleon interactions in a unitary and causal effective field theory based on the chiral Lagrangian”. *Nucl. Phys. A* 848 (2010), p. 126. DOI: `10.1016/j.nuclphysa.2010.08.006`.

[39] R. A. Arndt et al. “Partial-wave analysis of pion photoproduction”. *Phys. Rev. C* 42 (1990), p. 1853. DOI: `10.1103/PhysRevC.42.1853`.

[40] SAID web interface. URL: `http://gwdac.phys.gwu.edu/`.

[41] R. G. Moorhouse, H. Oberlack, and A. H. Rosenfeld. “Analysis of π^+, π^-, and π^0 photoproduction from the first through the third resonance region”. *Phys. Rev. D* 9 (1974), p. 1. DOI: `10.1103/PhysRevD.9.1`.

[42] R. L. Walker. “Phenomenological Analysis of Single-Pion Photoproduction”. *Phys. Rev.* 182 (1969), p. 1729. DOI: `10.1103/PhysRev.182.1729`.

[43] V. E. Tarasov et al. “Extracting the photoproduction cross sections off the neutron, via the $\gamma n \to \pi^- p$ reaction, from deuteron data with final-state interaction effects”. *Phys. Rev. C* 84 (2011), p. 035203. DOI: `10.1103/PhysRevC.84.035203`.

[44] V. Lensky et al. “Precision calculation of $\gamma\mathrm{d} \to \pi\mathrm{nn}$ within chiral perturbation theory”. *Eur. Phys. J. A* 26 (2005), p. 107. DOI: `10.1140/epja/i2005-10154-7`.

[45] V. Lensky. Personal communication. 2017.

[46] M. Fuchs et al. “Neutral pion photoproduction from the proton near threshold”. *Phys. Lett. B* 368 (1996), p. 20. DOI: `10.1016/0370-2693(95)01488-8`.

[47] J. C. Bergstrom et al. “Measurement of the ^{1}H(γ, π^0) cross section near threshold”. *Phys. Rev. C* 53 (1996), p. 1052. DOI: `10.1103/PhysRevC.53.R1052`.

[48] J. C. Bergstrom, R. Igarashi, and J. M. Vogt. “Measurement of the ^{1}H(γ, π^0) cross section near threshold. II. Pion angular distributions”. *Phys. Rev. C* 55 (1997), p. 2016. DOI: `10.1103/PhysRevC.55.2016`.

[49] J. C. Bergstrom. “Measurement of the ^{1}H(γ, π^0) cross section near threshold. III. Angular coefficients”. *Phys. Rev. C* 58 (1998), p. 2574. DOI: `10.1103/PhysRevC.58.2574`.

[50] D. Hornidge et al. “Accurate Test of Chiral Dynamics in the $\vec{\gamma}p \to \pi^0 p$ Reaction”. *Phys. Rev. Lett.* 111 (2013), p. 062004. DOI: `10.1103/PhysRevLett.111.062004`.

[51] V. Rossi et al. “Analysis of the reaction γ+n$\to$p+π^- in the first and second resonance regions”. *Nuovo Cimento A* 13 (1973), p. 59. DOI: `10.1007/BF02788907`.

[52] G. Gialanella et al. “Analysis of the reaction γ+p $\to$ p+π^++π^- at energies up to 1 GeV in a hydrogen bubble chamber”. *Nuovo Cimento A* 63 (1969), p. 892. DOI: `10.1007/BF02760745`.

[53] M. Salomon et al. “Radiative capture and charge exchange of negative pions on protons at 26.4 and 39.3 MeV”. *Nucl. Phys. A* 414 (1984), p. 493. DOI: `10.1016/0375-9474(84)90615-8`.

[54] TRIUMF. Canada’s national laboratory for particle and nuclear physics and accelerator-based science. URL: `http://www.triumf.ca/`.

[55] H. W. Fearing et al. “Charged radiative pion capture on the nucleon in heavy baryon chiral perturbation theory”. *Nucl. Phys. A* 684 (2001), p. 377. DOI: `10.1016/S0375-9474(01)00399-2`.

[56] A. Bagheri et al. “Reaction π^-p$\to\gamma$n below the Δ resonance”. *Phys. Rev. C* 38 (1988), p. 875. DOI: `10.1103/PhysRevC.38.875`.

[57] M. Wang. PhD thesis. University Of Kentucky, 1992.

[58] K. Liu. “Radiative Negative Pion Proton Capture and the Low Energy Theorem”. PhD thesis. University Of Kentucky, 1994.

[59] A. H. Compton. “A Quantum Theory of the Scattering of X-rays by Light Elements”. *Phys. Rev.* 21 (1923), p. 483. DOI: `10.1103/PhysRev.21.483`.

[60] M. Goldhaber and E. Teller. “On Nuclear Dipole Vibrations”. *Phys. Rev.* 74 (1948), p. 1046. DOI: `10.1103/PhysRev.74.1046`.

[61] E. R. Gaerttner and M. L. Yeater. “Note on the Resonance Scattering of High Energy γ-Rays by Nuclei of Carbon and Copper”. *Phys. Rev.* 76 (1949), p. 363. DOI: `10.1103/PhysRev.76.363`.

[62] M.-T. Hütt et al. “Compton scattering by nuclei”. *Phys. Rep.* 323 (2000), p. 457. DOI: `10.1016/S0370-1573(99)00041-1`.

[63] D. Drechsel, B. Pasquini, and M. Vanderhaeghen. “Dispersion relations in real and virtual Compton scattering”. *Phys. Rep.* 378 (2003), p. 99. DOI: `10.1016/S0370-1573(02)00636-1`.

[64] M. Schumacher. “Polarizability of the nucleon and Compton scattering”. *Prog. Part. Nucl. Phys.* 55 (2005), p. 567. DOI: `10.1016/j.ppnp.2005.01.033`.

[65] H. W. Grießhammer et al. “Using Effective Field Theory to analyse low-energy Compton scattering data from protons and light nuclei”. *Prog. Part. Nucl. Phys.* 67 (2012), p. 841. DOI: `10.1016/j.ppnp.2012.04.003`.

[66] P. P. Martel. “Measuring Proton Spin Polarizabilities With Polarized Compton Scattering”. PhD thesis. University of Massachusetts Amherst, 2013. URL: `https://wwwa2.kph.uni-mainz.de/images/publications/phd/pmartel_dis.pdf`.

[67] R. P. Hildebrandt. “Elastic Compton Scattering from the Nucleon and Deuteron”. PhD thesis. Technische Universität München, 2005. URL: `http://www.t39.ph.tum.de/T39_files/T39_people_files/PhDThesis/hildebrandt.pdf`.

[68] H. W. Grießhammer and T. R. Hemmert. “Dispersion effects in nucleon polarizabilities”. *Phys. Rev. C* 65 (2002), p. 045207. DOI: `10.1103/PhysRevC.65.045207`.

[69] R. E. Prange. “Dispersion Relations for Compton Scattering”. *Phys. Rev.* 110 (1958), p. 240. DOI: `10.1103/PhysRev.110.240`.

[70] L. S. Myers et al. “Measurement of Compton Scattering from the Deuteron and an Improved Extraction of the Neutron Electromagnetic Polarizabilities”. *Phys. Rev. Lett.* 113 (2014), p. 262506. DOI: `10.1103/PhysRevLett.113.262506`.

[71] L. S. Myers et al. “Compton scattering from the deuteron below pion-production threshold”. *Phys. Rev. C* 92 (2015), p. 025203. DOI: `10.1103/PhysRevC.92.025203`.

[72] C. Patrignani et al. “Review of Particle Physics”. *Chin. Phys. C* 40 (2016), p. 100001. DOI: `10.1088/1674-1137/40/10/100001`.

[73] R. P. Hildebrandt et al. “Signatures of chiral dynamics in low-energy Compton scattering off the nucleon”. *Eur. Phys. J. A* 20 (2004), p. 293. DOI: `10.1140/epja/i2003-10144-9`.

[74] R. P. Hildebrandt, H. W. Grießhammer, and T. R. Hemmert. “Spin polarizabilities of the nucleon from polarized low-energy Compton scattering”. *Eur. Phys. J. A* 20 (2004), p. 329. DOI: `10.1140/epja/i2003-10154-7`.

[75] R. P. Hildebrandt, H. W. Grießhammer, and T. R. Hemmert. “Nucleon polarizabilities from deuteron Compton scattering within a Green’s function hybrid approach”. *Eur. Phys. J. A* 46 (2010), p. 111. DOI: `10.1140/epja/i2010-11024-y`.

[76] D. Choudhury, A. Nogga, and D. R. Phillips. “Investigating Neutron Polarizabilities through Compton Scattering on ^{3}He”. *Phys. Rev. Lett.* 98 (2007), p. 232303. DOI: `10.1103/PhysRevLett.98.232303`.

[77] D. Shukla, A. Nogga, and D. R. Phillips. “Analyzing the effects of neutron polarizabilities in elastic Compton scattering off ^{3}He”. *Nucl. Phys. A* 819 (2009), p. 98. DOI: `10.1016/j.nuclphysa.2009.01.003`.

[78] D. Choudhury. “Investigating Neutron Polarizabilities and NN Scattering In Heavy-Baryon Chiral Perturbation Theory”. PhD thesis. Ohio University, 2006. URL: `https://etd.ohiolink.edu/ap/10?0::NO:10:P10_ACCESSION_NUM:ohiou1163711618`.

[79] R. Al Jebali. “Measurement of the $\gamma + {}^4$He Total Photoabsorption Cross-Section using a Gas-Scintillator Active Target”. PhD thesis. The University of Glasgow, 2013. URL: `http://nuclear.gla.ac.uk/npe-theses/AlJebali_thesis.pdf`.

[80] R. Al Jebali et al. “A helium gas scintillator active target for photoreaction measurements”. *Eur. Phys. J. A* 51 (2015), p. 123. DOI: `10.1140/epja/i2015-15123-y`.

[81] A2 Collaboration at Johannes Gutenberg-Universität Mainz. URL: `http://wwwa2.kph.uni-mainz.de/`.

[82] A. Tenore and A. Verganelakis. “Elastic photon-deuteron scattering and the nucleon polarizability”. *Nuovo Cimento* 35 (1965), p. 261. DOI: `10.1007/BF02734837`.

[83] M. A. Lucas. “Compton Scattering from the Deuteron at Intermediate Energies”. PhD thesis. University Of Illinois At Urbana-Champaign, 1994.

[84] D. L. Hornidge et al. “Elastic Compton Scattering from the Deuteron and Nucleon Polarizabilities”. *Phys. Rev. Lett.* 84 (2000), p. 2334. DOI: `10.1103/PhysRevLett.84.2334`.

[85] D. L. Hornidge. “Elastic Photon Scattering From Deuterium”. PhD thesis. University Of Saskatchewan, 1999. URL: `http://nucleus.usask.ca/technical_reports/theses/Hornidge-thesis.pdf`.

[86] M. Lundin et al. “Compton Scattering from the Deuteron and Extracted Neutron Polarizabilities”. *Phys. Rev. Lett.* 90 (2003), p. 192501. DOI: `10.1103/PhysRevLett.90.192501`.

[87] M. Lundin. “Compton Scattering from the Deuteron at Low Energies”. `https://www.maxlab.lu.se/sites/default/files/lundin.pdf`. PhD thesis. Lund University, 2002.

[88] L. S. Myers. “Deuteron Compton Scattering Below Pion Threshold”. PhD thesis. University of Illinois at Urbana-Champaign, 2010. URL: `https://www.ideals.illinois.edu/handle/2142/18332`.

[89] J.-O. Adler et al. “The upgraded photon tagging facility at the MAX IV Laboratory”. *Nucl. Instrum. Meth. Phys. Res. A* 715 (2013), p. 1. DOI: `10.1016/j.nima.2013.02.040`.

[90] M. Eriksson. “The MAX-lab Story; From Microtron to MAX IV”. *Proceedings of IPAC 2014*. URL: `http://jacow.org/IPAC2014/papers/thppa03.pdf`.

[91] K. Fissum. *Near-threshold Photoproduction of* π^-. Experimental proposal, 2008. URL: `https://www.maxlab.lu.se/sites/default/files/nuclear_proposal08-01.pdf`.

[92] G. Feldman. *Compton Scattering from Deuterium above the Pion Production Threshold.* Experimental proposal, 2010. URL: `https://www.maxlab.lu.se/sites/default/files/nuclear_pac_2010_proposal_10-02.pdf`.

[93] J.-O. Adler et al. "The photon tagging facility at the max accelerator system in Lund". *Nucl. Instrum. Meth. Phys. Res. A* 294 (1990), p. 15. DOI: `10.1016/0168-9002(90)91823-T`.

[94] J.-O. Adler et al. "A broad range tagging spectrometer for the MAX-laboratory". *Nucl. Instrum. Meth. Phys. Res. A* 388 (1997), p. 17. DOI: `10.1016/S0168-9002(97)00347-1`.

[95] K. Hansen. Personal communication. 2016.

[96] Lund tagger online documentation. URL: `https://www.maxlab.lu.se/sites/default/files/nuclear_ET.pdf`.

[97] J. M. Vogt et al. "The photon tagging facility at the Saskatchewan Accelerator Laboratory". *Nucl. Instrum. Meth. Phys. Res. A* 324 (1993), p. 198. DOI: `10.1016/0168-9002(93)90977-P`.

[98] J. P. Miller et al. "Development of a NaI(Tl) detector with superior photon energy resolution for use above 100 MeV". *Nucl. Instrum. Meth. Phys. Res. A* 270 (1988), p. 431. DOI: `10.1016/0168-9002(88)90711-5`.

[99] A. Hünger et al. "Compton scattering by the proton through $\theta_{cms} = 75°$ and $90°$ in the Δ-resonance region". *Nucl. Phys. A* 620 (1997), p. 385. DOI: `10.1016/S0375-9474(97)00184-X`.

[100] V. L. Highland et al. "Branching ratios for stopped pions in deuterium". *Nucl. Phys. A* 365 (1981), p. 333. DOI: `10.1016/0375-9474(81)90395-X`.

[101] D. W. Joseph. "Electron Pair Production in $\pi^- + d$ Capture". *Phys. Rev.* 119 (1960), p. 805. DOI: `10.1103/PhysRev.119.805`.

[102] R. MacDonald et al. "Charge Exchange of Stopped π^- in Deuterium: Experiment and Theory". *Phys. Rev. Lett.* 38 (1977), p. 746. DOI: `10.1103/PhysRevLett.38.746`.

[103] S. Tripathi et al. "Double radiative pion capture on hydrogen and deuterium and the nucleon's pion cloud". *Phys. Rev. C* 75 (2007), p. 064603. DOI: `10.1103/PhysRevC.75.064603`.

[104] J. A. Bistirlich et al. "Photon Spectra from Radiative Absorption of Pions in Nuclei". *Phys. Rev. C* 5 (1972), p. 1867. DOI: `10.1103/PhysRevC.5.1867`.

[105] J. E. Amaro, A. M. Lallena, and J. Nieves. "Radiative pion capture in nuclei: a continuum shell-model approach". *Nucl. Phys. A* 623 (1997), p. 529. DOI: `10.1016/S0375-9474(97)00187-5`.

[106] B. Gabioud et al. "$n - n$ Scattering Length from the Photon Spectra of the Reactions $\pi^- d \to \gamma$nn and $\pi^- p \to \gamma n$". *Phys. Rev. Lett.* 42 (1979), p. 1508. DOI: `10.1103/PhysRevLett.42.1508`.

[107] J. Allison et al. "Recent developments in Geant4". *Nucl. Instrum. Meth. Phys. Res. A* 835 (2016), p. 186. DOI: `10.1016/j.nima.2016.06.125`.

[108] M. F. Preston. “Nuclear Compton scattering from ^{12}C”. MA thesis. Lund University, 2014. URL: `http://lup.lub.lu.se/student-papers/record/4465998`.

[109] B. Schröder. Personal communication. 2016.

[110] W. R. Gibbs, B. F. Gibson, and G. J. Stephenson, Jr. “Extraction of a_{nn} from the reaction $\pi^{-}d \rightarrow \gamma\mathrm{nn}$”. *Phys. Rev. C* 11 (1975), p. 90. DOI: `10.1103/PhysRevC.11.90`.

[111] W. R. Gibbs. Personal communication. 2016.

[112] D. A. Jenkins, P. T. Debevec, and P. D. Harty. “$^{2}\mathrm{H}(\gamma,p)n$ cross section between 20 and 440 MeV”. *Phys. Rev. C* 50 (1994), p. 74. DOI: `10.1103/PhysRevC.50.74`.

[113] W. Verkerke and D. Kirkby. “The RooFit toolkit for data modeling”. *eConf* C0303241 (2003). arXiv: `physics/0306116 [physics]`.

[114] R. Brun and F. Rademakers. “ROOT - An object oriented data analysis framework”. *Nucl. Instrum. Meth. Phys. Res. A* 389 (1997), p. 81. DOI: `10.1016/S0168-9002(97)00048-X`.

[115] F. James and M. Roos. “Minuit: A System for Function Minimization and Analysis of the Parameter Errors and Correlations”. *Comput. Phys. Commun.* 10 (1975), p. 343. DOI: `10.1016/0010-4655(75)90039-9`.

[116] W. Verkerke and D. Kirkby. RooFit user manual 2.91. URL: `https://root.cern.ch/download/doc/RooFit_Users_Manual_2.91-33.pdf`.

[117] K. Kossert et al. “Neutron Polarizabilities Investigated by Quasifree Compton Scattering from the Deuteron”. *Phys. Rev. Lett.* 88 (2002), p. 162301. DOI: `10.1103/PhysRevLett.88.162301`.

[118] National Institute of Standards and Technology. Physical Measurement Laboratory. URL: `https://www.nist.gov/pml`.

[119] M. Meshkian. “Photon-Tagging Measurements at MAX-lab”. MA thesis. Lund University, 2012. URL: `http://lup.lub.lu.se/student-papers/record/3158631`.

[120] Geant4 User’s Guide for Application Developers. URL: `http://geant4.web.cern.ch/geant4/UserDocumentation/UsersGuides/ForApplicationDeveloper/html/index.html`.

[121] V. Tarasov. Personal communication. 2016.

[122] `TSpectrum` class documentation. URL: `https://root.cern.ch/doc/v608/classTSpectrum.html`.

[123] M. Morháč et al. “Background elimination methods for multidimensional coincidence γ-ray spectra”. *Nucl. Instrum. Meth. Phys. Res. A* 401 (1997), p. 113. DOI: `10.1016/S0168-9002(97)01023-1`.

[124] C. V. Hampton, B. Lian, and W. C. McHarris. “Fast-Fourier-transform spectral enhancement techniques for γ-ray spectroscopy”. *Nucl. Instrum. Meth. Phys. Res. A* 353 (1994), p. 280. DOI: `10.1016/0168-9002(94)91657-8`.

[125] W. R. Gibbs, B. F. Gibson, and G. J. Stephenson, Jr. "Threshold charged-pion photoproduction and radiative pion capture. I. The Nucleon". *Phys. Rev. C* 16 (1977), p. 322. DOI: `10.1103/PhysRevC.16.322`.

[126] W. R. Gibbs, B. F. Gibson, and G. J. Stephenson, Jr. "Threshold charged-pion photoproduction and radiative pion capture. II. $\pi^- d \to \gamma$nn". *Phys. Rev. C* 16 (1977), p. 327. DOI: `10.1103/PhysRevC.16.327`.

[127] W. Tornow et al. "Scattering length measurements from radiative pion capture and neutron-deuteron breakup". *Nucl. Phys. A* 631 (1998), p. 421. DOI: `10.1016/S0375-9474(98)00040-2`.

[128] Q. Chen et al. "Measurement of the neutron-neutron scattering length using the $\pi^- d$ capture reaction". *Phys. Rev. C* 77 (2008), p. 054002. DOI: `10.1103/PhysRevC.77.054002`.

[129] G. F. de Téramond. "Final-state interactions and neutron-neutron scattering parameters". *Phys. Rev. C* 16 (1977), p. 1976. DOI: `10.1103/PhysRevC.16.1976`.

[130] G. F. de Téramond, J. Páez, and C. W. Soto Vargas. "Off-shell rescattering effects in the reaction $\pi^- + d \to 2n + \gamma$". *Phys. Rev. C* 21 (1980), p. 2542. DOI: `10.1103/PhysRevC.21.2542`.

[131] B. Gabioud et al. "nn Scattering parameters a_{nn} and r_{nn} from the photon spectrum of the reaction $\pi^- d \to \gamma nn$". *Nucl. Phys. A* 420 (1984), p. 496. DOI: `10.1016/0375-9474(84)90669-9`.

[132] G. F. de Téramond and B. Gabioud. "Charge asymmetry of the nuclear interaction and neutron-neutron scattering parameters". *Phys. Rev. C* 36 (1987), p. 691. DOI: `10.1103/PhysRevC.36.691`.

[133] A. Gårdestig and D. R. Phillips. "Using chiral perturbation theory to extract the neutron-neutron scattering length from $\pi^- d \to nn\gamma$". *Phys. Rev. C* 73 (2006), p. 014002. DOI: `10.1103/PhysRevC.73.014002`.

[134] D. R. Phillips. Personal communication. 2017.

[135] G. F. de Téramond. Personal communication. 2017.

[136] M. Lacombe et al. "Parametrization of the deuteron wave function of the Paris N-N potential". *Phys. Lett. B* 101 (1981), p. 139. DOI: `10.1016/0370-2693(81)90659-6`.

[137] J. R. M. Annand et al. *Experiment A2-01/13, Compton Scattering on the He Isotopes with an Active Target.* Experimental proposal, 2013.

[138] A. Starostin et al. "Measurement of $K^- \vec{p} \to \eta\Lambda$ near threshold". *Phys. Rev. C* 64 (2001), p. 055205. DOI: `10.1103/PhysRevC.64.055205`.

[139] K.-H. Kaiser et al. "The 1.5 GeV harmonic double-sided microtron at Mainz University". *Nucl. Instrum. Meth. Phys. Res. A* 593 (2008), p. 159. DOI: `10.1016/j.nima.2008.05.018`.

[140] M. Janecek. "Reflectivity Spectra for Commonly Used Reflectors". *IEEE Trans. Nucl. Sci.* 59 (2012), p. 490. DOI: `10.1109/TNS.2012.2183385`.

[141] M. Janecek and W. W. Moses. “Simulating Scintillator Light Collection Using Measured Optical Reflectance”. *IEEE Trans. Nucl. Sci.* 57 (2010), p. 964. DOI: `10.1109/TNS.2010.2042731`.

[142] SensL Technologies Ltd., SiPM specification sheet. URL: `http://www.sensl.com/downloads/ds/DS-MicroCseries.pdf`.

[143] R. Al Jebali. Personal communication. 2015.

[144] R. J. Brouns. *Absolute Measurement of Alpha emission and spontaneous fission.* 1968.

[145] J. J. Petruzzo III et al. “A 1 m radius spherical electron drift chamber for the measurement of relativistic heavy nuclei”. *Nucl. Instrum. Meth. Phys. Res. A* 402 (1998), p. 123. DOI: `10.1016/S0168-9002(97)00993-5`.

[146] J. Dietrich, V. Kamerdzhiev, and K. Reimers. “Performance of the Scintillation Profile Monitor in the COSY Synchrotron”. *Conf. Proc.* C110904 (2011). Preliminary green dot status, p. 1201.

[147] Y. M. Chan and A. Dalgarno. “The refractive index of helium”. *Proc. Phys. Soc.* 85 (1965), p. 227. URL: `http://stacks.iop.org/0370-1328/85/i=2/a=304`.

[148] Filmetrics, Inc. database, refractive index of Mylar. URL: `http://www.filmetrics.com/refractive-index-database/PET/Estar-Melinex-Mylar`.